# Nonlinear Modeling and Control of Automobiles with Dynamic Wheel-Road Friction and Wheel Torque Inputs

A Thesis
Presented to
The Academic Faculty

by

**Matthew G. Villella**

In Partial Fulfillment
of the Requirements for the Degree
Master of Science

School of Electrical and Computer Engineering
Georgia Institute of Technology
April 2004

# Nonlinear Modeling and Control of Automobiles with Dynamic Wheel-Road Friction and Wheel Torque Inputs

Approved by:

Professor David G. Taylor, Advisor

Professor Bonnie Heck-Ferri

Professor Olivier Bauchau
(School of Aerospace Engineering)

Professor Jerry H. Ginsberg
(School of Mechanical Engineering)

Date Approved: 12 April 2004

*To Conrad,*

*A great mentor and friend,*

*In thanks for the encouragement and prayers.*

# ACKNOWLEDGEMENTS

I would like to thank my advisor, Professor David G. Taylor, with whom I spent countless hours developing a new and fresh understanding of vehicle dynamics and control. His guidance in transmitting my ideas into mathematical and written form has been invaluable.

I would also like to thank my colleagues at General Motors who first exposed me to the problem of vehicle control, especially Mike Rizzo, who instilled in me the idea that good vehicle control should always be responsive to the driver.

Many thanks to my family and friends who have had to put up with me during the writing of this thesis. To my roommate and friend, Chris, who puts up with my perpetually bad attitude and temper. To Father Mario, who has provided great counsel and continual prayer. Most especially to Jenny, who always reminds me of what matters most.

Thanks also to my labmates, especially Matt Hortman and Nattapon Chayopitak, who have listened attentively and provided insightful suggestions and advice. They have demonstrated that an intelligent, thoughtful question is as valuable for true understanding of a problem as is the solution itself.

Finally, I gratefully acknowledge the support of Dr. David R. Hertling and the Office of Graduate Affairs of the School of Electrical and Computer Engineering at the Georgia Institute of Technology.

# TABLE OF CONTENTS

# LIST OF TABLES

# LIST OF FIGURES

# SUMMARY

This thesis presents a new nonlinear automobile dynamical model and investigates the possibility of automobile dynamic control with wheel torque utilizing this model. The model has been developed from first principles by applying classical mechanics. Inputs to the model are the four independent wheel torques, while the steer angles at each wheel are specified as independent time-varying signals. In this way, consideration of a variety of steering system architectures, including rear-wheel steer, is possible, and steering introduces time-varying structure into the vehicle model.

The frictional contact at the wheel-road interface is modeled by use of the LuGre dynamic friction model. Extensions to the existing two-dimensional LuGre friction model are derived and the steady-state of the friction model is compared to existing static friction models. Simulation results are presented to validate the model mathematics and to explore automobile behavior in a variety of scenarios.

Vehicle control with wheel torque is explored using the theory of input-output linearization for multi-input multi-output systems. System relative degree is analyzed and use of steady-state LuGre friction in a control design model is shown to give rise to relative degree singularities when no wheel slip occurs. Dynamic LuGre friction does not cause such singularities, but instead has an ill-defined nature under the same no-slip condition. A method for treating this ill-defined condition is developed, leading to the potential for the system to have relative degree.

Longitudinal velocity control and combined longitudinal and angular vehicle velocity control are demonstrated in simulation using input-output linearization, and are shown to produce improved vehicle response as compared to the open-loop behavior of the automobile. Robustness of the longitudinal velocity control to friction model parameter variation is explored and little impact to the controller's ability to track the desired trajectory is observed.

# CHAPTER I

# INTRODUCTION

In the past one hundred years, automobiles have revolutionized the world by facilitating transportation in a way that was never before possible. They have provided ordinary people with an inexpensive and reliable means of mobility, and they have met with universal appeal.

The success of the automobile has been predicated on the notion that any individual can operate one and that no special skills or advanced training are required for its use. This ideal has continually motivated the automotive community to seek and develop new technology that enhances the safety of automobile occupants and to improve the driver's ability to control the vehicle.

The National Highway Traffic Safety Administration (NHTSA) reported that in 2001, almost 11,000 fatal crashes occurred in which crash avoidance maneuvers were attempted, out of a total of 37,795 fatal crashes [32]. Such a statistic suggests that the drivers were unsuccessful at controlling the dynamics of the vehicle sufficiently to avoid or mitigate the crash.

In addition, it is well recognized that automobiles are difficult, if not impossible, for a driver to control on a slippery road. Such recognition has led automobile manufacturers to develop a wide range of electronic systems to improve vehicle response to the driver.

The first of such types of systems were Antilock Braking Systems (ABS) which attempt to reduce wheel slip during braking and such systems became feasible with the advent of microprocessors [9]. Following the development of anti-lock brakes, automotive manufacturers developed both Traction Control Systems (TCS) and Vehicle Stability Control Systems (VSC) in rapid succession. These systems make use of electronic control to apply braking force to a vehicle's wheels to limit slip during vehicle acceleration and to respond more effectively to driver commands in adverse situations, respectively.

Complementing these advances of automobile braking system technology have been

rapid proliferations in designs of All-Wheel-Drive (AWD) systems. Such mechanical systems allow for engine drive torque to be transmitted to all of the vehicle wheels in varying ratios, and with different mechanical constraints. In addition, electronically controllable all-wheel-drive systems that allow for active transfer of torque to individual wheels have become available. Paralleling this mechanical technology is the implementation of electric vehicle concepts which have individual motors powering each wheel, allowing for independent, fast torque generation at each vehicle corner.

These developments motivate consideration of how to best apply torque to wheels to achieve vehicle dynamic objectives with the aim of assisting the driver to maintain authority over the motion of the automobile.

## *1.1 Objectives of this Thesis*

In order to define the objectives of this thesis, it is necessary to consider its context within the existing body of literature on the vehicle control subject.

A great deal of work has been done on the topic of dynamic control for automobiles by many authors. This work has not been limited to the use of wheel torque for actuation, but has also included control by means of automatic steering, both for the front and rear wheels, and control of vehicle roll to influence normal force and subsequently road-wheel forces, in addition to many combinations of these control inputs.

It is our desire to understand the influence of wheel torque on the dynamics of an automobile and the potential it may have for completely controlling the motion of the vehicle. We shall therefore limit our attention to the body of work that includes wheel torque as a control input.

This corpus is still quite large and we consider two main subdivisions of this field of work. These are the linear model-based control design approaches and nonlinear model-based approaches.

The literature is replete with examples of linear model design for vehicle control. The linear models utilized either begin with linear model assumptions, or linearization of related nonlinear models is performed as a design step. Included among the linear model literature

is [46], in which output function controllability was investigated in depth for wheel torque, steering, and normal force control inputs. Other authors demonstrate a considerable amount of success designing controllers using a variety of well-known techniques. These include LQ optimal design to drive tracking error signals to zero, employed in [14, 37, 28, 44]; $H_\infty$ design in [36, 51]; model matching design, employed in [31, 24]; sliding mode control in [30]; predictive control in [1]; fuzzy logic control in [45]; and a host of other techniques by various researchers [15, 5, 49, 41, 21, 10].

These designs based upon linear vehicle models all possess the shortcoming that the linear models are at best approximate, and apply only locally under very restrictive conditions. Such restrictions generally include small steer angles and small tire slip angles.[1] Imposition of these requirements would prevent a full consideration of wheel torque implications for control and, in fact, such conditions are also unlikely to exist in adverse driving situations. For these reasons, we choose to pursue the development and implementation of a nonlinear vehicle model.

Nonlinearities are generally introduced into the vehicle model as a result of friction force generation models. These friction models, however, appear in the literature in a variety of forms. The Dugoff tire model was utilized by [27, 23, 20] and Pacejka tire models have been used in [48, 42]. Both of these models consist of empirical functions that have been fit to steady-state tire force data. Similar empirically-based models have been employed in [34, 39, 29, 43, 50]. The control techniques employed by these authors vary considerably from inverse dynamics methods of torque application as in [48] to sliding mode theory as in [27, 50].

Empirical friction models have the disadvantage of having no basis in physical principles. In addition, since the models consist of fits to steady-state data, they fail to capture any dynamic frictional effects that might be present. Because of this, such models are not well suited to the type of in-depth exploration of wheel torque capability that we wish to pursue.

Other authors such as [22] assume a nonlinear model structure but employ a somewhat heuristic torque generation method. In [13, 40] nonlinear structure is also assumed, but

[1] For a definition of tire/wheel slip angle, see [16, Chapter 10].

sliding mode techniques are employed that do not require friction model knowledge. In [13], however, the observation is made that the control functions well only for properly specified trajectories, thus limiting the approach.

Seeking to overcome these shortcomings, another class of friction models has been developed. These models are dynamic friction models that are based on physical notions and provide frictional force as a function of a dynamical friction state. The presence of such a friction state implies system memory that the other models were unable to exhibit. Recently, a new dynamic friction model was proposed in [6] and an application of this model to the case of a wheel was developed in [7], where traction control was demonstrated for a single wheel. No authors, however, have thus far presented an entire vehicle model for control system design based upon this friction model. This deficiency shall be addressed in this thesis.

In Chapter 2, a detailed development of a vehicle dynamic model is presented in an attempt to frame the vehicle control problem in a classical dynamics context. A general model that describes full vehicle body and wheel motion in the horizontal plane, and is independent of the type of friction model that shall be utilized, is shown.

Chapter 3 develops the mathematics that describe the dynamical friction model for a single wheel. Extensions to the existing model are discussed and the relationship of the steady-state form of the dynamical friction model to the existing static friction Pacejka model and the classical Coulomb friction model is explored.

In Chapter 4, the vehicle model of Chapter 2 and the friction model of Chapter 3 are assembled and presented in state-space form. The model properties are then explored through simulation in MATLAB.

Finally, Chapter 5 begins to explore the possibility of vehicle control by the use of wheel torque. A detailed consideration of system relative degree is presented and preliminary attempts to control the vehicle body trajectory by means of input-output linearization are undertaken.

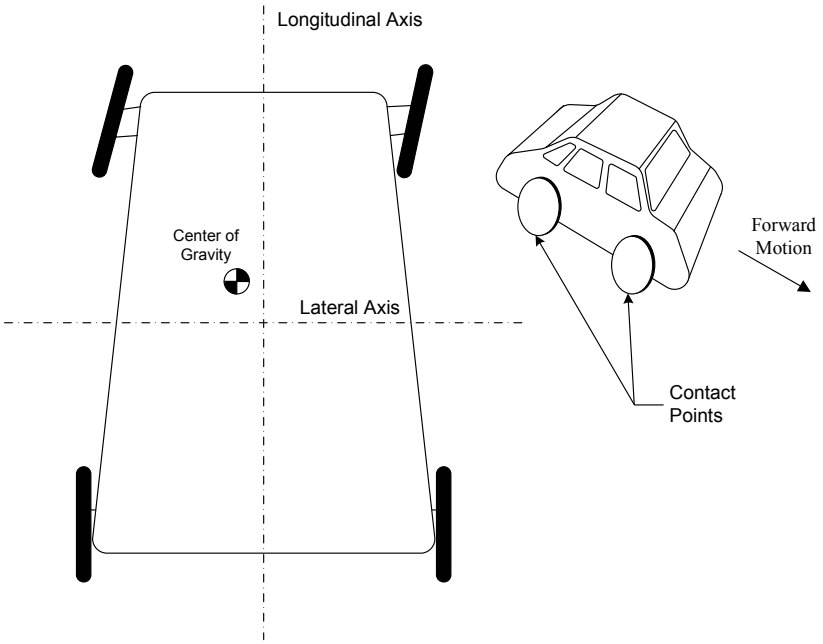


**Figure 1:** Vehicle system architecture.

## *1.2 System Architecture*

Prior to development of the mathematical description of motion of an automotive vehicle, it is necessary to clearly define the system whose properties we seek to model and control. A good control design model should expose only the most relevant vehicle properties that affect the system behavior that is to be controlled and limit the model complexity. However, model completeness and generality provide the advantage of allowing for consideration of a wide class of problems rather than being confined to application for a specific case. These factors motivate a system definition that is at once simple, yet complete.

The vehicle is defined as a system consisting of a vehicle body subsystem and four independent wheel subsystems, each with the same physical properties. The system architecture is shown in Figure 1. The wheels are rigidly attached to the vehicle body at each of four corners such that position of the center of each wheel is fixed with respect to the vehicle body.

The entire vehicle system is geometrically symmetric about one axis, which shall be

called the longitudinal axis. A lateral axis is defined perpendicular to the longitudinal axis, but no symmetry requirements about this axis are imposed. Thus the two front wheels are equidistant from both axes, as are the two rear wheels. The distance of front and rear wheels on the same side of the vehicle may differ.

The shape of the vehicle body is not specified, nor is its mass distribution. However, the horizontal position of the vehicle body center of gravity must lie within the trapezoid defined by the wheels.

The wheels are always in contact with a level, planar surface, which shall be referred to as the road. They are thin, rigid disks with uniformly distributed mass, and are oriented upright and perpendicular to the road. Thus, they contact the road at a single point and no camber angle[2] is allowed. The wheels are fixed to the vehicle body through their center of mass which lies at their geometric center. They are allowed to rotate freely about the axis perpendicular to the disk plane and passing through the wheel center, allowing them to roll. Rotation about a vertical axis passing through the wheel center is also permitted, corresponding to steer.

No steering or driveline constraints shall be explicity imposed during development of the model; that is, the wheels may roll and steer independently of one another. Constraints that limit this independence may therefore be considered as a special case and may be utilized in the simulation or control stage as desired.

The rigid connection of the wheels to the vehicle body precludes the presence of a suspension subsystem. This absence of a suspension is acceptable since suspension forces are internal to a vehicle system and have no effect on the motion of the entire system in the horizontal plane. Thus, a suspension would not influence the motion that we are interested in considering.

Development of a mathematical description of vehicle motion may now begin within this framework.

[2]For a definition of camber angle, see [16, 38].

# CHAPTER II

# VEHICLE MECHANICS

Consideration of the automobile control problem requires development of a mathematical understanding of the motion of the vehicle. We must therefore undertake a detailed study of the physics of the vehicle motion for development of both simulation and design models. The study of motion is classically subdivided into the two complementary areas of kinematics and dynamics. We will employ the techniques and laws of these fields in an attempt to produce a unified mathematical view of automobile dynamics.

## *2.1 Kinematics*

Consideration of vehicle motion requires that we first provide a means of describing that motion. This is the kinematics task of our vehicle mechanics study, where we shall define conventions for expressing how the vehicle may move. For our kinematics study, we are not yet concerned with the actual vehicle motion as produced by force and torque inputs; rather, we would first like to study the motion that is permitted by our choice of system architecture that was described in Section 1.2.

The vehicle system has two primary subsystems that require kinematical motion descriptions. The first is the *vehicle body*, which is our primary interest and whose motion we would ultimately like to control. The second subsystem is that of the *wheel*, which, through its four occurrences in the vehicle system, is our means of generating force through contact with the road. Since these subsystems are rigidly interconnected, we shall see that they have kinematical relationships to one another and that the overall vehicle motion is dependent on the kinematics of both subsystems.

### 2.1.1 Vehicle Body Kinematics

Development of the kinematics for the vehicle body requires that we first define appropriate coordinate frames. The choice of frames is non-unique and we therefore attempt to select

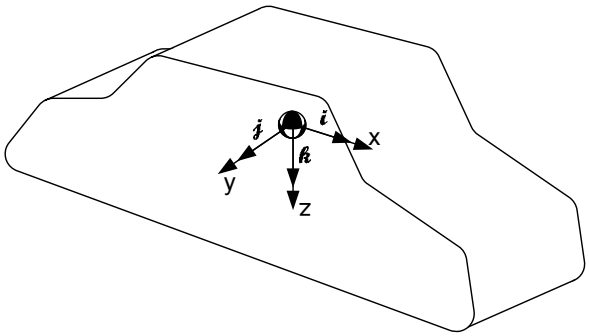


**Figure 2:** Vehicle body coordinate frame convention.

frames that provide a more intuitive physical insight into our problem. The vehicle body frame with axes $x, y, z$ and unit vectors $\boldsymbol{i}, \boldsymbol{j}, \boldsymbol{k}$ is chosen as in Figure 2. It is an inertial frame that is instantaneously coincident with the vehicle body's center of gravity. The $x$- and $y$-axes are instantaneously aligned with the longitudinal and lateral vehicle axes, respectively, and the $z$-axis is selected by a right-handed convention to point downward. This choice results in a positive sign convention for both yaw and lateral velocity motion to the right.

The choice of coordinate frame may be thought of as the vehicle occupant observation frame in which vehicle velocities and accelerations are experienced in the direction of vehicle orientation, but measured absolutely with respect to the earth. That is, the occupant observes motion of the environment with respect to the vehicle and the driver desires to influence these observations by choices of brake, accelerator, and steering inputs. This frame is clearly the frame in which driver assistance automatic control systems must operate.

With the vehicle body coordinate frame now defined, the velocity of the center of gravity of the vehicle body may be written as

$$\boldsymbol{v}_{cg} = v_x \boldsymbol{i} + v_y \boldsymbol{j} \tag{1}$$

where $v_x$ and $v_y$ are the velocity components along the $x$ and $y$ axes, respectively. We shall assume zero motion of the vehicle body in the $z$-axis direction, corresponding to a level driving surface. The velocity terms in the $z$-direction will therefore be left out of the development for simplicity.

Now, performing vector differentiation, the acceleration of the center of gravity, measured in the vehicle body coordinate frame is

$$\begin{aligned} \boldsymbol{a}_{cg} &= \frac{d\boldsymbol{v}_{cg}}{dt} \\ &= \dot{v}_x \boldsymbol{i} + \dot{v}_y \boldsymbol{j} + \omega_v \boldsymbol{k} \times (v_x \boldsymbol{i} + v_y \boldsymbol{j}) \\ &= (\dot{v}_x - \omega_v v_y)\, \boldsymbol{i} + (\dot{v}_y + \omega_v v_x)\, \boldsymbol{j} \end{aligned} \tag{2}$$

where $\omega_v$ is the angular velocity of the vehicle about the $z$-axis. Note that the vector differentiation results in coupling of the two velocity modes, which will have an impact on the dynamics of the vehicle as shall be seen later in Section 2.2.

### 2.1.2 Wheel Kinematics

Development of the wheel kinematics builds upon the vehicle kinematics and makes use of general kinematic results for measurements in moving coordinate frames [17, Chapter 3] to relate the motion of the two subsystems. The primary kinematic of interest for the wheels is the relative velocity between the wheel and the road at the point of contact between them. This relative velocity appears as an input to most force generation models, and we thus seek a description of it for later use.

From kinematics we know that for any stationary point, $n$, with respect to the vehicle body, the velocity of the point is

$$\boldsymbol{v}_n = \boldsymbol{v}_{cg} + \omega_v \boldsymbol{k} \times (x_n \boldsymbol{i} + y_n \boldsymbol{j})$$

where $x_n$ and $y_n$ are the coordinates of the point with respect to the vehicle body frame. Thus, for the center of wheel $n$, which remains at a fixed distance from the vehicle center of gravity, we have

$$\boldsymbol{v}_n = (v_x - \omega_v y_n)\, \boldsymbol{i} + (v_y + \omega_v x_n)\, \boldsymbol{j} \tag{3}$$

for $n = 1, \ldots, 4$, where $x_n$ and $y_n$ are now determined by the wheelbase and track width, respectively, of the vehicle. They are measured with respect to the center of gravity and are thus positive or negative as appropriate.

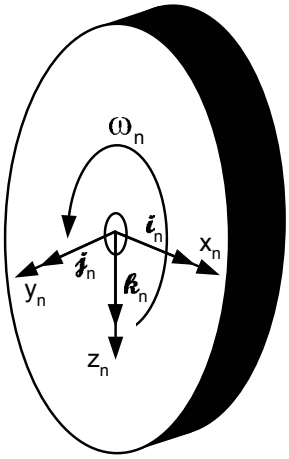


**Figure 3:** Wheel coordinate frame convention.

Now we define wheel coordinate frames with unit vectors $\boldsymbol{i}_n, \boldsymbol{j}_n, \boldsymbol{k}_n$ attached to the wheel center, with the $y$-axis aligned with the wheel rotational axis, and the $x$-axis parallel to the ground as in Figure 3. The frame rotates with the wheel as it steers but not as it rolls, thus the frame's orientation differs from the vehicle frame only by the wheel's steer angle, with the $z$-axis fixed parallel to the vehicle frame $z$-axis. The wheel angular velocity in this frame is then

$$\boldsymbol{\omega}_{w,n} = \omega_{w,n}\boldsymbol{j}_n$$

where $\omega_{w,n}$ is the scalar wheel rotation rate of wheel $n$. This results in a negative sign convention for forward roll motion, and is a necessary consequence for coordinate frame consistency.

The velocity of the point on the wheel directly below the wheel center and in contact with the ground, measured in this new frame is now simply

$$\boldsymbol{v}_{c,n} = \omega_{w,n} r \boldsymbol{i}_n$$

where $r$ is the wheel radius, which is assumed to be the same for all four wheels. The total velocity of this contact point is the relative velocity at the contact patch. This results from the fact that all variables in the defined coordinate frames are absolute. Since the velocity of the road surface is zero, any wheel velocity at the contact point is velocity relative to the road. The relative velocity at the contact patch is thus

$$\boldsymbol{v}_{r,n} = \boldsymbol{v}_{c,n} + \boldsymbol{v}_n \tag{4}$$

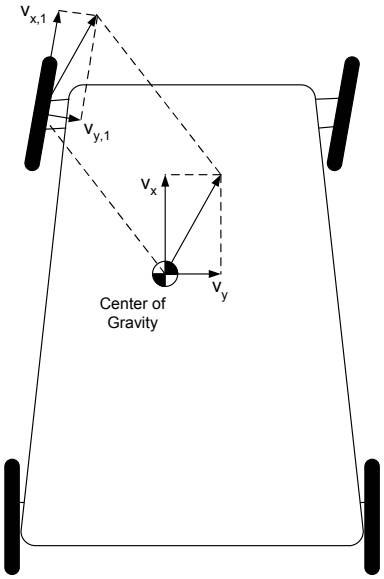


**Figure 4:** Velocity vector coordinate transformation.

but thus far, $\boldsymbol{v}_{c,n}$ and $\boldsymbol{v}_n$ have been expressed in different coordinate frames, with different unit vectors. We are able to mathematically relate the wheel and vehicle coordinate frames by the unit vector transformation equations

$$\begin{aligned} \boldsymbol{i} &= \cos\theta_n \boldsymbol{i}_n - \sin\theta_n \boldsymbol{j}_n \\ \boldsymbol{j} &= \sin\theta_n \boldsymbol{i}_n + \cos\theta_n \boldsymbol{j}_n \end{aligned} \tag{5}$$

for $n = 1, \ldots, 4$, where $\theta_n$ is the steer angle of wheel $n$. Transformation of the velocity, $\boldsymbol{v}_n$, from the vehicle body frame to the wheel coordinate frame is shown in Figure 4. We see from the figure that the absolute magnitude and direction of the velocity vector with respect to the inertial earth frame is unchanged by the transformation. Rather, we are merely changing the orientation of our measurement of this vector so that it may be related to other vectors measured in the same way. A more complete treatment of such transformations may be found in [17] and other mechanics texts.

Now, substituting $\boldsymbol{i}$ and $\boldsymbol{j}$ from (5) into the expression for $\boldsymbol{v}_n$ in (3), and adding $\boldsymbol{v}_{c,n}$, the relative velocity measured in the wheel coordinate frame becomes

$$\begin{aligned} \boldsymbol{v}_{r,n} &= \left[(v_x - \omega_v y_n)\cos\theta_n + (v_y + \omega_v x_n)\sin\theta_n + \omega_{w,n} r\right] \boldsymbol{i}_n \\ &\quad + \left[(v_y + \omega_v x_n)\cos\theta_n - (v_x - \omega_v y_n)\sin\theta_n\right] \boldsymbol{j}_n \end{aligned} \tag{6}$$

for $n = 1, \ldots, 4$. For the case of one-dimensional motion this equation simplifies to

$$v_r = v_x + \omega_w r$$

and noting the negative sign convention for forward roll, the relative velocity is equal to the difference between the linear vehicle velocity and the tangential wheel velocity. This is equivalent to the relative velocity relation in the one-dimensional formulation of [8], with an opposite sign convention for $\omega_w$, and confirms our general two-dimensional result.

Note that in (6) there is an explicit dependence of only the $x$-component of $\boldsymbol{v}_{r,n}$ on the wheel angular velocity, indicating that lateral wheel relative velocity results purely from vehicle motion, and not directly from wheel motion. This will prove to be very important in the development of vehicle control as we shall see in Chapter 5.

## *2.2 Dynamics*

With the kinematics of the vehicle defined, we may turn our attention to the dynamical behavior of the system. We now consider how the motion that is described by the kinematical equations is produced. For this development, a Newton-Euler formulation shall be utilized due to the physical insight that it provides. This method for deriving the dynamical equations is made possible by model simplicity that results from both our system architecture and some appropriate dynamics assumptions. These assumptions shall be discussed, where appropriate, as the development of the model dynamics proceeds.

### 2.2.1 Vehicle Body

According to Newton's Law, the net sum of the forces acting upon the vehicle is equal to the rate of change of the linear vehicle momentum. This results in the following expression for the acceleration of the vehicle's center of gravity

$$\sum_{n=1}^{4} \boldsymbol{F}_n = m_v \boldsymbol{a}_{cg} \tag{7}$$

where $\boldsymbol{F}_n$ is the vector force acting in the plane of motion at the $n$th wheel in the vehicle frame and $m_v$ is the total lumped vehicle mass of the vehicle body plus the wheels. This

force is defined component-wise in the wheel frame as

$$\boldsymbol{F}_n \equiv F_{x,n}\boldsymbol{i}_n + F_{y,n}\boldsymbol{j}_n$$

The $z$-component of the force acting at each wheel is the normal force and shall be dealt with separately since it does not directly influence the $x$- and $y$-axis dynamics of interest.

This force must be transformed from the wheel to the vehicle frame for use in (7). This transformation is accomplished by the inverse of the unit vector transformation of (5) and results in

$$\boldsymbol{F}_n = \left(F_{x,n}\cos\theta_n - F_{y,n}\sin\theta_n\right)\boldsymbol{i} + \left(F_{x,n}\sin\theta_n + F_{y,n}\cos\theta_n\right)\boldsymbol{j} \tag{8}$$

Substituting these transformed forces and the acceleration from (2) into (7), and separating into components, we have the dynamical equations for the linear motion of the vehicle

$$\boldsymbol{\lambda}_c^T(\boldsymbol{\theta})\boldsymbol{F}_x - \boldsymbol{\lambda}_s^T(\boldsymbol{\theta})\boldsymbol{F}_y = m_v\left(\dot{v}_x - \omega_v v_y\right) \tag{9}$$

$$\boldsymbol{\lambda}_s^T(\boldsymbol{\theta})\boldsymbol{F}_x + \boldsymbol{\lambda}_c^T(\boldsymbol{\theta})\boldsymbol{F}_y = m_v\left(\dot{v}_y + \omega_v v_x\right) \tag{10}$$

where $\boldsymbol{\theta} = [\theta_1, \ldots, \theta_4]^T$ is a vector of the steering angles,

$$\begin{aligned}\boldsymbol{\lambda}_c(\boldsymbol{\theta}) &= [\cos\theta_1, \ldots, \cos\theta_4]^T \\ \boldsymbol{\lambda}_s(\boldsymbol{\theta}) &= [\sin\theta_1, \ldots, \sin\theta_4]^T\end{aligned}$$

are vectors of the cosine and sine of each steering angle and

$$\begin{aligned}\boldsymbol{F}_x &= [F_{x,1}, \ldots, F_{x,4}]^T \\ \boldsymbol{F}_y &= [F_{y,1}, \ldots, F_{y,4}]^T\end{aligned}$$

are the $x$- and $y$-component force vectors. Equations (9) and (10) define the translational motion of the vehicle, but rotational motion must occur as well.

Euler's Law for rotational motion requires that the net torque about an axis must be equal to the rate of change of the angular momentum. Since the system architecture dictates that the only rotational motion of the vehicle body that may occur is yaw motion about the $z$-axis, and neglecting the angular momentum change produced by the rotation of the

spinning wheels about the vertical axis, Euler's Law for the vehicle body simplifies to the scalar equation

$$\tau_v = I_v \alpha_v \tag{11}$$

where $\tau_v$ is the total torque about the $z$-axis produced by the road-wheel forces, $\alpha_v$ is the angular acceleration of the vehicle, and $I_v$ is the inertia of the vehicle about the $z$-axis. The fact that no pitch or roll motion occurs is a consequence of the absence of a vehicle suspension. With the wheels rigidly fixed to the vehicle body, pitch and roll could only occur if one or more wheels ceased to contact the ground, and we choose not to consider such extreme cases. The angular momentum change of the wheels due to rotation about the vertical axis is very small in comparison to that resulting from rotation of the vehicle body, due to the significant difference between wheel and vehicle inertias. Our choice to neglect this momentum change is therefore well justified and should pose little reduction to the accuracy of our model. Note, however, that for high velocity maneuvers such as might occur for racing vehicles, the assumption may no longer prove to be valid since both angular momentum and angular momentum rate could be considerably higher. We shall therefore limit use of this model to less aggressive passenger vehicle maneuvers.

Now, expressing the torque in terms of the forces at each wheel and the moment arms about the vehicle center of gravity, we obtain the third dynamical equation for the vehicle body which describes the rotational motion as

$$\left(-\boldsymbol{F}_x^T \boldsymbol{Y} + \boldsymbol{F}_y^T \boldsymbol{X}\right) \boldsymbol{\lambda}_c(\boldsymbol{\theta}) + \left(\boldsymbol{F}_x^T \boldsymbol{X} + \boldsymbol{F}_y^T \boldsymbol{Y}\right) \boldsymbol{\lambda}_s(\boldsymbol{\theta}) = I_v \alpha_v \tag{12}$$

where we have utilized our previous definitions for the force and trigonometric vectors, and $\boldsymbol{X}$ and $\boldsymbol{Y}$ are diagonal matrices with the $x$ and $y$-coordinates of each wheel along the respective diagonals.

Equations (9), (10), and (12) are the dynamical equations required for description of the vehicle body motion. The description of the dynamical motion of the entire vehicle system will not be complete until we develop the dynamical equations for the wheels.

### 2.2.2 Wheels

In order to consider the wheel dynamics, we continue to ignore the momentum change produced by the yaw motion of the wheels, and recognize that our defined vehicle architecture prohibits wheel camber motion (rotation about the $x$-axis). We also assume that steering angle is produced by the action of a driver, regardless of dynamics, so that steering is simply a time-varying kinematic. Then we must only write the equations that describe the rotation of the wheels about the wheel-fixed $y$-axis. From Euler's law, this is simply

$$\tau_{w,n} + F_{x,n} r = I_w \alpha_{w,n} \tag{13}$$

for $n = 1, \ldots, 4$, where $\tau_{w,n}$ is the input torque that drives wheel $n$, $\alpha_{w,n}$ is the wheel angular acceleration, and $I_w$ is the wheel rotational inertia about the wheel frame $y$-axis, which we assume is identical for all wheels.

With the addition of (13) to our vehicle body dynamical equations, we now have a description of the vehicle dynamics in terms of the road-wheel forces. These forces are the subject of consideration in the next section.

## *2.3 Force Mechanics*

While we have now successfully described the mechanics of the motion of an automobile, we do not yet know how the forces that appear in the dynamical equations are generated. These forces are the external forces acting upon our system at the road-wheel interface, and arise solely as a result of contact phenomena. Contact mechanisms fall into the two categories of reactional or normal contact, and frictional contact. In general, rigid body contacts have components of both of these types, and this is true of the case of contact between a vehicle wheel and the road surface. We must therefore develop a mathematical description of the forces generated by these two types of contact in order to produce a vehicle model.

Normal force is generated perpendicular to the plane of contact and is a reaction to the applied force in that direction. In the case of the automobile, normal force is applied by the road surface to the vehicle's wheels, acting upward in the negative $z$-axis direction.

Normal force is produced only by reaction to the vehicle's weight since we are assuming zero pitch and roll motion and ignoring the contribution of wheel angular momentum changes. However, since contact occurs at each of the four wheels, the total normal force must be distributed among the four points of contact. This normal force distribution does not remain constant, but must vary to produce the forces necessary to maintain zero pitch and roll conditions. We will refer to this phenomenon as static weight transfer since no motion occurs as a result of the application of the normal forces, but the total normal force is maintained constantly equal to the vehicle's weight and is transferred among the wheels.

Since normal force does not produce motion, our interest in it results completely from the fact that it contributes to the generation of frictional force and must be known in order to determine the influence of the frictional contact on vehicle motion. Despite this fact, the appearance of normal force in friction models is prominent and normal force therefore has a significant role in our model development.

We must confine our consideration to normal forces acting upwards since downward normal force has no physical meaning. With our vehicle frame coordinate conventions, this means that normal force is negative semi-definite, however, it is more common in practice to consider normal force to be greater than or equal to zero. We shall therefore consider normal force to be positive semi-definite and append negative signs as necessary to maintain coordinate frame consistency.

In order to compute normal force, we must perform a static force balance in the $z$-direction and static moment balances about the pitch and roll axes. Since no motion actually occurs about these axes, their location may be selected arbitrarily as long as the orientations are fixed parallel to the vehicle frame $x$- and $y$-axes. We select these axes as shown in Figure 5 so that they pass through the center of gravity of the vehicle body.

We denote the normal force at wheel $n$ as $N_n$ and recognize that the moment arms of the normal forces about the pitch and roll axes are now simply the previously defined track width and wheelbase coordinate parameters $x_n$ and $y_n$. We may then formulate the static

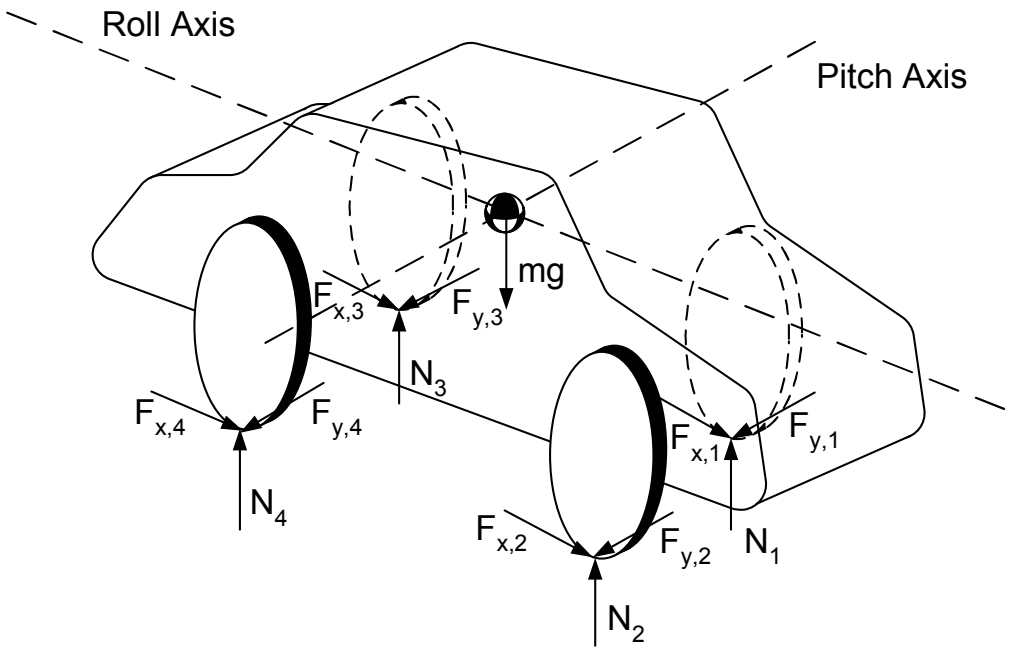


**Figure 5:** Static force and moment balance for determination of normal force.

force and moment balance equations as

$$\begin{aligned} \boldsymbol{y}^T\boldsymbol{N} + h(\boldsymbol{\lambda}_s^T(\boldsymbol{\theta})\boldsymbol{F}_x + \boldsymbol{\lambda}_c^T(\boldsymbol{\theta})\boldsymbol{F}_y) &= 0, \text{ roll moment balance} \\ \boldsymbol{x}^T\boldsymbol{N} + h(\boldsymbol{\lambda}_c^T(\boldsymbol{\theta})\boldsymbol{F}_x - \boldsymbol{\lambda}_s^T(\boldsymbol{\theta})\boldsymbol{F}_y) &= 0, \text{ pitch moment balance} \\ \textstyle\sum_{n=1}^{4} N_n - m_v g &= 0, \text{ force balance} \end{aligned}$$

where $h$ is the height of the vehicle body center of gravity above the ground, $g$ is the gravitational acceleration, $\boldsymbol{x}$ and $\boldsymbol{y}$ are vectors of the $x$ and $y$ wheel coordinates, and $\boldsymbol{N}$ is a vector of the normal forces, $N_n$ for $n = 1, \ldots, 4$.

This system of equations is underdetermined because we wish to solve for four unknown normal forces, but have only these three independent equations. The underdetermined nature of the problem indicates that there is not a single solution, but a manifold upon which the solution may lie. That is, an infinite number of solutions that will satisfy the static force and moment balance equations exists. Resolving this difficulty requires that either an assumption must be made about the normal forces to supplement these equations, or that dynamics must be considered. We wish to avoid the complexity of suspension dynamics

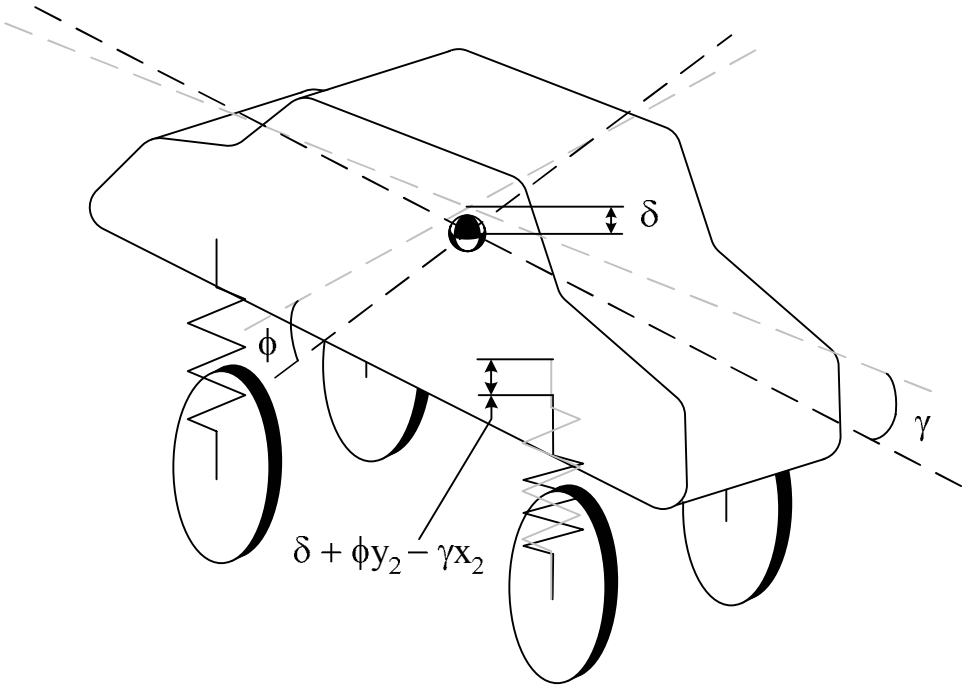


**Figure 6:** Suspension model for normal force determination.

and the addition of state variables that this approach would require, but an arbitrary assumption for normal force distribution would reduce the validity of our model. Instead, we shall attempt to impose a constraint that is consistent with our physical understanding of the system architecture in order to find a single solution to the statics equations.

We begin by considering a hypothetical simple suspension model for analysis purposes as shown in Figure 6. This suspension model is artificial and shall only be used for development of the normal force equations and will not be employed in the overall vehicle model.

Let us define $\phi$ and $\gamma$ as the roll and pitch, respectively, about the axes that we have already defined, and $\delta$ as the linear deviation of the vehicle body height from its initial position. These variables all describe motion of the artificial suspension and not actual vehicle body motion. As such, they are purely mathematical devices we are employing for the task of determining a normal force solution, and have no true physical manifestation in the vehicle system.

Applying Hooke's Law to our suspension model at each wheel, we may write the normal

forces as the spring compression times the spring constant, $k$. Spring compression results from the combination of translational motion in the $z$-direction and the pitch and roll rotations of the vehicle body, shown in Figure 6. For the small pitch and roll angles that are implied by very stiff springs, we may use the approximations that $\sin\phi \approx \phi$ and $\sin\gamma \approx \gamma$ so that these angles enter our equations linearly rather than through trigonometric nonlinearities. In our case, the springs are approaching infinite stiffness, and the approximation is therefore valid. Then, assuming that the springs are constrained to apply force only along the $z$-axis, and that we have equal spring constants at all four wheels, we may express the normal forces as

$$N_n = k\left(\delta + \phi y_n - \gamma x_n\right),\ n = 1, \ldots, 4 \tag{14}$$

Note that since we have lumped the wheel mass together with the vehicle body mass and no actual pitch and roll motion occurs, inclusion of wheel mass gravitational force in these equations would be redundant. However, if pitch and roll were allowed, we would be required to consider the mass of the wheels and vehicle separately and this formulation would not apply.

The equations of (14), combined with the static force and moment balance equations, are a system of seven equations in seven unknowns. We may solve this system of equations sequentially by first substituting (14) into the force and moment balance equations and then solving for the three artificial motion variables, $\phi$, $\gamma$, and $\delta$. Doing so, we find that

$$\begin{aligned}
\delta &= \frac{1}{k}\left(p_{\delta,y}\boldsymbol{\lambda}_s^T(\boldsymbol{\theta}) - p_{\delta,x}\boldsymbol{\lambda}_c^T(\boldsymbol{\theta})\right)\boldsymbol{F}_x - \frac{1}{k}\left(p_{\delta,y}\boldsymbol{\lambda}_c^T(\boldsymbol{\theta}) + p_{\delta,x}\boldsymbol{\lambda}_s^T(\boldsymbol{\theta})\right)\boldsymbol{F}_y + \frac{1}{k}b_\delta \\
\phi &= -\frac{1}{k}p_\phi\boldsymbol{\lambda}_s^T(\boldsymbol{\theta})\boldsymbol{F}_x - \frac{1}{k}p_\phi\boldsymbol{\lambda}_c^T(\boldsymbol{\theta})\boldsymbol{F}_y + \frac{1}{k}b_\phi \\
\gamma &= \frac{1}{k}p_\gamma\boldsymbol{\lambda}_c^T(\boldsymbol{\theta})\boldsymbol{F}_x - \frac{1}{k}p_\gamma\boldsymbol{\lambda}_s^T(\boldsymbol{\theta})\boldsymbol{F}_y + \frac{1}{k}b_\gamma
\end{aligned}$$

where

$$\begin{aligned}
p_{\delta,x} &= \frac{h}{D_x}\sum_{n=1}^{4} x_n \\
p_{\delta,y} &= \frac{h}{D_y}\sum_{n=1}^{4} y_n \\
b_\delta &= \frac{1}{4}m_v g\left[1 + \frac{1}{D_y}\left(\sum_{n=1}^{4} y_n\right)^2 + \frac{1}{D_x}\left(\sum_{n=1}^{4} x_n\right)^2\right]
\end{aligned}$$

$$
\begin{aligned}
p_\phi &= \frac{4h}{D_y} \\
b_\phi &= -\frac{m_v g}{D_y}\sum_{n=1}^{4} y_n \\
p_\gamma &= \frac{4h}{D_x} \\
b_\gamma &= \frac{m_v g}{D_x}\sum_{n=1}^{4} x_n
\end{aligned}
$$

with

$$
\begin{aligned}
D_x &= 4\sum_{n=1}^{4} x_n^2 - \left(\sum_{n=1}^{4} x_n\right)^2 \\
D_y &= 4\sum_{n=1}^{4} y_n^2 - \left(\sum_{n=1}^{4} y_n\right)^2
\end{aligned}
$$

This solution, when utilized in the normal force equations of (14) yields the normal force distribution solution

$$
\boldsymbol{N} = \boldsymbol{c} + \boldsymbol{P}_x(\boldsymbol{\theta})\boldsymbol{F}_x + \boldsymbol{P}_y(\boldsymbol{\theta})\boldsymbol{F}_y \tag{15}
$$

where

$$
\boldsymbol{c} = b_\delta \mathbf{1}_{4\times 1} + b_\phi \boldsymbol{y} - b_\gamma \boldsymbol{x} \tag{16}
$$

with $\mathbf{1}_{4\times 1}$ as a $4 \times 1$ vector of ones, and the functions preceding the force vectors are

$$
\boldsymbol{P}_x(\boldsymbol{\theta}) = \begin{bmatrix} q_{xx,1}\cos\theta_1 + q_{yx,1}\sin\theta_1 & \cdots & q_{xx,1}\cos\theta_4 + q_{yx,1}\sin\theta_4 \\ \vdots & \ddots & \vdots \\ q_{xx,4}\cos\theta_1 + q_{yx,4}\sin\theta_1 & \cdots & q_{xx,4}\cos\theta_4 + q_{yx,4}\sin\theta_4 \end{bmatrix} \tag{17}
$$

$$
\boldsymbol{P}_y(\boldsymbol{\theta}) = \begin{bmatrix} q_{xy,1}\sin\theta_1 + q_{yy,1}\cos\theta_1 & \cdots & q_{xy,1}\sin\theta_4 + q_{yy,1}\cos\theta_4 \\ \vdots & \ddots & \vdots \\ q_{xy,4}\sin\theta_1 + q_{yy,4}\cos\theta_1 & \cdots & q_{xy,4}\sin\theta_4 + q_{yy,4}\cos\theta_4 \end{bmatrix} \tag{18}
$$

which are $4 \times 4$ matrices of geometric parameters and steering angles where

$$
q_{xx,n} = -\frac{h\left(4x_n + \sum_{n=1}^{4} x_n\right)}{4\sum_{n=1}^{4} x_n^2 - \left(\sum_{n=1}^{4} x_n\right)^2} \tag{19}
$$

$$
q_{yx,n} = -\frac{h\left(4y_n - \sum_{n=1}^{4} y_n\right)}{4\sum_{n=1}^{4} y_n^2 - \left(\sum_{n=1}^{4} y_n\right)^2} \tag{20}
$$

$$q_{xy,n} = \frac{h\left(4x_n - \sum_{n=1}^{4} x_n\right)}{4\sum_{n=1}^{4} x_n^2 - \left(\sum_{n=1}^{4} x_n\right)^2} \tag{21}$$

$$q_{yy,n} = -\frac{h\left(4y_n + \sum_{n=1}^{4} y_n\right)}{4\sum_{n=1}^{4} y_n^2 - \left(\sum_{n=1}^{4} y_n\right)^2} \tag{22}$$

We see that the dependence on the spring stiffness, $k$, has been eliminated in (15) and that this equation depends only on geometric parameters, friction forces, and steering angles.

Friction force was our motivation for considering normal force when we began our development and (15) is therefore not completely useful in its present form since we still do not have an explicit solution for the friction forces. We may resolve this dilemma by recognizing that, in general, friction models produce force that is linearly related to the normal force. We therefore define diagonal matrices $\boldsymbol{\mu}_x$ and $\boldsymbol{\mu}_y$ with friction functions for each $x$ and $y$-component force, respectively, along the main diagonal. This now allows us to write the relationship between friction and normal force for all four wheels in vector form as

$$\begin{aligned} \boldsymbol{F}_x &= \boldsymbol{\mu}_x \boldsymbol{N} \\ \boldsymbol{F}_y &= \boldsymbol{\mu}_y \boldsymbol{N} \end{aligned} \tag{23}$$

With these definitions, we may now rewrite (15) as

$$\boldsymbol{N} = \boldsymbol{c} + \boldsymbol{P}_x(\boldsymbol{\theta})\boldsymbol{\mu}_x \boldsymbol{N} + \boldsymbol{P}_y(\boldsymbol{\theta})\boldsymbol{\mu}_y \boldsymbol{N} \tag{24}$$

which may be solved for an explicit expression for normal force in terms of geometric parameters, steering angles, and friction functions as

$$\boldsymbol{N} = \left(\boldsymbol{I}_4 - \boldsymbol{P}_x(\boldsymbol{\theta})\boldsymbol{\mu}_x - \boldsymbol{P}_y(\boldsymbol{\theta})\boldsymbol{\mu}_y\right)^{-1} \boldsymbol{c} \tag{25}$$

where $\boldsymbol{I}_4$ is the $4 \times 4$ identity matrix, and we assume for the present time that the matrix inverse in this equation exists.

Using this normal force result and the relations of (23), we are now able express the friction forces as

$$\begin{aligned} \boldsymbol{F}_x &= \boldsymbol{\mu}_x \left(\boldsymbol{I}_4 - \boldsymbol{P}_x(\boldsymbol{\theta})\boldsymbol{\mu}_x - \boldsymbol{P}_y(\boldsymbol{\theta})\boldsymbol{\mu}_y\right)^{-1} \boldsymbol{c} \\ \boldsymbol{F}_y &= \boldsymbol{\mu}_y \left(\boldsymbol{I}_4 - \boldsymbol{P}_x(\boldsymbol{\theta})\boldsymbol{\mu}_x - \boldsymbol{P}_y(\boldsymbol{\theta})\boldsymbol{\mu}_y\right)^{-1} \boldsymbol{c} \end{aligned} \tag{26}$$

This solution is independent of the specific friction model and may be utilized in the dynamical equations of Section 2.2 to eliminate dependence on the frictional forces.

## 2.4 Vehicle Mechanics Summary

We have now completed our description of vehicle motion and may assemble all of our equations into a vehicle model. The model consists of vehicle body dynamical equations, wheel dynamical equations, and force equations.

We begin by rewriting the vehicle body dynamical equation of rotation, (12), as

$$\left(\boldsymbol{\lambda}_s^T(\boldsymbol{\theta})\boldsymbol{X} - \boldsymbol{\lambda}_c^T(\boldsymbol{\theta})\boldsymbol{Y}\right)\boldsymbol{F}_x + \left(\boldsymbol{\lambda}_c^T(\boldsymbol{\theta})\boldsymbol{X} + \boldsymbol{\lambda}_s^T(\boldsymbol{\theta})\boldsymbol{Y}\right)\boldsymbol{F}_y = I_v\alpha_v \tag{27}$$

where we have taken the transpose of the left-hand side and factored out the force vectors. We now write the wheel rotation equations of (13) in matrix-vector form as

$$\boldsymbol{\tau} + r\boldsymbol{F}_x = I_w\boldsymbol{\alpha}_w \tag{28}$$

where $\boldsymbol{\tau}$ is a vector of the four wheel torque inputs, and $\boldsymbol{\alpha}_w$ is a vector of the four wheel angular accelerations.

For convenience, we also repeat the dynamical equations of (9) and (10) here

$$\begin{aligned}
\boldsymbol{\lambda}_c^T(\boldsymbol{\theta})\boldsymbol{F}_x - \boldsymbol{\lambda}_s^T(\boldsymbol{\theta})\boldsymbol{F}_y &= m_v\left(\dot{v}_x - \omega_v v_y\right) \\
\boldsymbol{\lambda}_s^T(\boldsymbol{\theta})\boldsymbol{F}_x + \boldsymbol{\lambda}_c^T(\boldsymbol{\theta})\boldsymbol{F}_y &= m_v\left(\dot{v}_y + \omega_v v_x\right)
\end{aligned}$$

which completes the set of vehicle dynamic equations.

We see that these equations are all linear functions of the force vectors, which enables us to express them together as the vector equations

$$\boldsymbol{M}_1\dot{\boldsymbol{\xi}} = \boldsymbol{\eta}(\boldsymbol{\xi}) + \boldsymbol{A}_x(\boldsymbol{\theta})\boldsymbol{F}_x + \boldsymbol{A}_y(\boldsymbol{\theta})\boldsymbol{F}_y \tag{29}$$

$$\boldsymbol{M}_2\dot{\boldsymbol{\nu}} = r\boldsymbol{F}_x + \boldsymbol{\tau} \tag{30}$$

where

$$\boldsymbol{M}_1 = \begin{bmatrix} m_v & 0 & 0 \\ 0 & m_v & 0 \\ 0 & 0 & I_v \end{bmatrix} \tag{31}$$

$$\boldsymbol{M}_2 = I_w\boldsymbol{I}_4 \tag{32}$$

are the diagonal mass matrices,

$$\boldsymbol{\xi} = [v_x, v_y, \omega_v]^T \tag{33}$$

$$\boldsymbol{\nu} = \boldsymbol{\omega}_w \tag{34}$$

are state vector partitions, and

$$\boldsymbol{A}_x = \begin{bmatrix} \boldsymbol{\lambda}_c^T(\boldsymbol{\theta}) \\ \boldsymbol{\lambda}_s^T(\boldsymbol{\theta}) \\ \boldsymbol{\lambda}_s^T(\boldsymbol{\theta})\boldsymbol{X} - \boldsymbol{\lambda}_c^T(\boldsymbol{\theta})\boldsymbol{Y} \end{bmatrix} \tag{35}$$

$$\boldsymbol{A}_y = \begin{bmatrix} -\boldsymbol{\lambda}_s^T(\boldsymbol{\theta}) \\ \boldsymbol{\lambda}_c^T(\boldsymbol{\theta}) \\ \boldsymbol{\lambda}_c^T(\boldsymbol{\theta})\boldsymbol{X} + \boldsymbol{\lambda}_s^T(\boldsymbol{\theta})\boldsymbol{Y} \end{bmatrix} \tag{36}$$

$$\boldsymbol{\eta}(\boldsymbol{\xi}) = m_v[\omega_v v_y, -\omega_v v_x, 0]^T \tag{37}$$

We may now substitute the forces of (26) into the vehicle model of (29)-(30) to find that

$$\boldsymbol{M}_1\dot{\boldsymbol{\xi}} = \boldsymbol{\eta}(\boldsymbol{\xi}) + \left(\boldsymbol{A}_x(\boldsymbol{\theta})\boldsymbol{\mu}_x + \boldsymbol{A}_y(\boldsymbol{\theta})\boldsymbol{\mu}_y\right)\left(\boldsymbol{I}_4 - \boldsymbol{P}_x(\boldsymbol{\theta})\boldsymbol{\mu}_x - \boldsymbol{P}_y(\boldsymbol{\theta})\boldsymbol{\mu}_y\right)^{-1}\boldsymbol{c} \tag{38}$$

$$\boldsymbol{M}_2\dot{\boldsymbol{\nu}} = r\boldsymbol{\mu}_x\left(\boldsymbol{I}_4 - \boldsymbol{P}_x(\boldsymbol{\theta})\boldsymbol{\mu}_x - \boldsymbol{P}_y(\boldsymbol{\theta})\boldsymbol{\mu}_y\right)^{-1}\boldsymbol{c} + \boldsymbol{\tau} \tag{39}$$

Note here that while neither $\boldsymbol{\nu}$ nor $\boldsymbol{\tau}$ appear explicitly in the vehicle body dynamical equations of (38), coupling of these equations occurs by means of the friction matrices, $\boldsymbol{\mu}_x$ and $\boldsymbol{\mu}_y$, which we now see must necessarily be state dependent functions.

Thus, the influence of the wheel torque vector, $\boldsymbol{\tau}$, on the vehicle body motion occurs solely as a result of the presence of friction. This motivates us to consider the exact form of a friction model for use in this work, since it is now clear that the vehicle dynamic model cannot be complete without specification of $\boldsymbol{\mu}_x$ and $\boldsymbol{\mu}_y$. This task is, in fact, the subject of the next chapter.

# CHAPTER III

# ROAD-WHEEL FRICTION

Thus far, we have considered all of the necessary components of a vehicle model except for the friction function that was introduced in Section 2.3. This function was written in generic form such that substitution of any desirable friction model into the vehicle model was made possible, but the nature of this function or the friction phenomenon that it describes has not yet been considered.

Friction occurs when two bodies contact one another, and is responsible for the generation of dissipative forces that are parallel to the contact surface. These forces are dissipative in that they oppose the relative motion of these bodies with respect to one another and act only to decrease system energy. Frictional mechanisms are not generally well understood, however, many models have been developed that attempt to describe the macroscopic effect of this phenomenon.

In this chapter we shall discuss our choice of friction model for application to contact between a wheel and the road surface. In keeping with the formulation of Chapter 2, our model must produce a unitless multiplier of normal force as output, however, we have not yet specified any requirements for the inputs to the friction model, nor have we imposed a particular model structure. Our previous results therefore leave us free to select the most appropriate friction model for our task.

The classical approach to the modeling of friction is the Coulomb model. The key feature of Coulomb friction is that it is a discontinuous function of the relative velocity between the contact surfaces, and as such it is an idealization and approximation of true behavior. Many other methods for modeling friction have been proposed in the literature including continuous approximations to the discontinuous Coulomb friction model [2] and empirical force models such as Pacejka's Magic Formula [35]. These models, while often mathematically simple, do not fully describe modern experimental observations of friction

behavior [2].

We choose instead to utilize a friction model that is developed from first principles with physical parameters that may be selected by a vehicle designer or experimentally determined for an existing vehicle. Such a model was introduced in [6] and was demonstrated to be an accurate model of true behavior in [8]. This model, referred to as the LuGre Friction Model, shall be embraced in this work for its desirable characteristics, however some extensions to the model are necessary for complete applicability to the vehicle modeling problem.

## *3.1 The Two-Dimensional LuGre Model*

The LuGre friction model is based upon a view of friction as the interaction of microscopic surface asperities which act as bristles and deflect as the surfaces move with respect to one another [6]. The deflection of the bristles is described by a dynamical equation and the frictional force is a function of the deflection state. This results in a dynamical friction model which exhibits transient behavior and is able to capture the behavior of other friction models such as the Pacejka model as a special case of its steady state [8].

The LuGre model introduced in [6] is a point-contact lumped parameter model which may be employed to describe wheel-road contact. For the case of non-rigid tire-road contact, a distributed version of the LuGre model has been developed to describe contact patch interaction rather than simple point contact [8, 12]. This distributed model is then averaged over the contact patch to produce an average lumped model. We shall confine our present attention to the original point-contact LuGre model, which is consistent with our rigid wheel system architecture, but note that a distributed formulation is possible for our model as well.

The LuGre model was originally presented in one-dimensional form [6] and subsequently extended to two dimensions in [11, 12, 47]. We present an alternative two-dimensional extension to the LuGre model that corrects some discrepancies in these previous models and provides the necessary outputs for use in our vehicle model.

Formulation of the correct two-dimensional extension to the LuGre model requires a full comprehension of the vector nature of the kinematics of the friction model. We must

recognize that scalar mathematics describe a special case of vector mathematics where all but one component are identically zero. In addition, multi-dimensional motion requires consideration of rotation which was not present in the scalar case. Thus, progression from a scalar one-dimensional model to a vector two-dimensional model cannot generally be accomplished by duplicating scalar results for each motion axis. We will therefore consider a vector formulation for LuGre friction so that we may benefit from the techniques of vector mathematics.

### 3.1.1 Vector Friction Model and Bristle Kinematics

Development of the two-dimensional model requires that we first consider definition of the variables of motion and the kinematics that these variables may describe. This definition is fundamental for the derivation of model equations that accurately represent the physical phenomena that we wish to capture.

We begin by defining the bristle displacement vector for a single wheel as

$$\boldsymbol{\zeta} \equiv \zeta_x \boldsymbol{i}_w + \zeta_y \boldsymbol{j}_w$$

where $\boldsymbol{i}_w$ and $\boldsymbol{j}_w$ are the unit vectors of a wheel-fixed coordinate frame that is defined identically to the wheel frame of Chapter 2. Here we are not considering the wheel as a subsystem of a vehicle, but rather as an isolated entity. The total derivative of this displacement vector is

$$\begin{aligned} \frac{d\boldsymbol{\zeta}}{dt} &= \dot{\zeta}_x \boldsymbol{i}_w + \dot{\zeta}_y \boldsymbol{j}_w + \omega_z \boldsymbol{k} \times \boldsymbol{\zeta} \\ &= (\dot{\zeta}_x - \omega_z \zeta_y)\boldsymbol{i}_w + (\dot{\zeta}_y + \omega_z \zeta_x)\boldsymbol{j}_w \end{aligned} \tag{40}$$

where $\omega_z$ is the total rotational velocity of the wheel about its $z$-axis. The nonlinear terms present in this derivative are a consequence of the rotation of the coordinate frame with respect to the ground, and arise from time-differentiation of the coordinate frame's unit vectors. Physically, they indicate that changes in the bristle displacement are measured as a consequence of rotation of the measurement frame rather than as a result of changes in the actual displacement. This situation is illustrated in Figure 7, which shows a wheel and bristle in an initial configuration with some bristle displacement, and then after rotation of

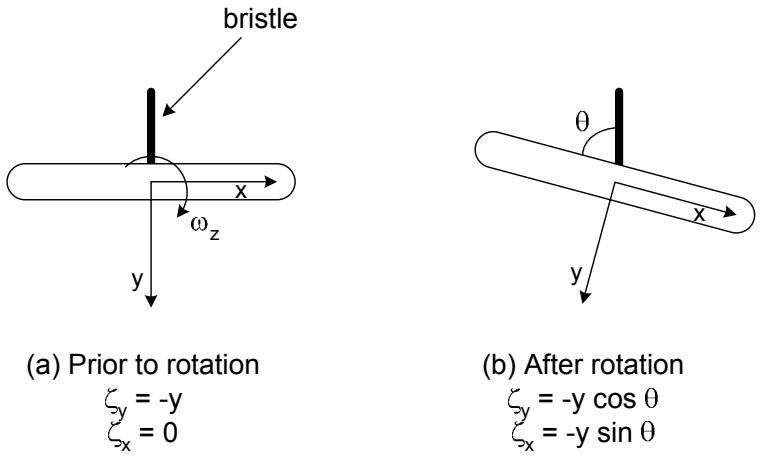


**Figure 7:** Changes in bristle displacement resulting from wheel rotation.

the wheel. We see that the bristle deflection has not changed relative to the road, but that it has changed with respect to the wheel coordinate frame in which it is being measured. This effect, combined with changes in the bristle displacement magnitude, gives rise to the total derivative of the bristle displacement vector.

We now propose that the vector form of the lumped LuGre model dynamics may be written as

$$\dot{\boldsymbol{\zeta}} = -\boldsymbol{v}_r - \frac{\sigma_0 \|\boldsymbol{v}_r\|}{\Gamma(\boldsymbol{v}_r)}\boldsymbol{\zeta} \tag{41}$$

where $\boldsymbol{v}_r$ is the vector relative velocity between the wheel and the road, $\sigma_0$ is the bristle stiffness and $\Gamma(\boldsymbol{v}_r)$ is a function that is defined as

$$\Gamma(\boldsymbol{v}_r) = \mu_d + (\mu_s - \mu_d)e^{-\|\boldsymbol{v}_r/v_s\|^\alpha} \tag{42}$$

where $\mu_d$ and $\mu_s$ are, respectively, the dynamic and static Coulomb friction coefficients, $v_s$ is the Stribeck velocity [2], and $\alpha$ is a shape parameter. This function is shown in Figure 8 for a chosen set of parameters. We see from the figure that the overall effect of $\Gamma(\boldsymbol{v}_r)$ is to produce transitions between $\mu_s$ and $\mu_d$ as a function of the magnitude of the relative velocity between the contact surfaces. The Stribeck velocity and shape parameter thus act only to affect the rate of transition between the static and dynamic friction coefficients.

In order to solve the vector differential equation of (41) for the bristle deflection, we must rewrite the equation in component form so that we instead have a scalar differential

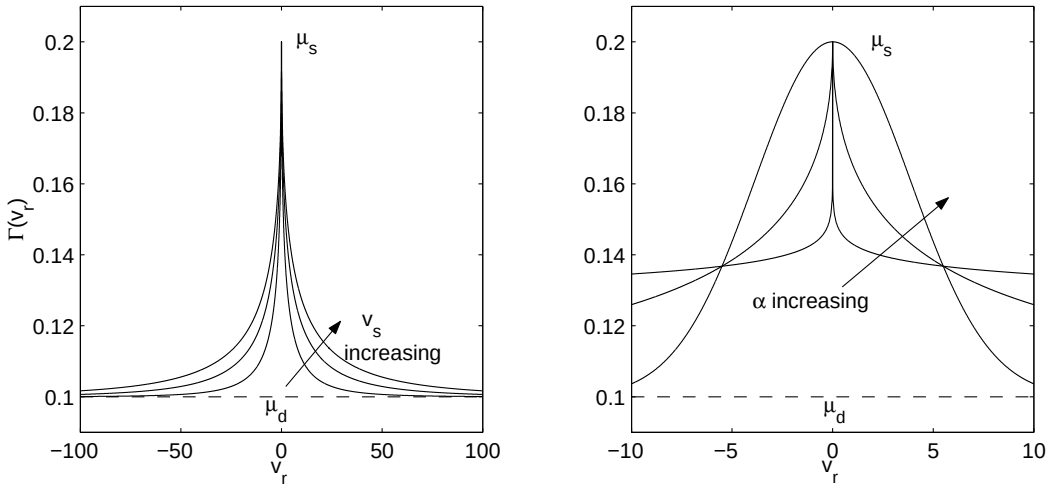


**Figure 8:** The effect of friction parameters on the shape of the friction function $\Gamma(v_r)$.

equation for each component. Since, in general, we will have non-zero angular velocity, we must consider the rotation contribution to the total derivative of the bristle displacement vector that appears on the left-hand side of (41), as discussed above. To do so, we equate (40) and (41), which results in

$$(\dot{\zeta}_x - \omega_z \zeta_y)\boldsymbol{i}_w + (\dot{\zeta}_y + \omega_z \zeta_x)\boldsymbol{j}_w = -\boldsymbol{v}_r - \frac{\sigma_0 \left\| \boldsymbol{v}_r \right\|}{\Gamma(\boldsymbol{v}_r)}\boldsymbol{\zeta}$$

Separation of this expression into components and regrouping yields the two coupled scalar differential equations for bristle deflection

$$\begin{aligned} \dot{\zeta}_x &= -v_{rx} - \tfrac{\sigma_0 \|\boldsymbol{v}_r\|}{\Gamma(\boldsymbol{v}_r)}\zeta_x + \omega_z \zeta_y \\ \dot{\zeta}_y &= -v_{ry} - \tfrac{\sigma_0 \|\boldsymbol{v}_r\|}{\Gamma(\boldsymbol{v}_r)}\zeta_y - \omega_z \zeta_x \end{aligned} \tag{43}$$

where the rotational effect on the bristle dynamics is now more apparent. The implication of the coupling terms on the right-hand side is that rotation of the wheel acts to transfer bristle displacement from one axis to another.

We must be careful not to confuse the derivatives of the bristle displacement vector *components* on the left-hand side of Equation (43) with the total derivative of the bristle displacement *vector*. The derivatives in (43) are derivatives with respect to the moving wheel coordinate frame and not the derivative of the displacement with respect to the stationary earth frame as in Equation (41). Let us define $\partial\boldsymbol{\zeta} \equiv [\dot{\zeta}_x, \dot{\zeta}_y]^T$, where we have

used the partial differential operator since this vector does not represent the total motion of the bristle, but only the portion of the motion that occurs with respect to the wheel frame.

Now that we have formulated the friction model dynamics, we may specify the model's output equation. We recall that this output must be a unitless multiplier of normal force. Following the form of the one-dimensional LuGre model, we suggest that this output equation should be

$$\boldsymbol{\mu} = \sigma_0 \boldsymbol{\zeta} + \sigma_1 \dot{\boldsymbol{\zeta}} + \sigma_2 \boldsymbol{v}_r \tag{44}$$

where $\sigma_0$ is the same bristle stiffness that appeared in the dynamical equation, and $\sigma_1$ and $\sigma_2$ are damping and viscous friction parameters, respectively.

Note that the friction output function has dependence on the absolute bristle velocity, $\dot{\boldsymbol{\zeta}}$, rather than on the velocity with respect to the wheel frame, $\partial\boldsymbol{\zeta}$. This indicates that bristle damping is produced by motion of the bristle with respect to the ground, but measured in the wheel frame, rather than by bristle motion with respect to the wheel. Figure 9 demonstrates that this is, in fact, the case.

We see in Figure 9a that the bristle model is represented as a spring and damper in parallel, fixed to the wheel at one end and the bristle tip at the opposite end. The bristle is initially aligned along the wheel frame $x$-axis and the tip of the bristle is in motion along the same axis. Figure 9b shows the next time instant, after an incremental wheel rotation. We now see the absolute position increment of the bristle, $\delta x$, and the position increments with respect to the wheel frame, $\delta x_w$ and $\delta y_w$. It is clear from this diagram that only $\delta x$ would produce damping force, confirming the proposed output equation of (44).

We will see in the next section that despite damping dependence only on absolute motion, the orientation of the bristle motion with respect to the wheel does potentially affect the dynamics.

### 3.1.2 Two-Dimensional Bristle Parameters

Thus far, we have treated the bristle stiffness and damping parameters as scalar constants. This imposes a requirement that the bristle be equally stiff and provide equal amounts of damping in every deflection direction. We know from the field of material mechanics

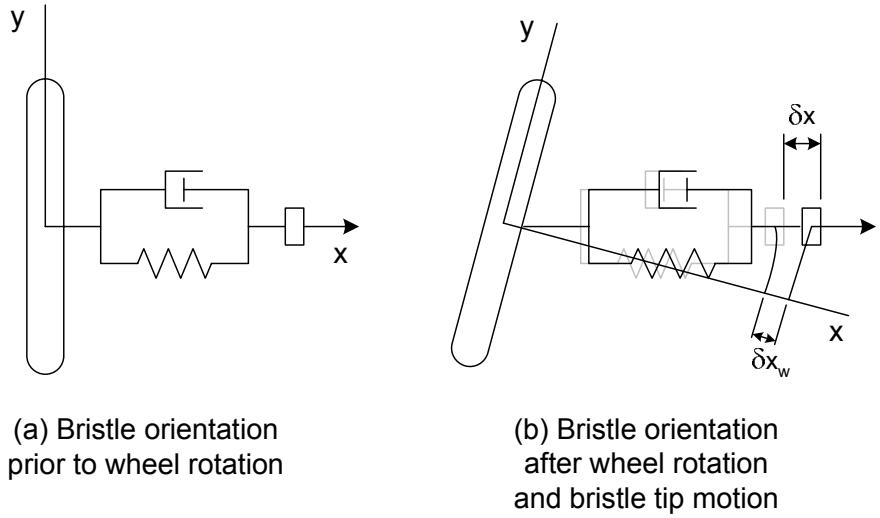


**Figure 9:** Two-dimensional incremental bristle motion.

that this is not necessarily the case for a beam in pure bending [3, Chap. 4], and the bristle may be viewed as such. A complete extension of the LuGre model to the two-dimensional case therefore requires consideration of directionally dependent stiffness and damping parameters. We must therefore rewrite the dynamic equation of (41) and the output equation of (44) as

$$\dot{\boldsymbol{\zeta}} = -\boldsymbol{v}_r - \frac{\sigma_0(\boldsymbol{\zeta})\,\|\boldsymbol{v}_r\|}{\Gamma(\boldsymbol{v}_r)}\boldsymbol{\zeta} \tag{45}$$

$$\boldsymbol{\mu} = \sigma_0(\boldsymbol{\zeta})\boldsymbol{\zeta} + \sigma_1(\dot{\boldsymbol{\zeta}})\dot{\boldsymbol{\zeta}} + \sigma_2(\boldsymbol{v}_r)\boldsymbol{v}_r \tag{46}$$

with the $\sigma$ parameters now as functions of the vectors that they precede, but with scalar output.

We recognize that the mechanical bending properties of a beam are dependent on the cross-sectional shape of the beam [3]. Since the friction bristles may have arbitrary cross-sectional shape that is unknown, we must approximate the variation of the stiffness and damping parameters in some continuous fashion. We therefore choose to specify the values of each $\sigma$ function along the two primary wheel axes as $\sigma_x$ and $\sigma_y$, and connect these values with an ellipse. Then we may select the value of each $\sigma$, at any instant, as the radius of the ellipse in the direction of the vector of interest as shown in Figure 10.

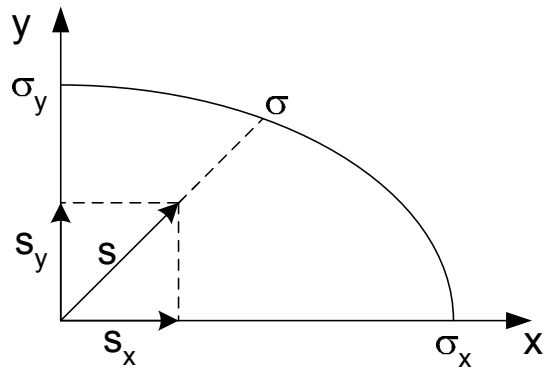


**Figure 10:** Ellipse method for two-dimensional stiffness and damping.

The equation for the ellipse in $x$ and $y$ coordinates is

$$\frac{x^2}{\sigma_x^2} + \frac{y^2}{\sigma_y^2} = 1 \tag{47}$$

where $\sigma_x$ and $\sigma_y$ are the radii of the ellipse along their respective axes. The direction for which we seek the ellipse radius is determined by the relevant vector ($\boldsymbol{\zeta}$, $\dot{\boldsymbol{\zeta}}$, or $\boldsymbol{v}_r$), which for generality we shall call $\boldsymbol{s}$, with components $s_x$ and $s_y$. Then the geometry requires that the ratios of each ellipse coordinate to the component of $\boldsymbol{s}$ in that coordinate be equal so that

$$\frac{x}{s_x} = \frac{y}{s_y}$$
$$x^2 = y^2 \frac{s_x^2}{s_y^2}$$

Substituting this into (47) and solving for $x^2$ and $y^2$, we have that

$$\begin{aligned} y^2 &= \frac{s_y^2 \sigma_x^2 \sigma_y^2}{s_x^2 \sigma_y^2 + s_y^2 \sigma_x^2} \\ x^2 &= \frac{s_x^2 \sigma_x^2 \sigma_y^2}{s_x^2 \sigma_y^2 + s_y^2 \sigma_x^2} \end{aligned}$$

Finally, the radius is

$$\begin{aligned} \sigma &= \sqrt{x^2 + y^2} \\ &= \sigma_x \sigma_y \sqrt{\frac{s_x^2 + s_y^2}{s_x^2 \sigma_y^2 + s_y^2 \sigma_x^2}} \end{aligned} \tag{48}$$

and we may find the functions for $\sigma_0$, $\sigma_1$, or $\sigma_2$ by respective substitution of $\boldsymbol{\zeta}$, $\dot{\boldsymbol{\zeta}}$, or $\boldsymbol{v}_r$ for $\boldsymbol{s}$. These functions should then be applied in the modified dynamic and output equations of (45)-(46).

This procedure may be generalized further to allow for non-symmetric directional dependence of the damping parameter by allowing for a different ellipse shape in each quadrant through specification of different damping parameters along the negative axes. In addition, non-elliptical directional dependencies may be approximated by the superposition of multiple ellipses of differing eccentricities. That is, we would have a series of equations of the form of (48), with different $\sigma_x$ and $\sigma_y$ parameters that would be evaluated and summed to give an aggregate result. In this way, we could characterize and model more complex variations in stiffness and damping and achieve a better approximation of the actual variation. Such a method, however, would be burdensome and we therefore limit our approach to consideration of a single ellipse. We also recognize that tire geometry suggests that the majority of parameter variation would occur between the two primary axes so that independent specification of the parameters along only these axes as we have shown here makes intuitive sense.

Note that this ellipse method provides a first-order approximation to the actual variation of the stiffness and damping parameters as a function of the direction of motion. For simplicity, we may choose to sacrifice directional dependence and approximate these characteristics as circles rather than ellipses so that the parameters become scalar constants. The constant parameters should then represent the average value of the actual variation over all bristle directions.

## *3.2 LuGre Model Steady State*

A steady-state analysis of the proposed two-dimensional LuGre model of (45)-(46), (48) may provide greater insight into the nature of the model. For any dynamical system, a steady-state operating point represents a purely kinematic form of the system in which the dynamics do not occur. Thus, examination of the steady state allows us to reduce our differential equations to algebraic equations so that we may examine system behavior in an

approximate sense.

We begin our steady-state analysis by setting $\dot{\boldsymbol{\zeta}}$ equal to zero and $\boldsymbol{\zeta} = \boldsymbol{\zeta}_{ss}$ in the dynamic equation of (45). Solving for the steady-state bristle deflection, we have

$$\boldsymbol{\zeta}_{ss} = -\frac{\Gamma(\boldsymbol{v}_r)}{\sigma(\boldsymbol{\zeta})}\frac{\boldsymbol{v}_r}{\|\boldsymbol{v}_r\|} \tag{49}$$

Now we may substitute this result for $\boldsymbol{\zeta}$ into the output equation of (46), and again set $\dot{\boldsymbol{\zeta}}$ equal to zero to achieve the steady-state friction force model

$$\boldsymbol{\mu} = -\Gamma(\boldsymbol{v}_r)\frac{\boldsymbol{v}_r}{\|\boldsymbol{v}_r\|} \tag{50}$$

where we have chosen to drop the viscous friction term since, for dry contact, $\sigma_2$ will typically be very small or zero.

We must examine these force multipliers for limiting cases of $\boldsymbol{v}_r$ to determine if this model has the desired steady-state behavior. To do so, we recognize that $v_{r,x}/\|\boldsymbol{v}_r\|$ and $v_{r,y}/\|\boldsymbol{v}_r\|$ are the sine and cosine, respectively, of the angle that the $\boldsymbol{v}_r$ vector makes with the wheel frame $x$-axis. If we denote this angle as $\psi$, then the steady-state output equation may be rewritten in component form as

$$\begin{aligned} \mu_x &= -\Gamma(\boldsymbol{v}_r)\cos\psi \\ \mu_y &= -\Gamma(\boldsymbol{v}_r)\sin\psi \end{aligned}$$

Then, taking the limit of $\Gamma(\boldsymbol{v}_r)$ as $\boldsymbol{v}_r$ approaches the zero vector

$$\lim_{v_r \to 0} \Gamma(\boldsymbol{v}_r) \to \mu_s$$

and we have that

$$\mu_x = -\mu_s \cos\psi \tag{51}$$

$$\mu_y = -\mu_s \sin\psi \tag{52}$$

Since the $\boldsymbol{v}_r$ vector has vanished, $\psi$ is not well defined. However, we may interpret the result to mean that at the instant that motion begins or ceases, the friction coefficient function is equal in magnitude to $\mu_s$ and opposite to the direction of motion. This is the case for

$\boldsymbol{v}_r$ approaching zero, however, if we wish to know what the friction coefficient is for $\boldsymbol{v}_r$ identically equal to zero, me must reconsider (45).

Examination of the dynamical equation reveals that $\boldsymbol{v}_r = 0$ implies that $\dot{\boldsymbol{\zeta}} = 0$, and steady-state operation is thus guaranteed regardless of the vector $\boldsymbol{\zeta}$. The output equation then becomes

$$\boldsymbol{\mu} = \sigma_0(\boldsymbol{\zeta})\boldsymbol{\zeta}_{ss} \tag{53}$$

where $\boldsymbol{\zeta}_{ss}$ is now simply equal to whatever it was when the relative velocity disappeared. In this way, the force is able to take on any magnitude necessary to maintain zero relative velocity by achieving the necessary bristle deflection.

The zero relative velocity steady-state case of the lumped LuGre model is only subtly different than the static friction Coulomb model. First, the friction coefficient is not bounded in magnitude by $\mu_s$ for static friction as is the case for Coulomb friction. Rather, the LuGre model indicates that at the instant of appearance of relative velocity, the friction coefficient is equal in magnitude to $\mu_s$. Second, and perhaps more subtle, is that transitions to and from static friction are determined solely by the relative velocity at the point of contact rather than whether the applied force remains within a necessary bound.

Returning to the analysis, we must consider the case of steady-state motion where $\|\boldsymbol{v}_r\|$ is very large. Now we have that $\Gamma(\boldsymbol{v}_r) \to \mu_d$ so that

$$\boldsymbol{\mu} = -\mu_d \frac{\boldsymbol{v}_r}{\|\boldsymbol{v}_r\|} \tag{54}$$

which is identical to the dynamic friction Coulomb model for two-dimensional motion. That is, the friction coefficient has magnitude $\mu_d$ and its direction is opposite to that of the motion.

It is common in the tire friction literature to express the lateral wheel friction coefficient as a function of wheel slip angle and the longitudinal friction coefficient as a function of slip ratio [35]. Slip angle is the angle between the direction of motion of the wheel and the wheel's longitudinal axis as shown in Figure 11, while slip ratio is the ratio of the $x$-component relative velocity to the velocity of the wheel center in the $x$-direction. Let us denote slip angle as $\beta$, slip ratio as $\kappa$ and the forward wheel velocity as $v_x$. Now we may

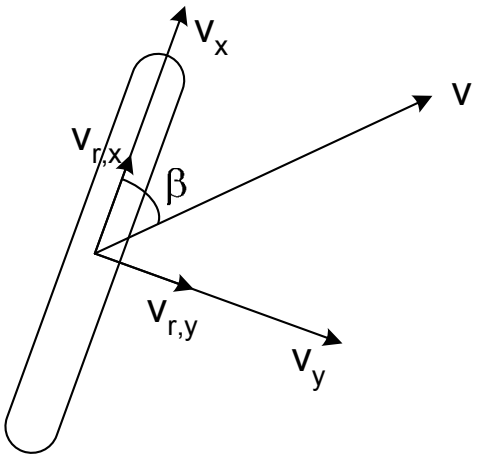


**Figure 11:** Slip angle definition.

write the mathematical definitions of slip angle and slip rate as

$$\tan\beta = \frac{v_{r,y}}{v_x} \tag{55}$$

$$\kappa = \frac{v_{r,x}}{v_x} \tag{56}$$

We may use these equations to express $\|\boldsymbol{v}_r\|$ as

$$\|\boldsymbol{v}_r\| = v_x\sqrt{\tan^2\beta + \kappa^2} \tag{57}$$

and finally, we may rewrite the steady state force coefficient of (50) as

$$\boldsymbol{\mu} = -\frac{\mu_d + (\mu_s - \mu_d)e^{-(v_x\sqrt{\tan^2\beta+\kappa^2}/v_s)^\alpha}}{\sqrt{\tan^2\beta + \kappa^2}} \begin{bmatrix} \tan\beta \\ \kappa \end{bmatrix} \tag{58}$$

where we have written out $\Gamma$ in its entirety, now as a function of $v_x$, $\beta$, and $\kappa$.

We select LuGre model parameters as in Table 1, set $\kappa = 0.005$ and $v_x = 20$ m/s, and plot $\mu_y$ as a function of $\beta$. Then, we alternatively set $\tan\beta = 0.01$ and $v_x = 10$ m/s, and plot $\mu_x$ as a function of $\kappa$. The results are shown in Figure 12 and we see that these curves match the characteristic shape of the Pacejka's Magic Formula model very well [35]. Thus, by selecting appropriate parameters for the LuGre model, we can achieve excellent fits to experimental steady-state data.

**Table 1:** Parameters used for steady state model evaluation.

| Parameter | Value |
|---|---|
| $\mu_d$ | 0.8 |
| $\mu_s$ | 1.5 |
| $v_s$ | 5.5 m/s |
| $\alpha$ | 0.5 |

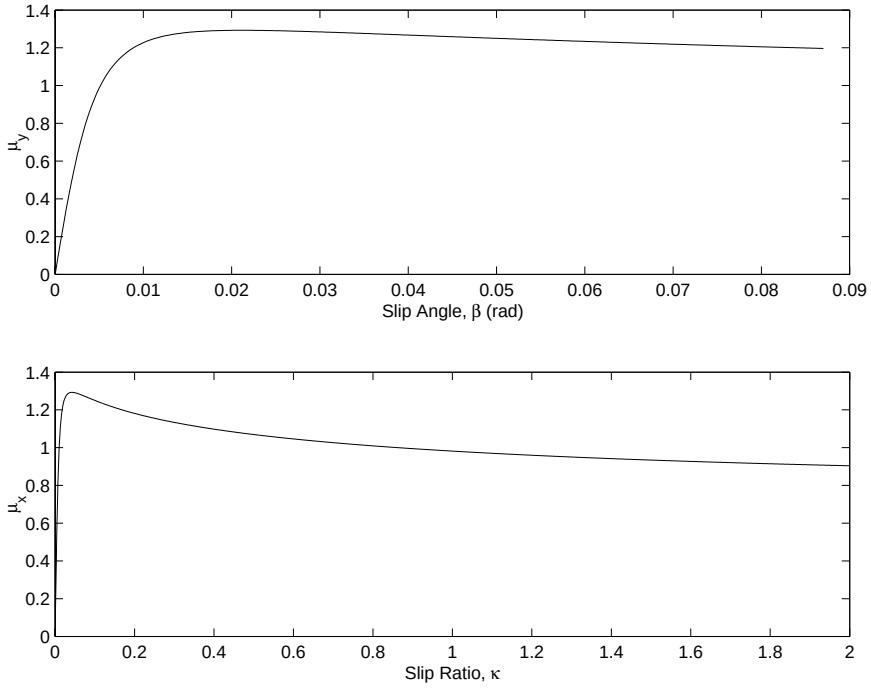


**Figure 12:** Steady-state friction force coefficients as a function of slip angle, $\beta$, and slip ratio, $\kappa$.

# CHAPTER IV

# THE VEHICLE MODEL

We have now developed all of the components necessary for a vehicle dynamic model, yet we have not assembled them into a useful form. We desire a state-variable representation which will allow us to easily simulate the vehicle motion on a computer by means of numerical integration. We will therefore now undertake to synthesize the complete vehicle model and to demonstrate the model functionality via simulation.

## *4.1 Nonlinear Model*

### 4.1.1 Friction Matrices

Recall from Chapter 2 that (38) and (39) fully define the motion of the vehicle body and wheels, except for specification of the matrices $\boldsymbol{\mu}_x$ and $\boldsymbol{\mu}_y$. We will now employ the results of Chapter 3 to construct these matrices.

We begin by defining bristle displacement vectors $\boldsymbol{\zeta}_n$ for $n = 1, \ldots, 4$ for each wheel. Then the $n$th dynamical bristle equation is

$$\dot{\boldsymbol{\zeta}}_n = -\boldsymbol{v}_{r,n} - \frac{\sigma_{0,n}(\boldsymbol{\zeta}_n)\|\boldsymbol{v}_{r,n}\|}{\Gamma(\boldsymbol{v}_{r,n})}\boldsymbol{\zeta}_n \tag{59}$$

for $n = 1, \ldots, 4$, where $\boldsymbol{v}_{r,n}$ is the relative velocity of the $n$th wheel contact point as defined in Chapter 2. Note here that $\sigma_0$ is not only specified as a function of the $n$th bristle deflection vector, but is also possibly a different function for each wheel as indicated by the subscript $n$. In addition, we define the $n$th friction coefficient function as

$$\boldsymbol{\mu}_n = \sigma_{0,n}(\boldsymbol{\zeta}_n)\boldsymbol{\zeta}_n + \sigma_{1,n}(\dot{\boldsymbol{\zeta}}_n)\dot{\boldsymbol{\zeta}}_n + \sigma_{2,n}(\boldsymbol{v}_{r,n})\boldsymbol{v}_{r,n} \tag{60}$$

where we have again allowed for different $\sigma$ specifications for each wheel. Now we may define the vectors

$$\boldsymbol{\mu}_x^* = [\boldsymbol{\mu}_1 \cdot \boldsymbol{i}_1, \ldots, \boldsymbol{\mu}_4 \cdot \boldsymbol{i}_4]^T \tag{61}$$

$$\boldsymbol{\mu}_y^* = [\boldsymbol{\mu}_1 \cdot \boldsymbol{j}_1, \ldots, \boldsymbol{\mu}_4 \cdot \boldsymbol{j}_4]^T \tag{62}$$

where the unit vectors $\boldsymbol{i}_n$ and $\boldsymbol{j}_n$, $n = 1, \ldots, 4$ are the wheel frame unit vectors of Chapter 2. This definition has separated the friction output equations into vectors of $x$ and $y$ component output equations. This now allows us to write

$$\boldsymbol{\mu}_x = \text{diag}(\boldsymbol{\mu}_x^*) \tag{63}$$

$$\boldsymbol{\mu}_y = \text{diag}(\boldsymbol{\mu}_y^*) \tag{64}$$

which are the friction matrices whose definition we sought.

### 4.1.2 Model Summary

We now seek to express the dynamical equations of the entire vehicle system in a compact form. Notice in (59) and (60) that no specific $\boldsymbol{\xi}$ or $\boldsymbol{\nu}$ dependence is demonstrated, however, this dependence is uniquely present as a result of the occurrence of $\boldsymbol{v}_{r,n}$ in these equations. Restating the result of (6) for the relative velocity of the contact point of wheel $n$ from Chapter 2, we have

$$\begin{aligned} \boldsymbol{v}_{r,n} = & \left[(v_x - \omega_v y_n)\cos\theta_n + (v_y + \omega_v x_n)\sin\theta_n + \omega_{w,n} r\right] \boldsymbol{i}_n \\ & + \left[(v_y + \omega_v x_n)\cos\theta_n - (v_x - \omega_v y_n)\sin\theta_n\right] \boldsymbol{j}_n \end{aligned} \tag{65}$$

and we observe that the relative velocity is a linear function of the state variables. Now define $\boldsymbol{v}_r(\boldsymbol{\xi}, \boldsymbol{\nu}, \boldsymbol{\theta}) = [\boldsymbol{v}_{rx,1}, \ldots, \boldsymbol{v}_{rx,4}, \boldsymbol{v}_{ry,1}, \ldots, \boldsymbol{v}_{ry,4}]^T$, which is an $8 \times 1$ vector of the $x$- and $y$-component relative velocities for each wheel. This vector may now be written as

$$\boldsymbol{v}_r(\boldsymbol{\xi}, \boldsymbol{\nu}, \boldsymbol{\theta}) = \boldsymbol{\Xi}(\boldsymbol{\theta})\boldsymbol{\xi} + \boldsymbol{V}\boldsymbol{\nu} \tag{66}$$

where

$$\boldsymbol{\Xi}(\boldsymbol{\theta}) = \begin{bmatrix} \boldsymbol{\lambda}_c(\boldsymbol{\theta}) & \boldsymbol{\lambda}_s(\boldsymbol{\theta}) & \boldsymbol{x}\boldsymbol{\lambda}_s(\boldsymbol{\theta}) - \boldsymbol{y}\boldsymbol{\lambda}_c(\boldsymbol{\theta}) \\ -\boldsymbol{\lambda}_s(\boldsymbol{\theta}) & \boldsymbol{\lambda}_c(\boldsymbol{\theta}) & \boldsymbol{x}\boldsymbol{\lambda}_c(\boldsymbol{\theta}) + \boldsymbol{y}\boldsymbol{\lambda}_s(\boldsymbol{\theta}) \end{bmatrix} \tag{67}$$

with $\boldsymbol{\lambda}_c(\boldsymbol{\theta})$, $\boldsymbol{\lambda}_s(\boldsymbol{\theta})$, $\boldsymbol{x}$, and $\boldsymbol{y}$ as defined in Chapter 2 and

$$\boldsymbol{V} = \begin{bmatrix} r\boldsymbol{I}_4 \\ \boldsymbol{0}_4 \end{bmatrix} \tag{68}$$

We also define the vector $\boldsymbol{\zeta} = [\zeta_{x,1}, \ldots, \zeta_{x,4}, \zeta_{y,1}, \ldots, \zeta_{y,4}]^T$, which allows us to write the bristle dynamical equations of (59) in combined form as

$$\dot{\boldsymbol{\zeta}} = -\boldsymbol{\Xi}(\boldsymbol{\theta})\boldsymbol{\xi} - \boldsymbol{V}\boldsymbol{\nu} - \boldsymbol{Z}(\boldsymbol{\xi}, \boldsymbol{\nu}, \boldsymbol{\theta}, \dot{\boldsymbol{\theta}})\boldsymbol{\zeta} \tag{69}$$

where $\dot{\boldsymbol{\zeta}} = [\partial\zeta_{x,1}, \ldots, \partial\zeta_{x,4}, \partial\zeta_{y,1}, \ldots, \partial\zeta_{y,4}]^T$ is the vector of bristle deflection rates with respect to the vehicle frame as discussed in Chapter 3, and

$$\boldsymbol{Z}(\boldsymbol{\xi}, \boldsymbol{\nu}, \boldsymbol{\theta}, \dot{\boldsymbol{\theta}}) = \begin{bmatrix} \boldsymbol{Z}_{xx} & -\boldsymbol{Z}_{xy} \\ \boldsymbol{Z}_{yx} & \boldsymbol{Z}_{yy} \end{bmatrix} \tag{70}$$

is the matrix with submatrices

$$\boldsymbol{Z}_{xx} = \boldsymbol{Z}_{yy} = \operatorname{diag}\left( \frac{\sigma_{0,1}\|\boldsymbol{v}_{r,1}\|}{\Gamma(\boldsymbol{v}_{r,1})}, \ldots, \frac{\sigma_{0,4}\|\boldsymbol{v}_{r,4}\|}{\Gamma(\boldsymbol{v}_{r,4})} \right) \tag{71}$$

$$\boldsymbol{Z}_{xy} = \boldsymbol{Z}_{yx} = \omega_v \boldsymbol{I}_4 + \operatorname{diag}(\dot{\boldsymbol{\theta}}) \tag{72}$$

where the functional dependencies on $\boldsymbol{\xi}$ and $\boldsymbol{\nu}$ are understood and are omitted for the sake of notational brevity. Also note that we have neglected to show that $\sigma_{0,n}$ might have functional dependence on $\boldsymbol{\zeta}$, as described in Chapter 3, which would create additional dependence of $\boldsymbol{Z}$ on $\boldsymbol{\zeta}$.

Our definitions now allow us to summarize the entire vehicle dynamic model, including the effect of friction, as

$$\boldsymbol{M}_1\dot{\boldsymbol{\xi}} = \boldsymbol{\eta}(\boldsymbol{\xi}) + \boldsymbol{A}(\boldsymbol{\xi}, \boldsymbol{\nu}, \boldsymbol{\zeta}, \boldsymbol{\theta})\boldsymbol{P}^{-1}(\boldsymbol{\xi}, \boldsymbol{\nu}, \boldsymbol{\zeta}, \boldsymbol{\theta})\boldsymbol{c} \tag{73}$$

$$\boldsymbol{M}_2\dot{\boldsymbol{\nu}} = r\boldsymbol{\mu}_x(\boldsymbol{\xi}, \boldsymbol{\nu}, \boldsymbol{\zeta})\boldsymbol{P}^{-1}(\boldsymbol{\xi}, \boldsymbol{\nu}, \boldsymbol{\zeta}, \boldsymbol{\theta})\boldsymbol{c} + \boldsymbol{\tau} \tag{74}$$

$$\dot{\boldsymbol{\zeta}} = -\boldsymbol{\Xi}(\boldsymbol{\theta})\boldsymbol{\xi} - \boldsymbol{V}\boldsymbol{\nu} - \boldsymbol{Z}(\boldsymbol{\xi}, \boldsymbol{\nu}, \boldsymbol{\theta}, \dot{\boldsymbol{\theta}})\boldsymbol{\zeta} \tag{75}$$

where

$$\boldsymbol{A}(\boldsymbol{\xi}, \boldsymbol{\nu}, \boldsymbol{\zeta}, \boldsymbol{\theta}) = \boldsymbol{A}_x(\boldsymbol{\theta})\boldsymbol{\mu}_x(\boldsymbol{\xi}, \boldsymbol{\nu}, \boldsymbol{\zeta}) + \boldsymbol{A}_y(\boldsymbol{\theta})\boldsymbol{\mu}_y(\boldsymbol{\xi}, \boldsymbol{\nu}, \boldsymbol{\zeta}) \tag{76}$$

$$\boldsymbol{P}(\boldsymbol{\xi}, \boldsymbol{\nu}, \boldsymbol{\zeta}, \boldsymbol{\theta}) = \boldsymbol{I}_4 - \boldsymbol{P}_x(\boldsymbol{\theta})\boldsymbol{\mu}_x(\boldsymbol{\xi}, \boldsymbol{\nu}, \boldsymbol{\zeta}) - \boldsymbol{P}_y(\boldsymbol{\theta})\boldsymbol{\mu}_y(\boldsymbol{\xi}, \boldsymbol{\nu}, \boldsymbol{\zeta}) \tag{77}$$

Equations (73)-(75) are 15 coupled ordinary differential equations in 15 state variables. These equations may now be numerically integrated with a given steering trajectory and torque inputs to simulate motion of the vehicle system.

Our assumption of the invertibility of the matrix $\boldsymbol{P}$ in (73) and (74) is at the heart of our ability to solve the system of ODEs. Failure to invert the matrix is a failure of the model and we state the following theorem to address this difficulty.

**Theorem 1** *For any* $\boldsymbol{\xi}_0, \boldsymbol{\nu}_0, \boldsymbol{\zeta}_0, \boldsymbol{\theta}_0$ *such that* $\boldsymbol{v}_r(\boldsymbol{\xi}_0, \boldsymbol{\nu}_0, \boldsymbol{\theta}_0) = 0$ *and* $\boldsymbol{\zeta}_0 = 0$*, there exists some* $C \subset \mathcal{R}^3 \times \mathcal{R}^4 \times \mathcal{R}^8 \times \mathcal{R}^4$ *with* $\{\boldsymbol{\xi}_0, \boldsymbol{\nu}_0, \boldsymbol{\zeta}_0, \boldsymbol{\theta}_0\} \in C$ *such that* $\boldsymbol{P}^{-1}(\boldsymbol{\xi}, \boldsymbol{\nu}, \boldsymbol{\zeta}, \boldsymbol{\theta})$ *exists for all* $(\boldsymbol{\xi}, \boldsymbol{\nu}, \boldsymbol{\zeta}, \boldsymbol{\theta}) \in C$*.*

**Proof:** According to (60)-(64), the hypotheses $\boldsymbol{v}_r = 0$ and $\boldsymbol{\zeta} = 0$ imply that $\boldsymbol{\mu}_x = \boldsymbol{\mu}_y = 0$, which further implies $\boldsymbol{P} = \boldsymbol{I}_4$, according to (77). Since $\boldsymbol{P}$ is a continuous function of $(\boldsymbol{\xi}, \boldsymbol{\nu}, \boldsymbol{\zeta}, \boldsymbol{\theta})$, it follows that $\boldsymbol{P}$ is invertible in some neighborhood of this point. □

Thus, if we initialize the system at one of these zero relative velocity, zero bristle deflection points, we know that a solution is possible in some neighborhood of that initialization. This is easily done by selecting zero steer angle for all of the wheels, zero lateral velocity, and zero angular velocity. Then we select all of the wheel angular velocities equal to the longitudinal velocity divided by the wheel radius: $\xi_1/r$. With the bristle deflections also set to zero, such a choice of initial state is an equilibrium point for the system, and the system will retain this state as long as no input is applied.

This result suggests only that inversion of the matrix $\boldsymbol{P}$ is possible, but provides no information about the extent of deviation from the zero relative velocity, zero bristle deflection condition that is allowable. Equation (25) of Chapter 2, however, suggests a solution to this difficulty. We recognize that this equation indicates that a nearly singular $\boldsymbol{P}$ matrix would produce extremely high normal forces. The normal force for any given wheel, however, is bounded by the total weight of the vehicle, thus solutions that exceed this bound may only be generated by producing negative normal forces at other wheels. This occurrence is non-physical and we may therefore avoid both non-invertibility of $\boldsymbol{P}$ and impermissible solutions by monitoring the normal forces produced during state-derivative integration, and halt the integration as required.

**Table 2:** Model parameters for simulation.

| Parameter | Value |
|---|---|
| Inertial Parameters | |
| $m_v$ | 907.1890 kg |
| $I_v$ | 514.0709 kg m$^2$ |
| $I_w$ | 0.1361 kg m$^2$ |
| Geometric Parameters | |
| $r$ | 0.2 m |
| $h$ | 0.5 m |
| $x_1$ | 1.2 m |
| $x_2$ | 1.2 m |
| $x_3$ | -1 m |
| $x_4$ | -1 m |
| $y_1$ | -0.7 m |
| $y_2$ | 0.7 m |
| $y_3$ | -0.7 m |
| $y_4$ | 0.7 m |
| Friction Parameters | |
| $\sigma_{0,x}$ | 178 m$^{-1}$ |
| $\sigma_{1,x}$ | 1 s/m |
| $\sigma_{2,x}$ | 0 s/m |
| $\sigma_{0,y}$ | 500 m$^{-1}$ |
| $\sigma_{1,y}$ | 2 s/m |
| $\sigma_{2,y}$ | 0 s/m |
| $v_s$ | 5.5 m/s |

## *4.2 Simulation and Results*

We may now simulate the vehicle system by implementing a solution of (73)-(75) in MATLAB. For this purpose, we utilize the model parameters listed in Table 2. The friction parameters that are specified along the longitudinal wheel axis as well as the Stribeck velocity are taken from [8]. For the lateral bristle stiffness and damping, we specify larger values to achieve faster response in the lateral direction. Vehicle mass, inertia, and geometry parameters are chosen to emulate a mid-sized passenger car.

The vehicle body states may also be integrated to obtain the absolute vehicle position for simulation output. Since the vehicle body states are measured in the vehicle coordinate frame, a transformation is necessary prior to integration. This transformation is

$$\dot{x}_v \quad = \quad \xi_1 \cos\varphi + \xi_2 \sin\varphi$$

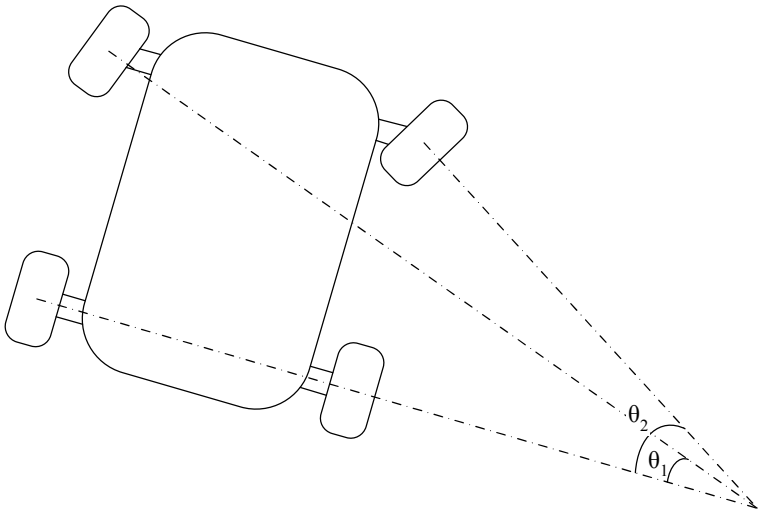


**Figure 13:** Vehicle steering geometry definition.

$$\begin{aligned} \dot{y}_v &= \xi_1 \sin\varphi - \xi_2 \cos\varphi \\ \dot{\varphi} &= \xi_3 \end{aligned}$$

and integrating these expressions, we have absolute position with respect to the initial position.

It is also necessary to specify steering architecture prior to simulation. The driver inputs a steering wheel angle which must be used to determine road-wheel angle. We now choose to fix the rear steering angles at zero steer, and the front steering angles are constrained so that their $y$ axes intersect the rear wheel rotation axis at the same point, as in Figure 13. The driver input, then, directly determines the angle of the front wheel that is on the side of the vehicle corresponding to the direction that the wheels are turned, and the other front wheel angle is determined by the rotation axis constraint. This is done so that no wheel slip is induced by the steering geometry, allowing for the possibility of zero relative velocity solutions at all four wheels.

The model parameters and simulation conventions have now been completely specified except for the coefficients of friction. These coefficients are environmentally dependent and are selected to approximate different types of driving surfaces. In the following sections, different parameter values are considered and the effect of these choices on the performance of the vehicle is shown.

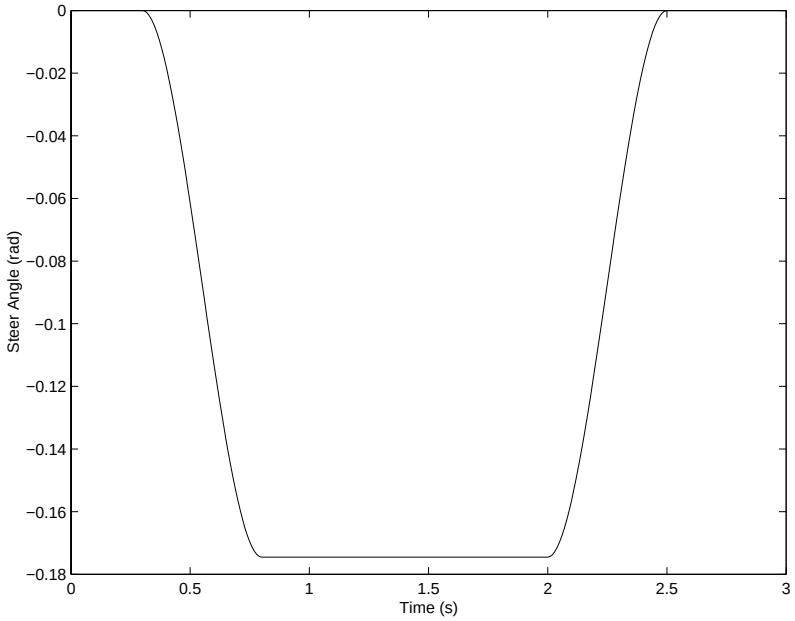


**Figure 14:** Steering input for simulation testing.

### 4.2.1 Normal Road Vehicle Simulation

We first select these coefficients to approximate a dry, moderately high-friction surface such as concrete or asphalt pavement. Appropriate values of the friction coefficients for this case are $\mu_d = 0.8$ and $\mu_s = 1.2$. Employing these values, we now proceed with the simulation of the vehicle.

The driver steering input is selected as in Figure 14 and this input will be used for the remainder of this chapter in order to compare different simulation scenarios. The maneuver consists of zero initial steer, a transition to -10 degrees of steer, and then a return to zero steer, and should cause the vehicle to turn left.

Now, with no torque input at any of the wheels, the simulation is run with an initial longitudinal speed of 15 m/s, and initial wheel speeds of 75 rad/s so that no slip is required. All other states are initialized as zero. The resulting output for the vehicle body velocities is shown in Figure 15. Here we see that the vehicle's speed remains at 15 m/s until the turn begins and friction begins to dissipate energy, resulting in a lower vehicle speed at

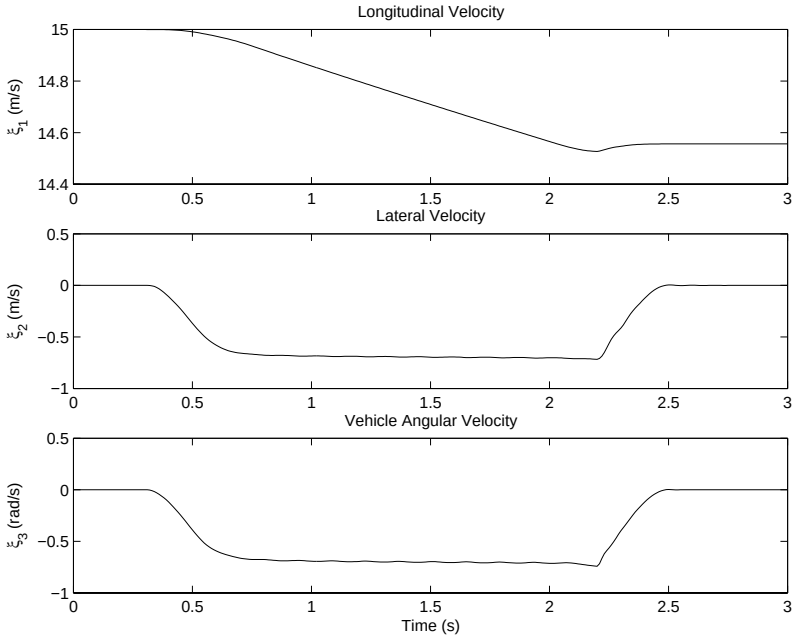


**Figure 15:** Vehicle body velocities for normal road turn maneuver.

the completion of the turn. The vehicle body lateral velocity increases with the steering as does the angular velocity and both return to zero at the completion of the steering input. This results in the vehicle path shown in Figure 16, where the vehicle position is initially at the origin, and the circles indicate the front of the vehicle. The path conforms to our expectation that the vehicle would turn left and then move straight forward once the steering input ceases.

We may also examine plots of the bristle deflection. These are shown in Figure 17 for the left wheels of the vehicle, and reveal that the bristles deflect laterally when steering begins, as a result of relative velocity, and then attain steady-state values as the steer angle is held fixed. Finally, the bristles return to zero lateral deflection when the maneuver is complete. Oscillation of the bristles may be observed, which is a result of relative velocity oscillating about zero. This is seen in Figure 18 which shows the relative velocity for the wheels on the left side of the vehicle. The left rear wheel lateral relative velocity in the lower right plot oscillates through zero, while the front wheel sustains higher relative velocity and thus does not cause bristle oscillation.

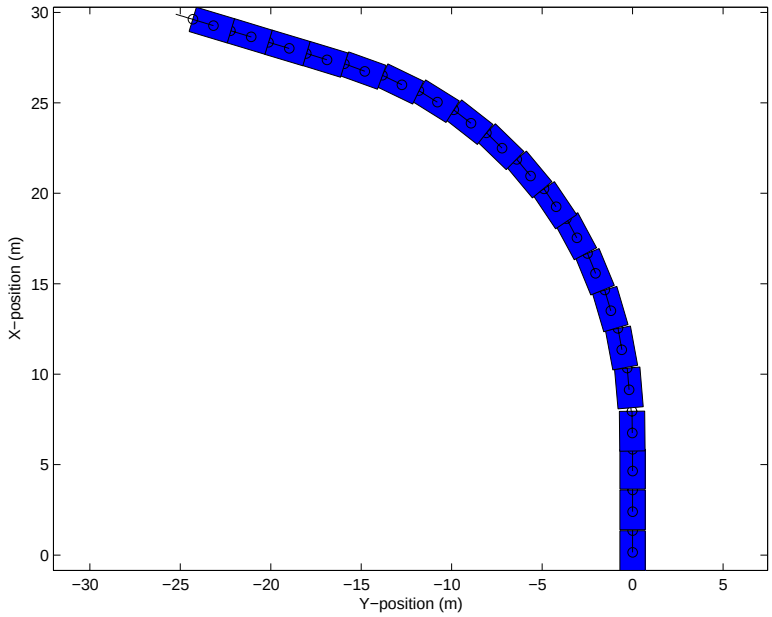


**Figure 16:** Vehicle position for normal road turn maneuver.

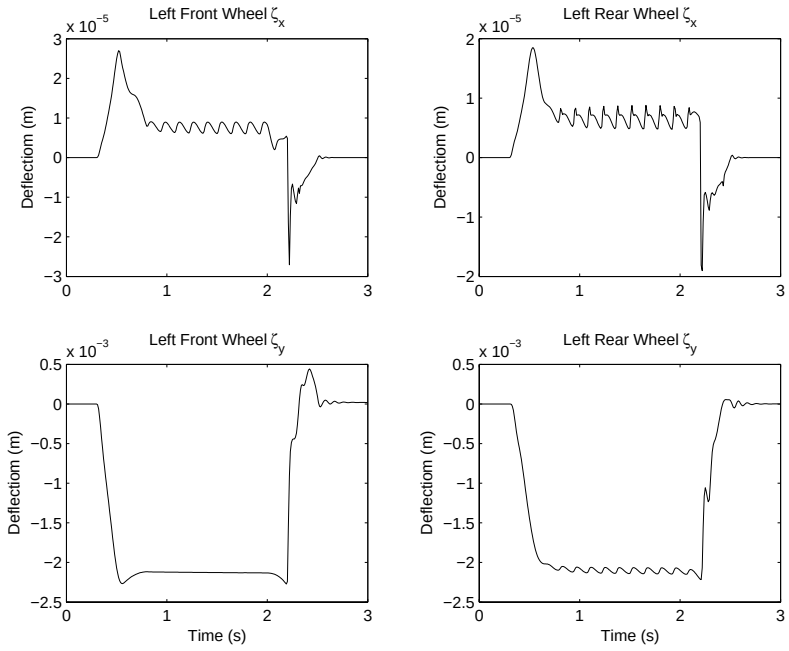


**Figure 17:** Lateral bristle deflection during turn maneuver on normal road.

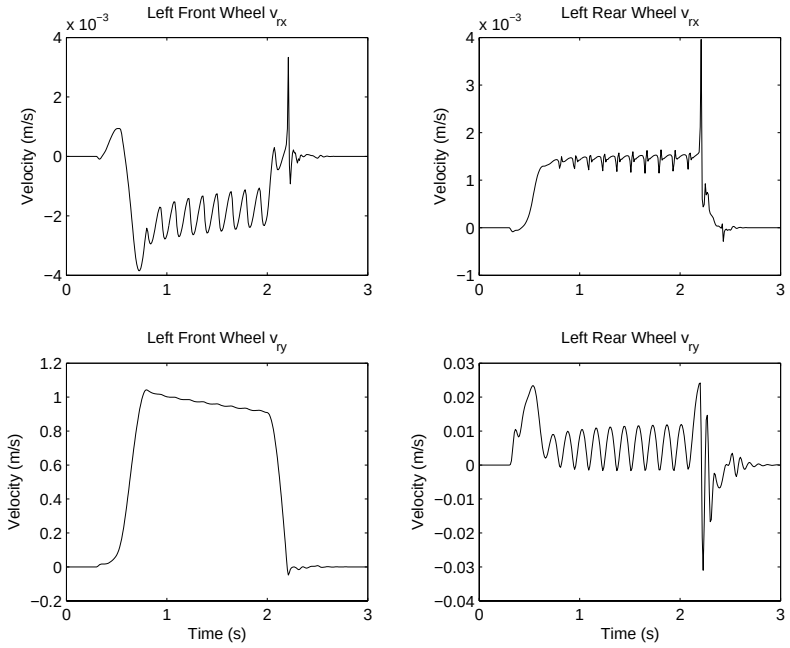


**Figure 18:** Wheel-road relative velocities during turn maneuver on normal road.

The fast friction dynamic that gives rise to the bristle oscillations has little observable impact on the slower vehicle body as seen in Figure 15 and some effect on the wheel dynamics. This is clearly shown in Figure 19 where the wheel speeds on the left and right sides of the vehicle diverge as the left wheels slow down and the right wheels speed up to traverse turns of differing radii, and some oscillation is apparent. The wheels are affected by the friction to a greater extent than the vehicle body because of their significantly lower mass and inertia.

While vehicle forces do not explicitly appear in the model, they may be computed from the state variables and plotted as well. Friction forces applied to the left wheels are shown in Figure 20. Here we see that the longitudinal forces are small since force is only required to slow down the wheels as the vehicle body slows, while lateral forces are high to achieve the lateral and angular acceleration necessary to turn the vehicle. A significant feature to note in the forces are the large transients that occur as the steer angle is changing. The wheels are able to instantaneously achieve much higher force than they are capable of achieving at steady state. This is a feature of the dynamic friction model and is not predicted by static

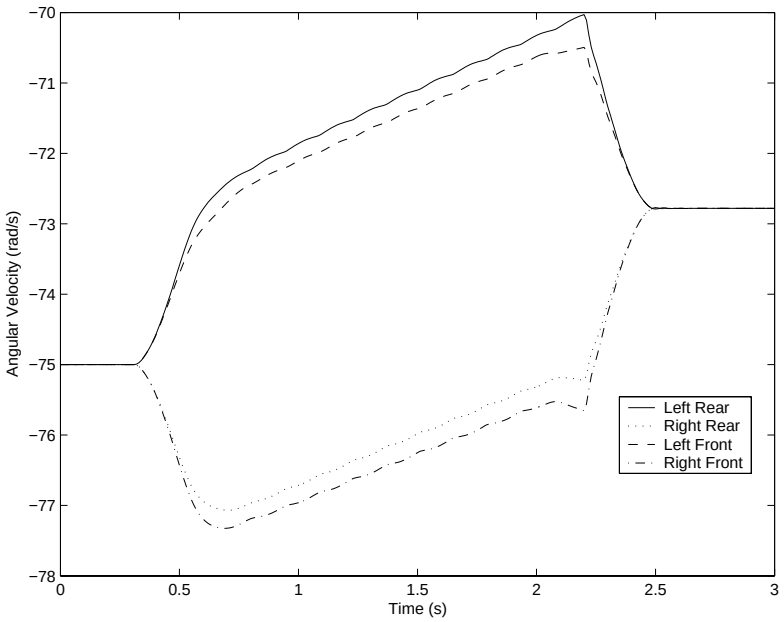


**Figure 19:** Wheelspeeds during turn maneuver on normal road.

force models such as Pacejka's Magic Formula [35].

The normal forces are shown in Figure 21 and begin higher for the rear wheels since the center of gravity is closer to the rear. Then, as the vehicle turns, the normal forces increase on the right side and decrease by the same amount on the left side as weight transfer occurs due to the centripetal acceleration of the turn.

We have thus far verified that the model behaves as we would expect for an automobile on a normal road with no torque input. The system is next simulated applying -50 Nm negative torque inputs to each wheel to accelerate the vehicle with the same steering input as was used for the no-torque scenario. Recall that as a result of our selected sign conventions, negative torque should produce forward vehicle motion. The resulting vehicle body velocities are shown in Figure 22 and we observe that the vehicle does, indeed, accelerate. Note, however, that in comparison to the case of no applied torque, the lateral and angular velocities of the vehicle are lower. The effect of these lower velocities is more apparent in Figure 23 which shows a comparison between the vehicle path that resulted from torque input and that which we saw previously in the case of no applied torque.

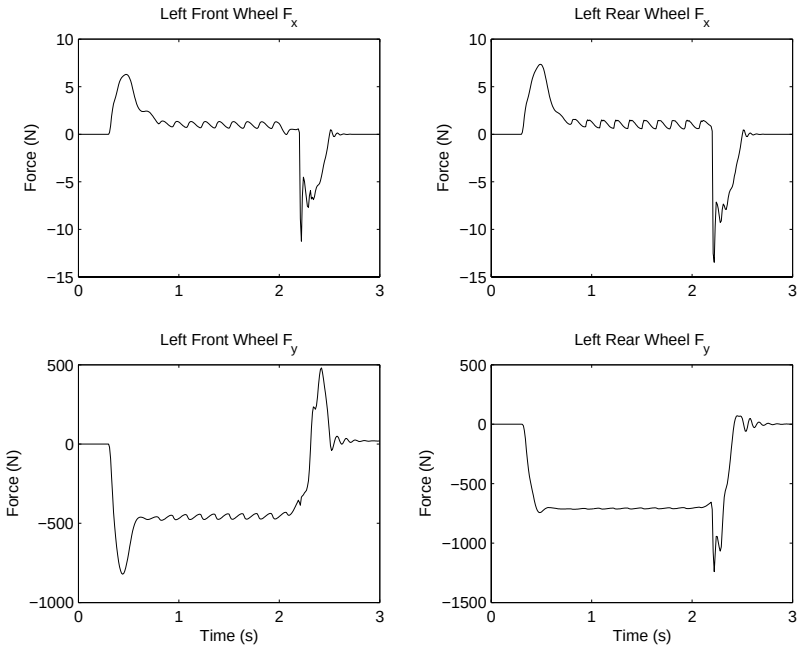


**Figure 20:** Forces on left wheels during turn maneuver on normal road.

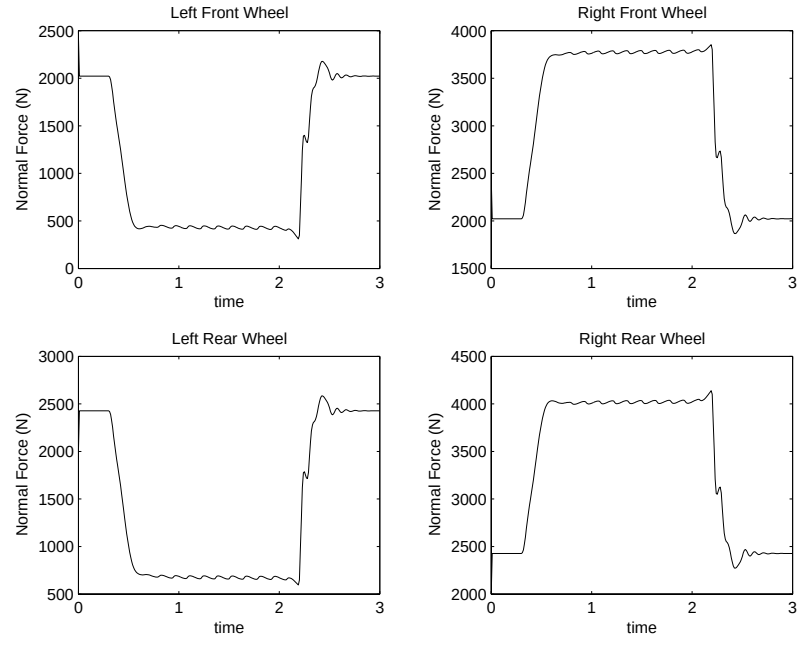


**Figure 21:** Normal forces during turn maneuver on normal road.

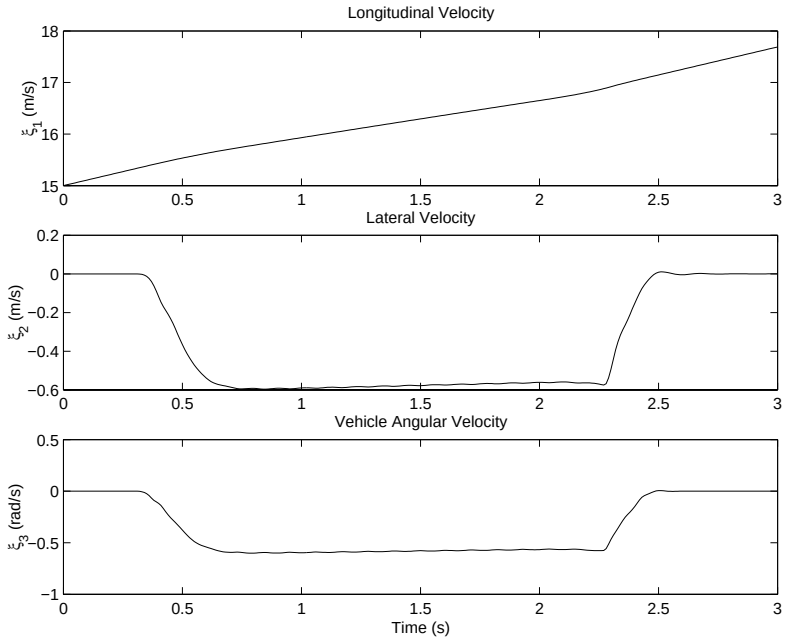


**Figure 22:** Vehicle body velocities during turn maneuver on normal road with -50 Nm torque input at each wheel.

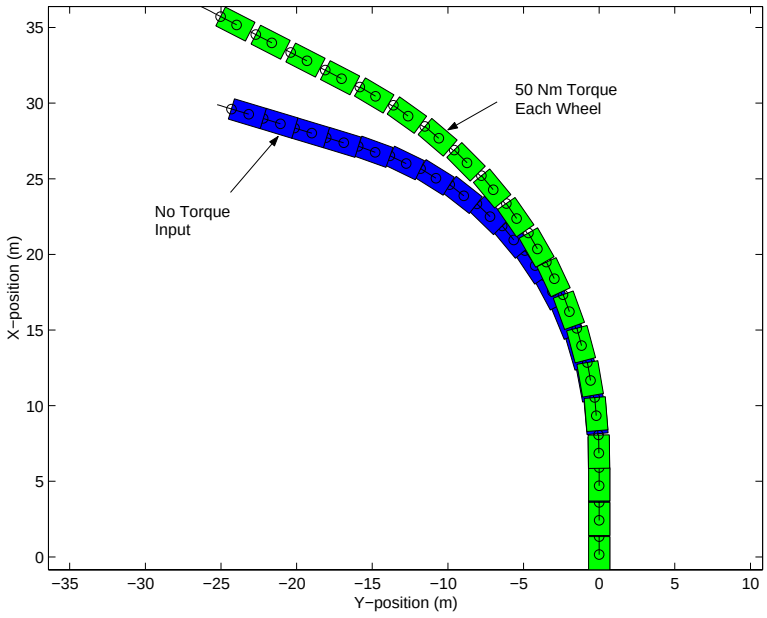


**Figure 23:** Vehicle path during turn maneuver on normal road with -50 Nm torque input at each wheel, compared to the case with no torque input.

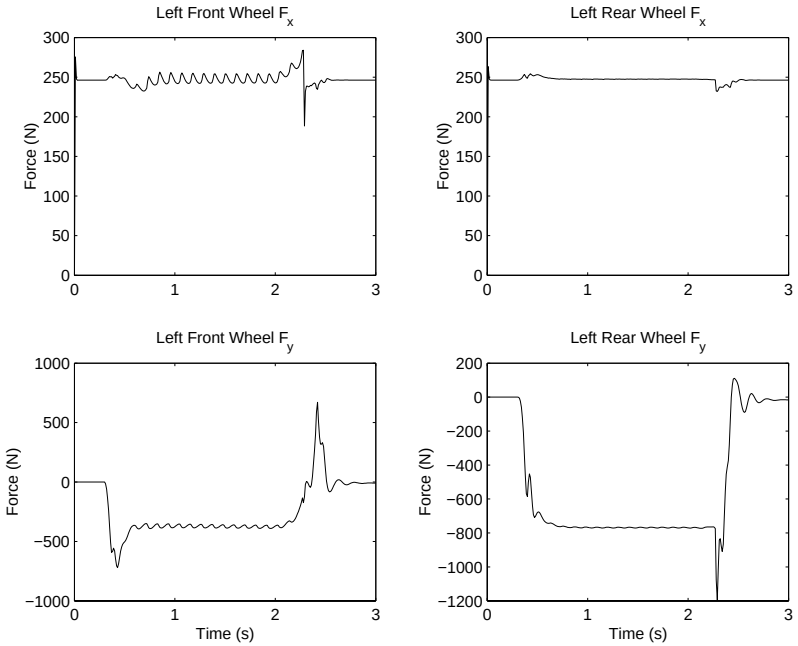


**Figure 24:** Friction forces during turn maneuver on normal road with -50 Nm torque input at each wheel.

When torque is applied, the vehicle turns less than it did previously. This result may be explained by examination of the friction forces, shown in Figure 24. The lateral force applied to the front wheel is lower than it was previously and the force is higher for the rear wheel. This produces less of a turning moment, causing the decrease in angular velocity. In addition, the overall lateral force is lower as well, and this leads to reduced lateral acceleration.

This force change is a result of the coupling of the $x$- and $y$-axis relative velocities in the friction model. Figure 25 shows that due to the torque input, the longitudinal relative velocity is much higher for the front wheel than it was previously, while the lateral velocity is only slightly increased. The much larger total relative velocity slows the bristle deflection by pushing the $\Gamma$ function closer to the dynamic coefficient of friction. This slowing, in turn, reduces the available force produced by bristle deflection rate, and the wheel is unable to produce sufficient lateral force to steer the vehicle as it did previously.

This effect of reduced lateral force in the presence of increased longitudinal force is well

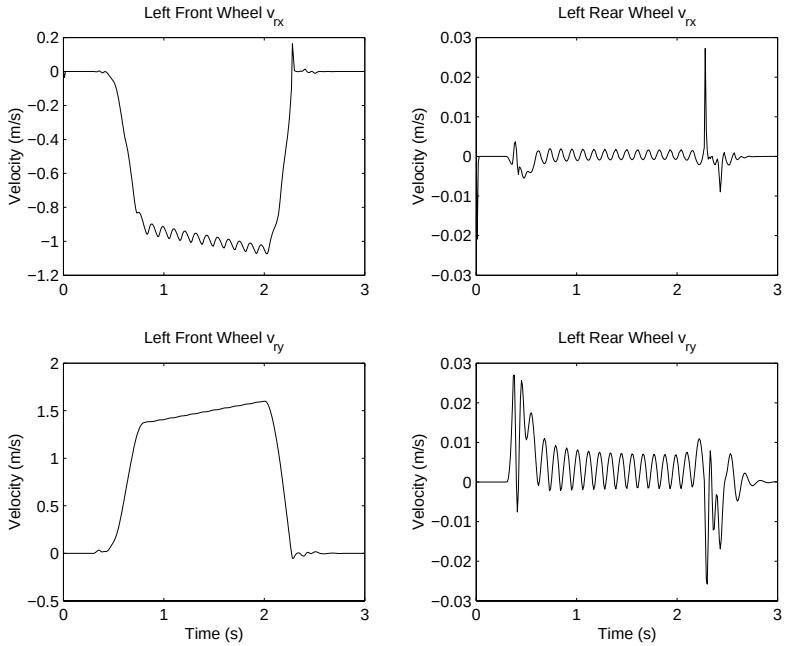


**Figure 25:** Wheel-road relative velocities during turn maneuver on normal road with -50 Nm torque input at each wheel.

recognized in the vehicle dynamics literature and is discussed in the context of "friction circles" that provide bounds to the total achievable force (e.g., [33, 19, 16]). The concept of such a discrete limiting bound, however, is only truly applicable to the steady-state friction force, since friction dynamics allow for the possibility of extremely high transient forces. The peak magnitude of the transient forces is influenced by a host of factors including vehicle inertia properties, friction parameters, and system inputs, including both steering and wheel torque. Thus, for transient forces, it is impossible to characterize such a bound.

We have now verified that the vehicle model may be successfully implemented in simulation. We devote the remainder of this chapter to exploring the slick road behavior of the vehicle model since this is the regime of operation in which we would most like to implement control.

### 4.2.2 Slick Road Vehicle Simulation

In order to simulate a slick road surface such as ice, we alter only the coefficients of friction. The dynamic coefficient of friction, $\mu_d$, is reduced to 0.1, and the static coefficient of friction,

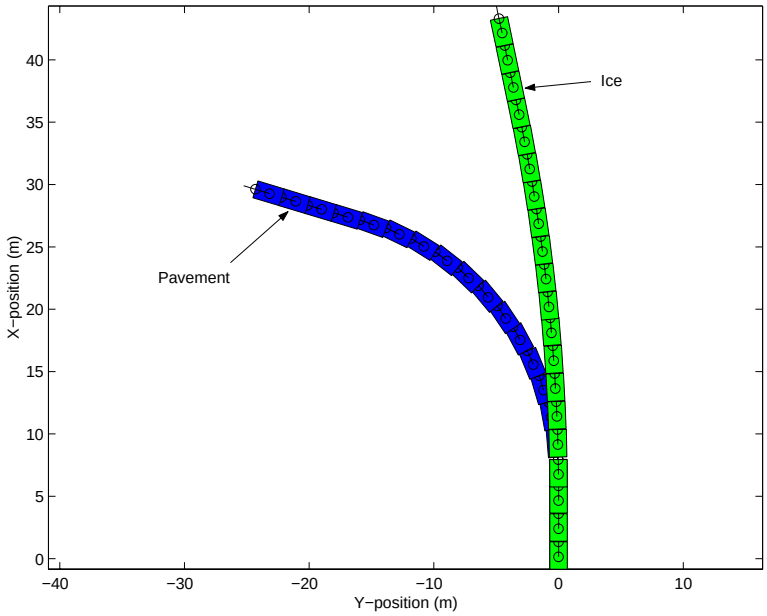


**Figure 26:** Comparison of the vehicle path on slick versus normal road with no torque input.

$\mu_s$, is reduced to 0.2. All other model parameters are maintained at their previous values as defined in Table 2, and we continue to use the steering input shown in Figure 14 so that we may compare vehicle performance to what was observed in the normal road case.

The simulation for the vehicle on a slippery road is now run with zero torque input and the resulting vehicle path is shown in Figure 26, overlaid on top of the normal road, no torque input path. The vehicle's yaw motion is considerably reduced during the interval with steering input, yet despite the lower response, the vehicle behaves in a stable fashion.

The slower vehicle response results from much lower bristle deflection rates, which consequently produce smaller bristle deflections as shown in Figure 27. These bristle deflections are an order of magnitude smaller than those occuring for the vehicle on the normal road, and produce much less force. With such a reduced ability to generate lateral bristle deflections, the vehicle achieves much lower turning velocities.

Consider, now, application of wheel torque to only the front wheels of the vehicle as for a front-wheel-drive automobile. We desire to apply the same total driving torque as in the normal road case, and we thus apply constant -100 Nm of torque to each front wheel. This

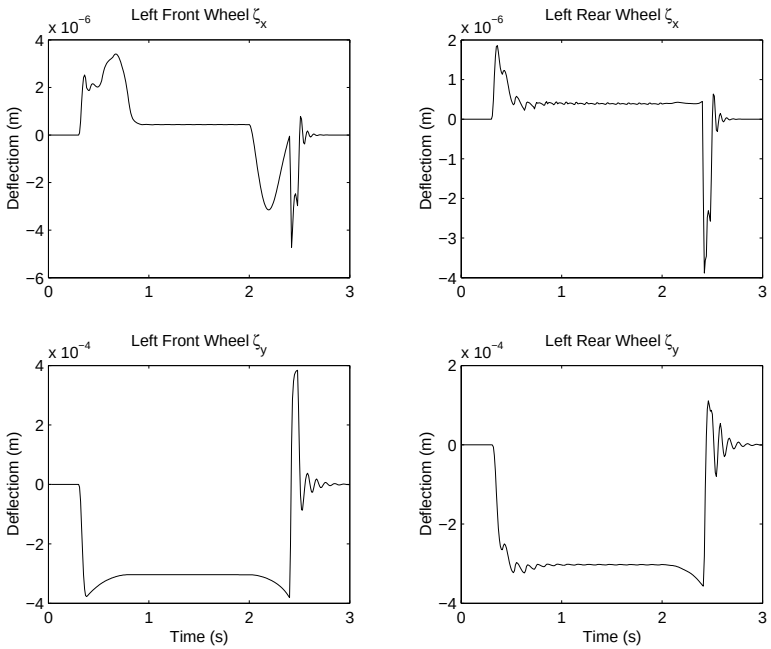


**Figure 27:** Bristle deflection for the left wheels of the vehicle on a slick surface with no torque input.

input results in even greater reductions in the ability of the vehicle to turn on the slick road, as shown in Figure 28. As in the case of normal road driving, torque inputs increase the relative velocities at the wheel-road interface, and produce lower lateral wheel force while increasing the longitudinal wheel force.

This reduction in lateral force due to the application of wheel torque proves to be disastrous in the case of torque application to only the rear wheels of the vehicle. In this case, the front wheel lateral force becomes much higher than the rear wheel lateral force, inducing a very high yaw moment about the vehicle center of gravity, causing the vehicle to spin out of control. This behavior is demonstrated in Figure 29 and is a clear demonstration of the most undesirable type of vehicle response.

The rear-wheel-drive situation serves to illustrate the very important point that wheel torque has a significant impact on the lateral response of the vehicle. This has two important implications for vehicle control. First, control of lateral and angular velocity modes by use of wheel torque alone is feasible. Second, successful control by means of wheel torque requires avoidance of inputs that produce the observed spin behavior.

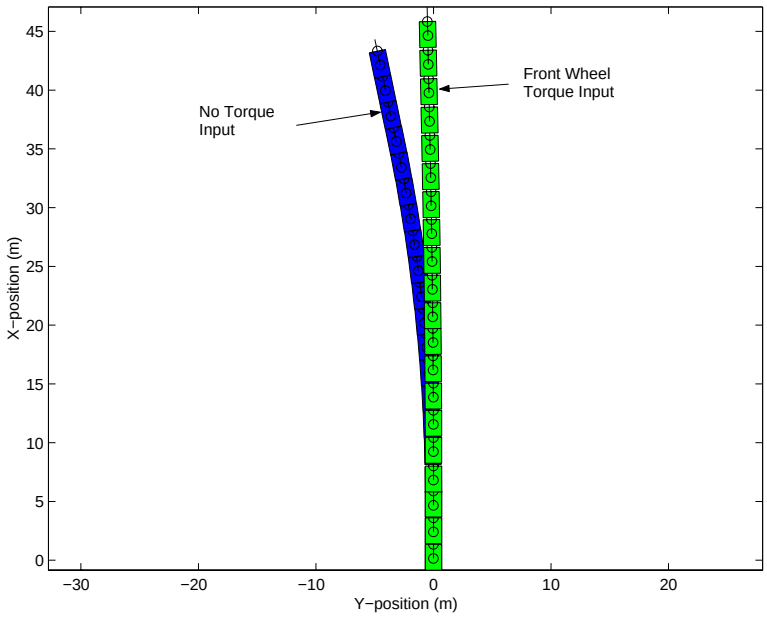


**Figure 28:** Comparison of the vehicle path on slick road with -100 Nm applied to front wheels versus no torque input.

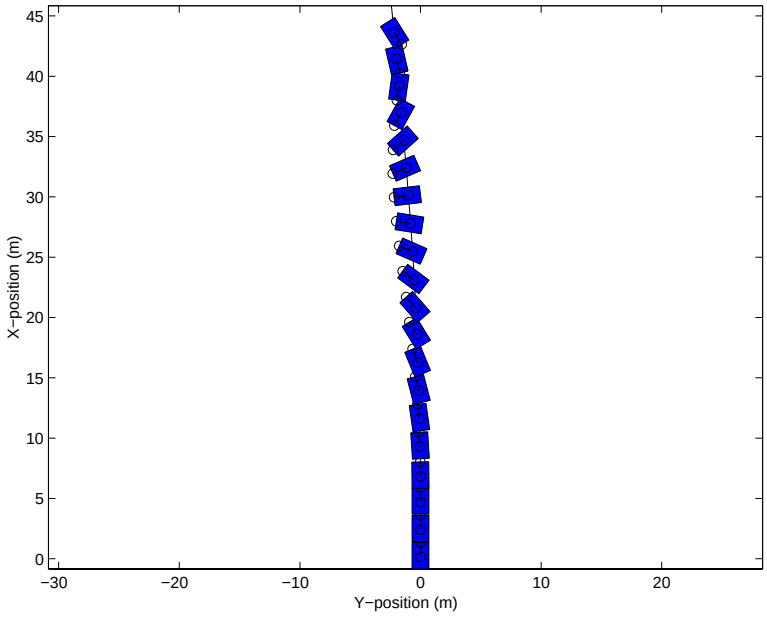


**Figure 29:** Vehicle spin resulting from -100 Nm torque input to rear wheels.

# CHAPTER V

# VEHICLE CONTROL

The model presented in (73)-(75) now puts us in a position to consider control of an automobile. As was discussed in Chapter 1, we desire a controller that assists a driver rather than one that makes the vehicle fully autonomous. We must therefore begin the development of control by considering strategies for achieving this goal.

## *5.1 Control Strategy*

In order for the human vehicle operator, the driver, to command vehicle motion, we suggest a two-fold scheme for segmenting vehicle control authority. First, the driver will always maintain direct control over the steering of the vehicle. The automatic controller is only able to function by adjusting wheel torque. This creates an effective segmentation of human versus automatic control capability. Second, we require that the vehicle controller respond to real-time driver inputs and regulate undesirable vehicle behavior. This may be accomplished through suitable specification of desired vehicle trajectories as a function of driver input variables such as steer angle, accelerator, and braking, and by appropriate choice of outputs.

We consider, also, that motion of the vehicle is to be controlled in a two-dimensional plane. Such motion is fully described by three variables: longitudinal, lateral, and angular velocity. Combinations of these velocities may thus be used as output variables, depending on specific vehicle motion control objectives. If we assume that wheel torque at all four wheels may be independently specified, then our control architecture has four inputs, and up to three outputs.

For the purposes of this control development, we must make some simplifying assumptions. For our design model, we shall assume constant $\sigma$ parameters for the friction. We will therefore select each $\sigma$ as the average value of the corresponding simulation model $\sigma$

function, and will be able to explore the effect of this simplification after control implementation. We also assume that we have ideal torque sources at each wheel, which may provide positive and negative torque, and be adjusted arbitrarily fast. Such an assumption would be valid for control by means of independent electric motors at each wheel whose response is much faster than the dynamics of the vehicle. We will show later how such an assumption might be dispensed with, to some extent, to effectively consider mechanical torque sources.

It is also necessary to consider the static and dynamic coefficients of friction between the wheels and road to be constant, known parameters. In general, these parameters are actually slowly varying and may be determined by use of estimation techniques. Similarly, we consider all vehicle model states to be fully measureable, including friction model states. This is not typically the case in production automobiles, however, we suggest that this deficiency may be dealt with by use of a dynamic state observer. This approach will be left for consideration in future work. The control formulation that shall be presented is, then, in some sense ideal, and is an indication of the best possible control that may be accomplished.

This control architecture is shown in Figure 30 as a block diagram. The driver generates the time-varying exogenous steering signal which is fed into the controller. Measurements of the vehicle body and wheel velocities, and friction bristle deflections are made by sensors and these also are input to the controller. The controller has access to a pre-defined parameter list, including system masses and inertias, bristle stiffnesses, and coefficients of friction. Finally, the controller outputs the computed wheel torque, which passes through a limiting device and is then applied to the wheels.

The control technique that we shall employ is input-output linearization. This technique requires that we first determine the relative degree of the system, which indicates the number of times that the system output must be differentiated before appearance of the control inputs [25, 26]. Since control outputs will always be a combination of the vehicle body velocities, our relative degree analysis will begin by considering the derivatives of these velocities.

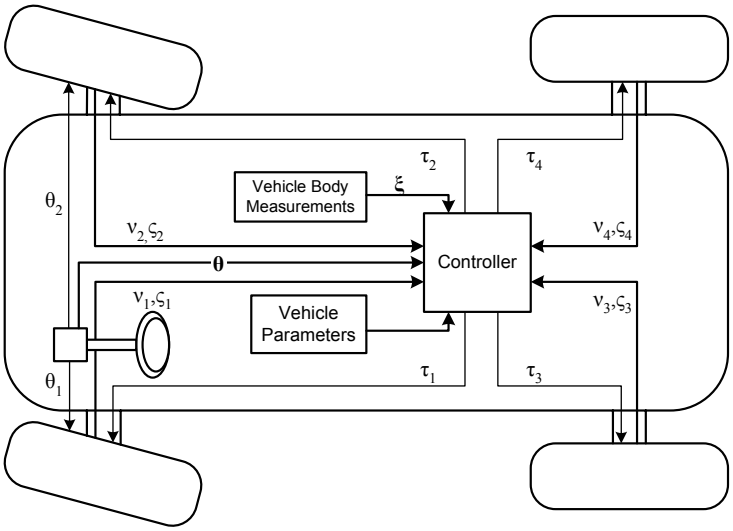


**Figure 30:** Control architecture diagram.

## *5.2 Relative Degree*

The state vector partition, $\boldsymbol{\xi}$, of Chapters 2 and 4 consists of the three velocity output variables of interest. Equation (73) therefore gives the first derivative of the output. The torque input vector $\boldsymbol{\tau}$ does not appear in this equation, and we must continue to differentiate $\boldsymbol{\xi}$ to discover if our system possesses relative degree.

### 5.2.1 Vehicle Body Jerk

The derivative of (73) yields vehicle body jerk equations and is found by term-by-term differentiation as

$$\boldsymbol{M}_1\ddot{\boldsymbol{\xi}} = \dot{\boldsymbol{\eta}} + \dot{\boldsymbol{A}}\boldsymbol{P}^{-1}\boldsymbol{c} + \boldsymbol{A}\frac{d(\boldsymbol{P}^{-1}\boldsymbol{c})}{dt} \tag{78}$$

where functional dependencies have been dropped on the right-hand side for notational convenience. We now consider the individual derivatives on the right-hand side of (78). The first two are simply

$$\dot{\eta}(\boldsymbol{\xi}) = m_v[\dot{\omega}_v v_y + \omega_v \dot{v}_y, -\dot{\omega}_v v_x - \omega_v \dot{v}_x, 0]^T \tag{79}$$

$$\dot{\boldsymbol{A}} = \dot{\boldsymbol{A}}_x\boldsymbol{\mu}_x + \dot{\boldsymbol{A}}_y\boldsymbol{\mu}_y + \boldsymbol{A}_x\dot{\boldsymbol{\mu}}_x + \boldsymbol{A}_y\dot{\boldsymbol{\mu}}_y \tag{80}$$

Despite the appearance of the matrix inverse, the derivative of the third term in (78) is also easily computable. The term is the normal force as defined in Chapter 2 and may be

differentiated as follows:

$$\begin{aligned} \boldsymbol{N} &= \boldsymbol{P}^{-1}\boldsymbol{c} \\ \boldsymbol{P}\boldsymbol{N} &= \boldsymbol{c} \\ \dot{\boldsymbol{P}}\boldsymbol{N} + \boldsymbol{P}\dot{\boldsymbol{N}} &= \dot{\boldsymbol{c}} \\ \dot{\boldsymbol{N}} &= \boldsymbol{P}^{-1}\left(\dot{\boldsymbol{c}} - \dot{\boldsymbol{P}}\boldsymbol{N}\right) \end{aligned}$$

Since $\boldsymbol{c}$ is constant, we have

$$\frac{d(\boldsymbol{P}^{-1}\boldsymbol{c})}{dt} = -\boldsymbol{P}^{-1}\dot{\boldsymbol{P}}\boldsymbol{P}^{-1}\boldsymbol{c} \tag{81}$$

and note that

$$\dot{\boldsymbol{P}} = -\dot{\boldsymbol{P}}_x\boldsymbol{\mu}_x - \dot{\boldsymbol{P}}_y\boldsymbol{\mu}_y - \boldsymbol{P}_x\dot{\boldsymbol{\mu}}_x - \boldsymbol{P}_y\dot{\boldsymbol{\mu}}_y \tag{82}$$

Use of these derivatives in (78) now yields the simplified matrix equation

$$\boldsymbol{M}_1\ddot{\boldsymbol{\xi}} = \dot{\boldsymbol{\eta}} + \left(\dot{\boldsymbol{A}} - \boldsymbol{A}\boldsymbol{P}^{-1}\dot{\boldsymbol{P}}\right)\boldsymbol{P}^{-1}\boldsymbol{c} \tag{83}$$

however, the control inputs do not yet appear explicitly in this expression. If these inputs are to appear, they must result from the derivatives of the $\boldsymbol{A}$ and $\boldsymbol{P}$ matrices. Further note from (74) of the previous chapter that the torque vector appears only as a result of wheel angular acceleration. Thus, in order for torque to appear in the vehicle body velocity derivatives, we must have derivatives of wheel angular velocity. Since these velocities appear in the vehicle body dynamical equations only in the friction matrices, torque will be manifested in (83) only as a result of differentiation of these matrices. Recognizing that the term inside the parentheses of (83) consists of combinations of $\boldsymbol{\mu}_x$ and $\boldsymbol{\mu}_y$ and their derivatives, we may expose these dependencies by rewriting this term as

$$\dot{\boldsymbol{A}} - \boldsymbol{A}\boldsymbol{P}^{-1}\dot{\boldsymbol{P}} = \boldsymbol{Q}_x\boldsymbol{\mu}_x + \boldsymbol{Q}_y\boldsymbol{\mu}_y + \boldsymbol{R}_x\dot{\boldsymbol{\mu}}_x + \boldsymbol{R}_y\dot{\boldsymbol{\mu}}_y \tag{84}$$

where

$$\boldsymbol{Q}_x = \dot{\boldsymbol{A}}_x + \boldsymbol{A}\boldsymbol{P}^{-1}\dot{\boldsymbol{P}}_x \tag{85}$$

$$\boldsymbol{Q}_y = \dot{\boldsymbol{A}}_y + \boldsymbol{A}\boldsymbol{P}^{-1}\dot{\boldsymbol{P}}_y \tag{86}$$

$$\boldsymbol{R}_x = \boldsymbol{A}_x + \boldsymbol{A}\boldsymbol{P}^{-1}\boldsymbol{P}_x \tag{87}$$

$$\boldsymbol{R}_y = \boldsymbol{A}_y + \boldsymbol{A}\boldsymbol{P}^{-1}\boldsymbol{P}_y \tag{88}$$

This allows us to separate terms containing derivatives of the friction matrices that we expect to be functions of wheel torque and those that are functions only of the vehicle system state variables. Utilizing this definition, (83) becomes

$$\boldsymbol{M}_1\ddot{\boldsymbol{\xi}} = \dot{\boldsymbol{\eta}} + \boldsymbol{Q}\boldsymbol{P}^{-1}\boldsymbol{c} + \left(\boldsymbol{R}_x\dot{\boldsymbol{\mu}}_x + \boldsymbol{R}_y\dot{\boldsymbol{\mu}}_y\right)\boldsymbol{P}^{-1}\boldsymbol{c} \tag{89}$$

with

$$\boldsymbol{Q} = \boldsymbol{Q}_x\boldsymbol{\mu}_x + \boldsymbol{Q}_y\boldsymbol{\mu}_y \tag{90}$$

Note that the derivatives in $\boldsymbol{Q}_x$ and $\boldsymbol{Q}_y$ are obtained by time differentiation of the appropriate $\boldsymbol{A}$ and $\boldsymbol{P}$ matrices of Chapter 2. These derivatives are simply

$$\dot{\boldsymbol{P}}_x = \boldsymbol{q}_{xx}\dot{\boldsymbol{\theta}}^T\frac{\partial\boldsymbol{\lambda}_c(\boldsymbol{\theta})}{\partial\boldsymbol{\theta}} + \boldsymbol{q}_{yx}\dot{\boldsymbol{\theta}}^T\frac{\partial\boldsymbol{\lambda}_s(\boldsymbol{\theta})}{\partial\boldsymbol{\theta}} \tag{91}$$

$$\dot{\boldsymbol{P}}_y = \boldsymbol{q}_{xy}\dot{\boldsymbol{\theta}}^T\frac{\partial\boldsymbol{\lambda}_s(\boldsymbol{\theta})}{\partial\boldsymbol{\theta}} + \boldsymbol{q}_{yy}\dot{\boldsymbol{\theta}}^T\frac{\partial\boldsymbol{\lambda}_c(\boldsymbol{\theta})}{\partial\boldsymbol{\theta}} \tag{92}$$

where the $\boldsymbol{q}$ vectors consist of the ordered constants of (19)-(22) and

$$\dot{\boldsymbol{A}}_x = \begin{bmatrix} \dot{\boldsymbol{\theta}}^T\frac{\partial\boldsymbol{\lambda}_c(\boldsymbol{\theta})}{\partial\boldsymbol{\theta}} \\ -\dot{\boldsymbol{\theta}}^T\frac{\partial\boldsymbol{\lambda}_s(\boldsymbol{\theta})}{\partial\boldsymbol{\theta}} \\ \dot{\boldsymbol{\theta}}^T\left(\frac{\partial\boldsymbol{\lambda}_s(\boldsymbol{\theta})}{\partial\boldsymbol{\theta}}\boldsymbol{X} - \frac{\partial\boldsymbol{\lambda}_c(\boldsymbol{\theta})}{\partial\boldsymbol{\theta}}\boldsymbol{Y}\right) \end{bmatrix} \tag{93}$$

$$\dot{\boldsymbol{A}}_y = \begin{bmatrix} \dot{\boldsymbol{\theta}}^T\frac{\partial\boldsymbol{\lambda}_s(\boldsymbol{\theta})}{\partial\boldsymbol{\theta}} \\ \dot{\boldsymbol{\theta}}^T\frac{\partial\boldsymbol{\lambda}_c(\boldsymbol{\theta})}{\partial\boldsymbol{\theta}} \\ \dot{\boldsymbol{\theta}}^T\left(\frac{\partial\boldsymbol{\lambda}_c(\boldsymbol{\theta})}{\partial\boldsymbol{\theta}}\boldsymbol{X} + \frac{\partial\boldsymbol{\lambda}_s(\boldsymbol{\theta})}{\partial\boldsymbol{\theta}}\boldsymbol{Y}\right) \end{bmatrix} \tag{94}$$

Now, recall that $\boldsymbol{\mu}_x$ and $\boldsymbol{\mu}_y$ are diagonal matrices and thus their derivatives are diagonal as well, so that we may now express (89) as

$$\boldsymbol{M}_1\ddot{\boldsymbol{\xi}} = \dot{\boldsymbol{\eta}} + \boldsymbol{Q}\boldsymbol{P}^{-1}\boldsymbol{c} + \boldsymbol{R}_x\mathrm{diag}(\boldsymbol{P}^{-1}\boldsymbol{c})\dot{\boldsymbol{\mu}}_x^* + \boldsymbol{R}_y\mathrm{diag}(\boldsymbol{P}^{-1}\boldsymbol{c})\dot{\boldsymbol{\mu}}_y^* \tag{95}$$

where $\boldsymbol{\mu}_x^*$ and $\boldsymbol{\mu}_y^*$ are the diagonals of the respective friction matrices and are thus vectors of friction functions for the $x$- and $y$-components for each wheel. Observe now that the first two terms of this equation are functions only of state variables while the last two terms are functions of state variables and possibly wheel torque.

We postulate that the derivatives of the friction function vectors are of the form

$$\dot{\boldsymbol{\mu}}_x^* = \boldsymbol{\alpha}_x(\boldsymbol{\xi},\boldsymbol{\nu},\boldsymbol{\zeta}) + \boldsymbol{\beta}_x(\boldsymbol{\xi},\boldsymbol{\nu},\boldsymbol{\zeta})\boldsymbol{\tau} \tag{96}$$

$$\dot{\boldsymbol{\mu}}_y^* = \boldsymbol{\alpha}_y(\boldsymbol{\xi},\boldsymbol{\nu},\boldsymbol{\zeta}) + \boldsymbol{\beta}_y(\boldsymbol{\xi},\boldsymbol{\nu},\boldsymbol{\zeta})\boldsymbol{\tau} \tag{97}$$

where $\boldsymbol{\alpha}_x$ and $\boldsymbol{\alpha}_y$ are $4 \times 1$ vectors and $\boldsymbol{\beta}_x$ and $\boldsymbol{\beta}_y$ are $4 \times 4$ matrices of state variables. We will show later that this is, indeed, the case for a number of forms of the friction functions. For the time being, we may use (96)-(97) to write (95) in terms of the torque vector as

$$\boldsymbol{M}_1\ddot{\boldsymbol{\xi}} = \dot{\boldsymbol{\eta}} + \boldsymbol{Q}\boldsymbol{P}^{-1}\boldsymbol{c} + \boldsymbol{R}(\boldsymbol{\xi},\boldsymbol{\nu},\boldsymbol{\zeta}) + \boldsymbol{G}(\boldsymbol{\xi},\boldsymbol{\nu},\boldsymbol{\zeta})\boldsymbol{\tau} \tag{98}$$

where

$$\boldsymbol{R}(\boldsymbol{\xi},\boldsymbol{\nu},\boldsymbol{\zeta}) = \boldsymbol{R}_x\mathrm{diag}(\boldsymbol{P}^{-1}\boldsymbol{c})\boldsymbol{\alpha}_x(\boldsymbol{\xi},\boldsymbol{\nu},\boldsymbol{\zeta}) + \boldsymbol{R}_y\mathrm{diag}(\boldsymbol{P}^{-1}\boldsymbol{c})\boldsymbol{\alpha}_y(\boldsymbol{\xi},\boldsymbol{\nu},\boldsymbol{\zeta}) \tag{99}$$

$$\boldsymbol{G}(\boldsymbol{\xi},\boldsymbol{\nu},\boldsymbol{\zeta}) = \boldsymbol{R}_x\mathrm{diag}(\boldsymbol{P}^{-1}\boldsymbol{c})\boldsymbol{\beta}_x(\boldsymbol{\xi},\boldsymbol{\nu},\boldsymbol{\zeta}) + \boldsymbol{R}_y\mathrm{diag}(\boldsymbol{P}^{-1}\boldsymbol{c})\boldsymbol{\beta}_y(\boldsymbol{\xi},\boldsymbol{\nu},\boldsymbol{\zeta}) \tag{100}$$

Finally, we may express this equation for vehicle body jerk in the canonical form for Input-Output Linearization with output derivatives equal to a vector function of state variables plus a decoupling matrix multiplied by an input vector as

$$\boldsymbol{M}_1\ddot{\boldsymbol{\xi}} = \boldsymbol{f}(\boldsymbol{\xi},\boldsymbol{\nu},\boldsymbol{\zeta}) + \boldsymbol{G}(\boldsymbol{\xi},\boldsymbol{\nu},\boldsymbol{\zeta})\boldsymbol{\tau} \tag{101}$$

where

$$\boldsymbol{f}(\boldsymbol{\xi},\boldsymbol{\nu},\boldsymbol{\zeta}) = \dot{\boldsymbol{\eta}} + \boldsymbol{Q}\boldsymbol{P}^{-1}\boldsymbol{c} + \boldsymbol{R}(\boldsymbol{\xi},\boldsymbol{\nu},\boldsymbol{\zeta}) \tag{102}$$

Thus, for any vehicle system with outputs defined as some function of the vehicle body velocities such that

$$\boldsymbol{y} = \boldsymbol{h}(\boldsymbol{\xi}) \tag{103}$$

where $\boldsymbol{h}(\boldsymbol{\xi})$ may be linear or nonlinear, the system posseses relative degree in the vehicle body jerk as long as the matrix

$$\frac{\partial \boldsymbol{h}(\boldsymbol{\xi})}{\partial \boldsymbol{\xi}}\boldsymbol{M}_1^{-1}\boldsymbol{G} \tag{104}$$

exists and has full row rank. Since $\boldsymbol{h}(\boldsymbol{\xi})$ may always be selected such that its Jacobian matrix exists and has full rank, and the inverse of the diagonal mass matrix $\boldsymbol{M}_1$ always

possesses full rank, the existence and rank requirements are transferred to the decoupling matrix, $\boldsymbol{G}$. Critical to the existence and rank properties of $\boldsymbol{G}$ are the matrices $\boldsymbol{\beta}_x$ and $\boldsymbol{\beta}_y$, and we must now examine the friction function derivatives to determine the exact form of (96) and (97).

### 5.2.2 Friction Function Derivatives

We choose to consider two friction functions for our relative degree analysis. These are the dynamic LuGre friction function of (44) and the steady-state LuGre friction function of (50). Since the steady-state LuGre model matches Pacejka's Magic Formula model well as demonstrated in Chapter 3, analysis of the steady-state LuGre friction function shall suffice for understanding the relative degree properties of a vehicle model utilizing the Magic Formula.

Let us begin the analysis with the steady-state friction function, which we repeat here for convenience as

$$\boldsymbol{\mu} = -\Gamma(\boldsymbol{v}_r)\frac{\boldsymbol{v}_r}{\|\boldsymbol{v}_r\|} \tag{105}$$

This function is troublesome due to the fact that when $\boldsymbol{v}_r = 0$, it is not well defined as a result of the vector norm that appears in the denominator. We therefore choose to approximate this function as

$$\boldsymbol{\mu} = -\Gamma(\boldsymbol{v}_r)\begin{bmatrix} -\frac{v_{rx}^3}{2\rho^3} + \frac{3v_{rx}}{2\rho} - \frac{v_{rx}v_{ry}^2}{2\rho^3} \\ -\frac{v_{ry}^3}{2\rho^3} + \frac{3v_{ry}}{2\rho} - \frac{v_{ry}v_{rx}^2}{2\rho^3} \end{bmatrix} \tag{106}$$

for $\|\boldsymbol{v}_r\| \leq \rho$ with $\rho$ a small positive constant. This function is well defined when $\|\boldsymbol{v}_r\|$ is equal to zero and using this approximation and (105) when $\|\boldsymbol{v}_r\| > \rho$, we have a continuous and well-defined $\boldsymbol{\mu}$ everywhere.

This approximation may be better understood by examining the one-dimensional case. In one dimension, the steady state friction function is the scalar equation

$$\mu = -\Gamma(v_r)\text{sgn}(v_r) \tag{107}$$

The signum function is not well defined at zero and we may approximate this discontinuous

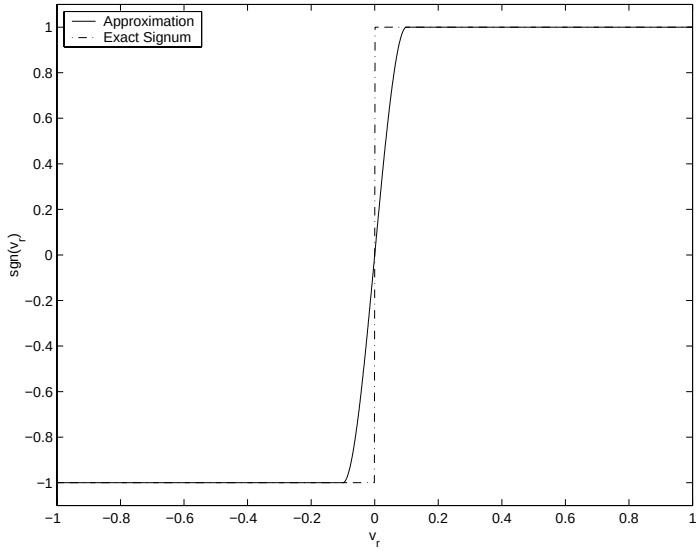


**Figure 31:** Continuous approximation to the signum function with a cubic spline.

function with a continuous cubic polynomial over the range $-\rho \leq v_r \leq \rho$ as

$$\mu = -\Gamma(v_r)\left(-\frac{v_r^3}{2\rho^3} + \frac{3v_r}{2\rho}\right) \tag{108}$$

This approximation is chosen such that $\mu$ is continuous and has a continuous first derivative at $\pm\rho$ as shown in Figure 31.

Notice that the signum function is simply the derivative of the absolute value. This suggests that in two dimensions, $\boldsymbol{v}_r/\|\boldsymbol{v}_r\|$ as in (105) is the gradient of a cone as shown in Figure 32 and that the problematic point is the tip of the cone where the gradient is not defined. We therefore replace the tip of the cone with the quartic surface defined by

$$\|\boldsymbol{v}_r\| \approx -\frac{v_{rx}^4}{8\rho^3} - \frac{v_{ry}^4}{8\rho^3} + \frac{3v_{rx}^2}{4\rho} + \frac{3v_{ry}^2}{4\rho} - \frac{v_{ry}^2 v_{rx}^2}{4\rho^3} + \frac{3\rho}{8} \tag{109}$$

as shown in the figure, for $\|\boldsymbol{v}_r\| \leq \rho$, resulting in the gradients used in (106).

We now rewrite the friction function of (105) in terms of the gradient of the relative velocity norm as

$$\boldsymbol{\mu} = -\Gamma(\boldsymbol{v}_r)\frac{\partial\|\boldsymbol{v}_r\|}{\partial\boldsymbol{v}_r} \tag{110}$$

and proceed to differentiate the friction function to determine relative degree. The derivative

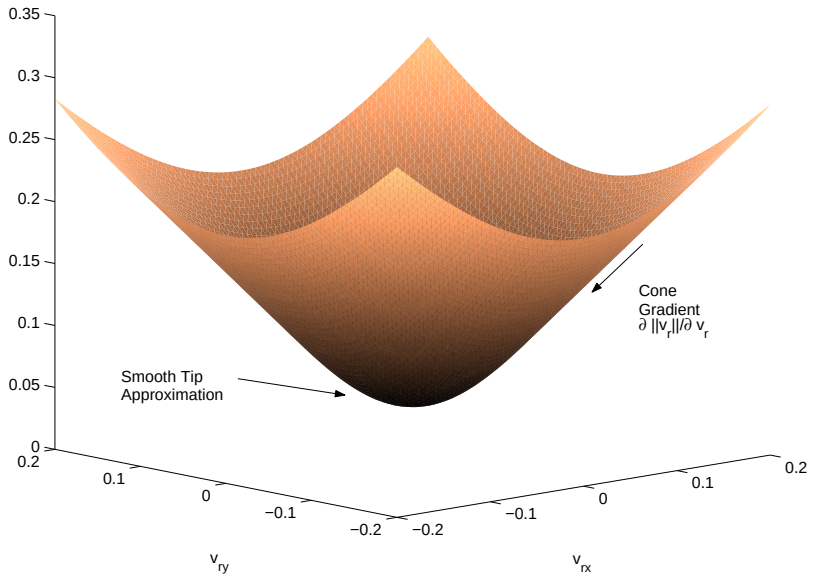


**Figure 32:** Relative velocity cone and cone tip approximation.

is

$$\dot{\boldsymbol{\mu}} = -\frac{1}{\|\boldsymbol{v}_r\|}\left[\left(\|\boldsymbol{v}_r\|\frac{\partial\Gamma(\boldsymbol{v}_r)}{\partial\|\boldsymbol{v}_r\|} - \Gamma(\boldsymbol{v}_r)\right)\frac{\partial\|\boldsymbol{v}_r\|}{\partial\boldsymbol{v}_r}\left(\frac{\partial\|\boldsymbol{v}_r\|}{\partial\boldsymbol{v}_r}\right)^T + \Gamma(\boldsymbol{v}_r)\right]\dot{\boldsymbol{v}}_r \tag{111}$$

and the derivative of the $\Gamma$ function is[1]

$$\frac{\partial\Gamma(\boldsymbol{v}_r)}{\partial\|\boldsymbol{v}_r\|} = -\alpha(\mu_s - \mu_d)\frac{\|\boldsymbol{v}_r\|^{\alpha-1}}{v_s^{\alpha}}e^{-\|\boldsymbol{v}_r/v_s\|^{\alpha}} \tag{112}$$

Notice that at zero relative velocity, the exact derivative in (111) is undefined, but use of the approximate gradient of the relative velocity norm for $\|\boldsymbol{v}_r\| < \rho$ gives rise to a well-defined limit of zero as $\|\boldsymbol{v}_r\|$ approaches zero. This result indicates a loss of relative degree for the overall system when the relative velocities of all wheel-road contact points are identically zero. Note, also, that should our system's friction possess non-zero $\sigma_2$ the result would be the addition of a $\sigma_2\dot{\boldsymbol{v}}_r$ term to (111) which would preserve relative degree. The implication is that for the case of dry-road contact, with no occurrence of slip, a controller designed using input-output linearization and a steady-state friction model would be unable

[1]The reader must be cautioned that the $\alpha$ parameter in the $\Gamma$ function has no relation to the $\boldsymbol{\alpha}_x$ and $\boldsymbol{\alpha}_y$ vectors of (96) and (97) other than that resulting from the appearance of $\Gamma$ or its derivative in these vectors.

to influence the vehicle jerk. Such a singularity in the relative degree might be avoided by use of the dynamic friction function instead.

The dynamic friction function is repeated here as

$$\boldsymbol{\mu} = \sigma_0 \boldsymbol{\zeta} + \sigma_1 \dot{\boldsymbol{\zeta}} + \sigma_2 \boldsymbol{v}_r \tag{113}$$

The dynamical friction equation of (41) allows us to express the friction function in terms of only state variables, eliminating the bristle deflection rates, and this becomes

$$\boldsymbol{\mu} = \sigma_0 \left(1 - \frac{\sigma_1 \|\boldsymbol{v}_r\|}{\Gamma(\boldsymbol{v}_r)}\right) \boldsymbol{\zeta} + (\sigma_2 - \sigma_1)\boldsymbol{v}_r \tag{114}$$

Now, differentiating this friction function, we have

$$\dot{\boldsymbol{\mu}} = \sigma_0 \left(1 - \frac{\sigma_1 \|\boldsymbol{v}_r\|}{\Gamma(\boldsymbol{v}_r)}\right) \dot{\boldsymbol{\zeta}} - \frac{\sigma_0 \sigma_1}{\Gamma(\boldsymbol{v}_r)} \left(1 - \frac{\|\boldsymbol{v}_r\|}{\Gamma(\boldsymbol{v}_r)} \frac{\partial \Gamma(\boldsymbol{v}_r)}{\partial \|\boldsymbol{v}_r\|}\right) \boldsymbol{\zeta} \left(\frac{\partial \|\boldsymbol{v}_r\|}{\partial \boldsymbol{v}_r}\right)^T \dot{\boldsymbol{v}}_r + (\sigma_2 - \sigma_1)\dot{\boldsymbol{v}}_r \tag{115}$$

and, once again, the gradient of the relative velocity norm is not well defined when the relative velocity goes to zero. Employing the polynomial gradient estimate in a neighborhood of zero relative velocity, the friction function derivative is well defined and the possibility for relative degree still exists since this function is not identically zero in the presence of zero relative velocity.

Thus, the dynamic friction model is immediately superior to the steady-state model in this sense. However, this superiority is at the expense of requiring knowledge of the bristle deflections, adding complexity to the model and any controller designed using the dynamic model. In addition, we shall see later that the dynamic friction model has the potential to give rise to relative degree singularities under different conditions. The dynamic friction function therefore provides better capability to control, yet it has its own difficulties that make perfect linearization occasionally impossible.

Equations (111) and (115) apply as written only to a single wheel. We may rewrite (115) in more general form for all four wheels in terms of its $x$ and $y$ components as

$$\dot{\boldsymbol{\mu}}_x = \sigma_0(\boldsymbol{I}_4 - \sigma_1 \boldsymbol{L}_1)\dot{\boldsymbol{\zeta}}_x - \sigma_0 \sigma_1 \boldsymbol{L}_2(\boldsymbol{I}_4 - \boldsymbol{L}_1 \boldsymbol{L}_3)\mathrm{diag}(\boldsymbol{\zeta}_x)\boldsymbol{J}\dot{\boldsymbol{v}}_r + (\sigma_2 - \sigma_1)\dot{\boldsymbol{v}}_{rx} \tag{116}$$

$$\dot{\boldsymbol{\mu}}_y = \sigma_0(\boldsymbol{I}_4 - \sigma_1 \boldsymbol{L}_1)\dot{\boldsymbol{\zeta}}_y - \sigma_0 \sigma_1 \boldsymbol{L}_2(\boldsymbol{I}_4 - \boldsymbol{L}_1 \boldsymbol{L}_3)\mathrm{diag}(\boldsymbol{\zeta}_y)\boldsymbol{J}\dot{\boldsymbol{v}}_r + (\sigma_2 - \sigma_1)\dot{\boldsymbol{v}}_{ry} \tag{117}$$

where

$$\boldsymbol{L}_1 = \text{diag}\left(\frac{\|\boldsymbol{v}_{r,1}\|}{\Gamma(\boldsymbol{v}_{r,1})}, \ldots, \frac{\|\boldsymbol{v}_{r,4}\|}{\Gamma(\boldsymbol{v}_{r,4})}\right) \tag{118}$$

$$\boldsymbol{L}_2 = \text{diag}\left(\Gamma^{-1}(\boldsymbol{v}_{r,1}), \ldots, \Gamma^{-1}(\boldsymbol{v}_{r,4})\right) \tag{119}$$

$$\boldsymbol{L}_3 = \text{diag}\left(\frac{\partial\Gamma(\boldsymbol{v}_{r,1})}{\partial\|\boldsymbol{v}_{r,1}\|}, \ldots, \frac{\partial\Gamma(\boldsymbol{v}_{r,4})}{\partial\|\boldsymbol{v}_{r,4}\|}\right) \tag{120}$$

and $\boldsymbol{J}$ is the $4 \times 8$ Jacobian matrix of relative velocity norms

$$\boldsymbol{J} = \begin{bmatrix} \frac{\partial\|\boldsymbol{v}_{r,1}\|}{\partial\boldsymbol{v}_r} \\ \vdots \\ \frac{\partial\|\boldsymbol{v}_{r,4}\|}{\partial\boldsymbol{v}_r} \end{bmatrix} \tag{121}$$

The non-indexed relative velocity vector is now the $8 \times 1$ vector as defined in the previous chapter, while the indexed versions are the $2 \times 1$ vectors of $x$-$y$ relative velocity pairs. Equation (111) could be rewritten for all four wheels in a similar fashion, however, the difficulties presented by the zero relative velocity singularity of the steady-state friction function suggests that it does not warrant such a detailed consideration.

Recalling (66) from the previous chapter, the derivative of the relative velocity vector may be expressed as

$$\dot{\boldsymbol{v}}_r = \boldsymbol{\Xi}(\boldsymbol{\theta})\dot{\boldsymbol{\xi}} + \boldsymbol{V}\dot{\boldsymbol{\nu}} + \dot{\boldsymbol{\Xi}}(\boldsymbol{\theta})\boldsymbol{\xi} \tag{122}$$

and substituting the state derivatives from (73) and (74) into this equation, we have

$$\dot{\boldsymbol{v}}_r = \boldsymbol{\Xi}\boldsymbol{M}_1^{-1}(\boldsymbol{\eta} + \boldsymbol{A}\boldsymbol{P}^{-1}\boldsymbol{c}) + \dot{\boldsymbol{\Xi}}\boldsymbol{\xi} + r\boldsymbol{V}\boldsymbol{M}_2^{-1}\boldsymbol{\mu}_x\boldsymbol{P}^{-1}\boldsymbol{c} + \boldsymbol{V}\boldsymbol{M}_2^{-1}\boldsymbol{\tau} \tag{123}$$

where functional dependencies have once again been omitted for succinctness. We may also partion this vector into $x$ and $y$ sub-vectors as

$$\dot{\boldsymbol{v}}_{rx} = \boldsymbol{\Xi}_x\boldsymbol{M}_1^{-1}(\boldsymbol{\eta} + \boldsymbol{A}\boldsymbol{P}^{-1}\boldsymbol{c}) + \dot{\boldsymbol{\Xi}}_x\boldsymbol{\xi} + r^2\boldsymbol{M}_2^{-1}\boldsymbol{\mu}_x\boldsymbol{P}^{-1}\boldsymbol{c} + r\boldsymbol{M}_2^{-1}\boldsymbol{\tau} \tag{124}$$

$$\dot{\boldsymbol{v}}_{ry} = \boldsymbol{\Xi}_y\boldsymbol{M}_1^{-1}(\boldsymbol{\eta} + \boldsymbol{A}\boldsymbol{P}^{-1}\boldsymbol{c}) + \dot{\boldsymbol{\Xi}}_y\boldsymbol{\xi} \tag{125}$$

where the subscripts on the $\boldsymbol{\xi}$ matrices indicate the respective $x$ and $y$ partitions. Finally, substituting these results and employing an $x$-$y$ partioned form of the bristle dynamical

equation, (75), in (116)-(117), we arrive at the desired form of (96) and (97) with

$$\begin{aligned}
\boldsymbol{\alpha}_x(\boldsymbol{\xi},\boldsymbol{\nu},\boldsymbol{\zeta}) &= -\sigma_0(\boldsymbol{I}_4-\sigma_1\boldsymbol{L}_1)(\boldsymbol{\Xi}_x\boldsymbol{\xi}-r\boldsymbol{\nu}-\boldsymbol{Z}_{xx}\boldsymbol{\zeta}_x+\boldsymbol{Z}_{xy}\boldsymbol{\zeta}_y) \\
&\quad -\sigma_0\sigma_1\boldsymbol{L}_2(\boldsymbol{I}_4-\boldsymbol{L}_1\boldsymbol{L}_3)\mathrm{diag}(\boldsymbol{\zeta}_x)\boldsymbol{J}[\boldsymbol{\Xi}\boldsymbol{M}_1^{-1}(\boldsymbol{\eta}+\boldsymbol{A}\boldsymbol{P}^{-1}\boldsymbol{c})+\dot{\boldsymbol{\Xi}}\boldsymbol{\xi}+r\boldsymbol{V}\boldsymbol{M}_2^{-1}\boldsymbol{\mu}_x\boldsymbol{P}^{-1}\boldsymbol{c}] \\
&\quad +(\sigma_2-\sigma_1)[\boldsymbol{\Xi}_x\boldsymbol{M}_1^{-1}(\boldsymbol{\eta}+\boldsymbol{A}\boldsymbol{P}^{-1}\boldsymbol{c})+\dot{\boldsymbol{\Xi}}_x\boldsymbol{\xi}+r^2\boldsymbol{M}_2^{-1}\boldsymbol{\mu}_x\boldsymbol{P}^{-1}\boldsymbol{c}] \qquad (126) \\
\boldsymbol{\beta}_x(\boldsymbol{\xi},\boldsymbol{\nu},\boldsymbol{\zeta}) &= -\sigma_0\sigma_1\boldsymbol{L}_2(\boldsymbol{I}_4-\boldsymbol{L}_1\boldsymbol{L}_3)\mathrm{diag}(\boldsymbol{\zeta}_x)\boldsymbol{J}\boldsymbol{V}\boldsymbol{M}_2^{-1}+(\sigma_2-\sigma_1)r\boldsymbol{M}_2^{-1} \qquad (127) \\
\boldsymbol{\alpha}_y(\boldsymbol{\xi},\boldsymbol{\nu},\boldsymbol{\zeta}) &= -\sigma_0(\boldsymbol{I}_4-\sigma_1\boldsymbol{L}_1)(\boldsymbol{\Xi}_y\boldsymbol{\xi}-\boldsymbol{Z}_{yx}\boldsymbol{\zeta}_x-\boldsymbol{Z}_{yy}\boldsymbol{\zeta}_y) \\
&\quad -\sigma_0\sigma_1\boldsymbol{L}_2(\boldsymbol{I}_4-\boldsymbol{L}_1\boldsymbol{L}_3)\mathrm{diag}(\boldsymbol{\zeta}_y)\boldsymbol{J}[\boldsymbol{\Xi}\boldsymbol{M}_1^{-1}(\boldsymbol{\eta}+\boldsymbol{A}\boldsymbol{P}^{-1}\boldsymbol{c})+\dot{\boldsymbol{\Xi}}\boldsymbol{\xi}+r\boldsymbol{V}\boldsymbol{M}_2^{-1}\boldsymbol{\mu}_x\boldsymbol{P}^{-1}\boldsymbol{c}] \\
&\quad +(\sigma_2-\sigma_1)[\boldsymbol{\Xi}_y\boldsymbol{M}_1^{-1}(\boldsymbol{\eta}+\boldsymbol{A}\boldsymbol{P}^{-1}\boldsymbol{c})+\dot{\boldsymbol{\Xi}}_y\boldsymbol{\xi}] \qquad (128) \\
\boldsymbol{\beta}_y(\boldsymbol{\xi},\boldsymbol{\nu},\boldsymbol{\zeta}) &= -\sigma_0\sigma_1\boldsymbol{L}_2(\boldsymbol{I}_4-\boldsymbol{L}_1\boldsymbol{L}_3)\mathrm{diag}(\boldsymbol{\zeta}_y)\boldsymbol{J}\boldsymbol{V}\boldsymbol{M}_2^{-1} \qquad (129)
\end{aligned}$$

We now have the ability to complete the relative degree analysis by examining the properties of the $\boldsymbol{G}$ matrix.

### 5.2.3 Rank Properties of the $G$ Matrix

We assemble (100), (127), and (129) into the $\boldsymbol{G}$ matrix for the dynamical friction function case as

$$\begin{aligned}
\boldsymbol{G}(\boldsymbol{\xi},\boldsymbol{\nu},\boldsymbol{\zeta}) &= -\boldsymbol{R}_x\mathrm{diag}(\boldsymbol{N})\left[\sigma_0\sigma_1\boldsymbol{L}_2(\boldsymbol{I}_4-\boldsymbol{L}_1\boldsymbol{L}_3)\mathrm{diag}(\boldsymbol{\zeta}_x)\boldsymbol{J}\boldsymbol{V}\boldsymbol{M}_2^{-1}-(\sigma_2-\sigma_1)r\boldsymbol{M}_2^{-1}\right] \\
&\quad -\boldsymbol{R}_y\mathrm{diag}(\boldsymbol{N})\left[\sigma_0\sigma_1\boldsymbol{L}_2(\boldsymbol{I}_4-\boldsymbol{L}_1\boldsymbol{L}_3)\mathrm{diag}(\boldsymbol{\zeta}_y)\boldsymbol{J}\boldsymbol{V}\boldsymbol{M}_2^{-1}\right] \qquad (130)
\end{aligned}$$

Since all of the matrices except $\boldsymbol{R}_x$ and $\boldsymbol{R}_y$ are diagonal, we may rearrange the expression for $\boldsymbol{G}$ and regroup terms as

$$\begin{aligned}
\boldsymbol{G}(\boldsymbol{\xi},\boldsymbol{\nu},\boldsymbol{\zeta}) &= -\sigma_0\sigma_1\left[\boldsymbol{R}_x\mathrm{diag}(\boldsymbol{\zeta}_x)+\boldsymbol{R}_y\mathrm{diag}(\boldsymbol{\zeta}_y)\right]\mathrm{diag}(\boldsymbol{N})\boldsymbol{L}_2(\boldsymbol{I}_4-\boldsymbol{L}_1\boldsymbol{L}_3)\boldsymbol{J}\boldsymbol{V}\boldsymbol{M}_2^{-1} \\
&\quad +r(\sigma_2-\sigma_1)\boldsymbol{R}_x\mathrm{diag}(\boldsymbol{N})\boldsymbol{M}_2^{-1} \qquad (131)
\end{aligned}$$

It is now clear that when all bristle deflections are identically zero, the first term vanishes. Such a situation exists for steady-state, constant-speed vehicle operation. This occurs for straight-line motion when no torque is applied to the wheels. In such a situation, (87) shows that $\boldsymbol{R}_x=\boldsymbol{A}_x$ since $\boldsymbol{\mu}_x$ and $\boldsymbol{\mu}_y$ are zero, causing $\boldsymbol{A}$ to vanish as well. Examination of $\boldsymbol{A}_x$, as defined in Chapter 2, reveals that for zero steer, a loss of rank occurs since the second

row becomes identically zero, and the lateral jerk of the vehicle can no longer be influenced by wheel torque.

Further, if bristle deflection occurs in the longitudinal direction, with no deflection laterally, the first term now contributes nonzero entries in the longitudinal and angular velocity rows, but the matrix still does not have full row rank for the zero steer case since the second row of $\boldsymbol{R}_x$ is still zero. Should steering or lateral bristle deflection occur, the matrix achieves rank, and lateral velocity may be influenced. The matrix will maintain rank in all other cases except when all four wheels are steered identically. Since we have chosen to limit our consideration to a vehicle with front wheel steer only, this situation will not occur.

Bearing in mind the rank properties of the $\boldsymbol{G}$ matrix, we may now consider control of the vehicle.

## *5.3 Input-Output Linearization*

As we have already stated, the vehicle system has relative degree as long as the decoupling matrix of (104) exists and has full row rank. The input-output linearization for the system with output equation $\boldsymbol{y} = \boldsymbol{h}(\boldsymbol{\xi})$ is then achieved as specified in [25, Ch. 5] by finding the torque vector that satisfies

$$\frac{\partial \boldsymbol{h}(\boldsymbol{\xi})}{\partial \boldsymbol{\xi}} \boldsymbol{M}_1^{-1} \boldsymbol{G}(\boldsymbol{\xi}, \boldsymbol{\nu}, \boldsymbol{\zeta}) \boldsymbol{\tau} = \ddot{\boldsymbol{y}}_r - \frac{d}{dt} \frac{\partial \boldsymbol{h}(\boldsymbol{\xi})}{\partial \boldsymbol{\xi}} \dot{\boldsymbol{\xi}} - \frac{\partial \boldsymbol{h}(\boldsymbol{\xi})}{\partial \boldsymbol{\xi}} \boldsymbol{M}_1^{-1} \boldsymbol{f}(\boldsymbol{\xi}, \boldsymbol{\nu}, \boldsymbol{\zeta}) \tag{132}$$

where $\ddot{\boldsymbol{y}}_r$ is the reference output signal that must be tracked. We may then prescribe second-order dynamics for the controlled system by defining this reference signal as

$$\ddot{\boldsymbol{y}}_r = \ddot{\boldsymbol{y}}^d + \boldsymbol{K}_d(\dot{\boldsymbol{y}}^d - \dot{\boldsymbol{y}}) + \boldsymbol{K}_p(\boldsymbol{y}^d - \boldsymbol{y}) \tag{133}$$

with positive definite gain matrices, $\boldsymbol{K}_d$ and $\boldsymbol{K}_p$, and desired trajectory, $\boldsymbol{y}^d$.

It is important to note now that any valid, full rank, decoupling matrix is non-square. This makes (132) underdetermined, with a non-unique $\boldsymbol{\tau}$. Any solution to this equation is valid and may be used for the control, however, the unique minimum torque vector norm solution is provided by the right pseudoinverse of the decoupling matrix, which is

$$\boldsymbol{D}^+ = \boldsymbol{G}^T \boldsymbol{M}_1^{-1} \left( \frac{\partial \boldsymbol{h}(\boldsymbol{\xi})}{\partial \boldsymbol{\xi}} \right)^T \left( \frac{\partial \boldsymbol{h}(\boldsymbol{\xi})}{\partial \boldsymbol{\xi}} \boldsymbol{M}_1^{-1} \boldsymbol{G} \boldsymbol{G}^T \boldsymbol{M}_1^{-1} \left( \frac{\partial \boldsymbol{h}(\boldsymbol{\xi})}{\partial \boldsymbol{\xi}} \right)^T \right)^{-1} \tag{134}$$

and this provides the unique control

$$\boldsymbol{\tau} = \boldsymbol{D}^{+}\left[\ddot{\boldsymbol{y}}_r - \frac{d}{dt}\frac{\partial \boldsymbol{h}(\boldsymbol{\xi})}{\partial \boldsymbol{\xi}}\dot{\boldsymbol{\xi}} - \frac{\partial \boldsymbol{h}(\boldsymbol{\xi})}{\partial \boldsymbol{\xi}}\boldsymbol{M}_1^{-1}\boldsymbol{f}(\boldsymbol{\xi},\boldsymbol{\nu},\boldsymbol{\zeta})\right] \tag{135}$$

which is capable of producing both positive and negative wheel torque.

We could have alternatively chosen to utilize the extra degrees of freedom to impose torque constraints. Such constraints often exist due to mechanical driveline limitations. These constraints may be implemented by augmenting the decoupling matrix and the right-hand side of (132) for linear constraints or by utilizing nonlinear equation solving techniques in the case of nonlinear constraints. For a decoupling matrix with $r$ rows, up to $4 - r$ constraints may be employed.

We now possess sufficient theory to consider implementation of control for a few different system output definitons.

### 5.3.1 Speed Control

Control may be first demonstrated for the simplest output definition consisting only of longitudinal velocity, which shall be referred to simply as speed. In this case, the output function, $\boldsymbol{h}(\boldsymbol{\xi})$ takes the form

$$\boldsymbol{h}(\boldsymbol{\xi}) = \begin{bmatrix} 1 & 0 & 0 \end{bmatrix}\boldsymbol{\xi} \tag{136}$$

and the input-output linearization shall be performed for the system with relative degree two, with the second derivative of its ouput as

$$\ddot{\boldsymbol{y}} = \boldsymbol{f}_1(\boldsymbol{\xi},\boldsymbol{\nu},\boldsymbol{\zeta}) + \boldsymbol{G}_1(\boldsymbol{\xi},\boldsymbol{\nu},\boldsymbol{\zeta})\boldsymbol{\tau} \tag{137}$$

where the subscript 1 on $\boldsymbol{f}$ and $\boldsymbol{G}$ indicates that we have selected the first rows of each. The control now becomes

$$\boldsymbol{\tau} = \boldsymbol{G}_1^T\left(\boldsymbol{G}_1\boldsymbol{G}_1^T\right)^{-1}\left[m_v\ddot{y}_r - f_1\right] \tag{138}$$

where

$$\ddot{y}_r = \ddot{s}^d + k_d(\dot{s}^d - \dot{\xi}_1) + k_p(s^d - \xi_1) \tag{139}$$

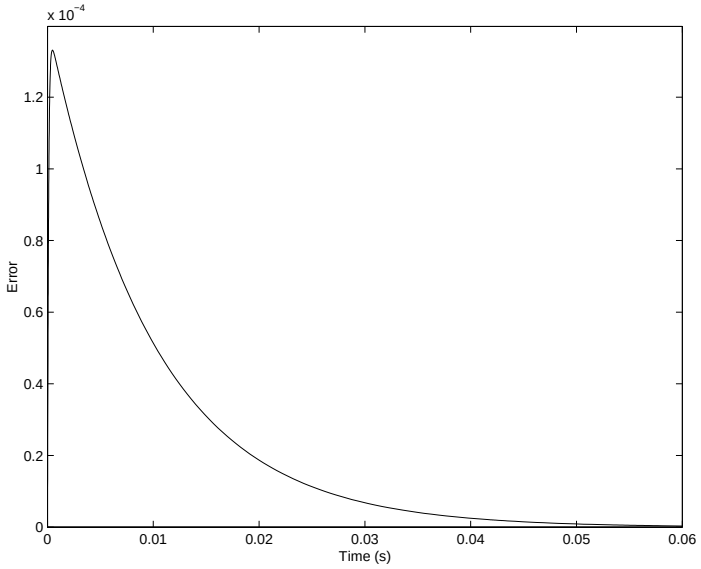


**Figure 33:** Speed error for straight-line acceleration control.

where $s^d$ is a twice-differentiable desired speed signal, and $k_p$ and $k_d$ are scalar gains. The signal $\dot{\xi}_1$ is the longitudinal acceleration of the vehicle body, which may be either measured or computed from (73) as the application requires.

To test this control, we choose a constant acceleration desired trajectory, such that the desired jerk term is zero, and speed is linearly increasing. We are most interested in vehicle performance for slippery roads where loss of vehicle control is most prevalent, so we select friction parameters as in the previous chapter to approximate driving on ice. We also set all control model parameters to match the simulation model parameters as given in Chapter 2.4.

Figure 33 shows the error evolution in the speed, resulting from application of the control with the controller parameters listed in Table 3 for the first 60 milliseconds of operation. Observe the initial error transient before the controller achieves the desired steady state acceleration.

We may also examine the torque applied by the controller to one of the wheels during its operation. The first millisecond of operation is shown in Figure 34 and we see that the controller initially applies as much effort as the torque limits allow to quickly accelerate the

**Table 3:** Parameters used for speed control.

| Parameter | Value |
|---|---|
| $k_p$ | 1e6 |
| $k_d$ | 1e4 |

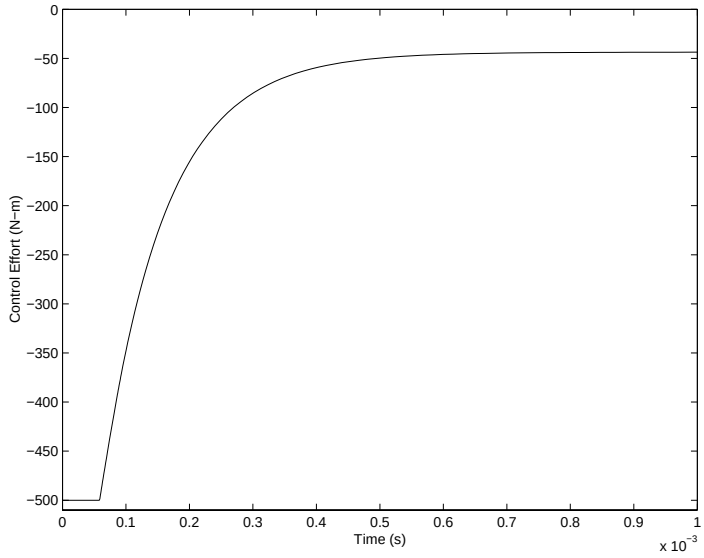


**Figure 34:** Control effort transient for straight-line speed control.

vehicle, but this effort quickly decreases as the tire friction achieves the necessary force.

Such acceleration performance, however, may be achieved by open-loop torque application, so we turn our attention to the more difficult problem of speed control during a vehicle maneuver. Our model now functions in two dimensions, but we shall employ identical friction bristle stiffnesses and damping along the $x$- and $y$-axes so that our control may have perfect model matching.

Figure 35 shows a comparison of the vehicle's speed under application of control versus open-loop torque inputs of -11 Nm and -13 Nm at the front and rear wheels, respectively, for a lane-change type maneuver with a desired acceleration of 0.2 m/s$^2$, and gains selected as in the previous example. The steering input for this manuever is shown in Figure 36.

Note that the controlled vehicle tracks the desired speed almost perfectly, with some disturbance at the intervals where the steering angle is changing, while the uncontrolled

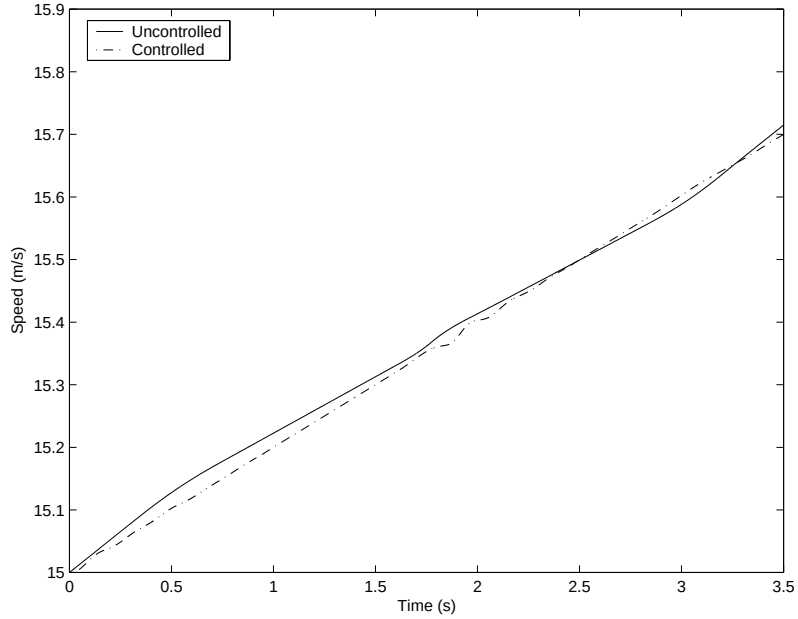


**Figure 35:** Comparison of controlled versus uncontrolled vehicle speed.

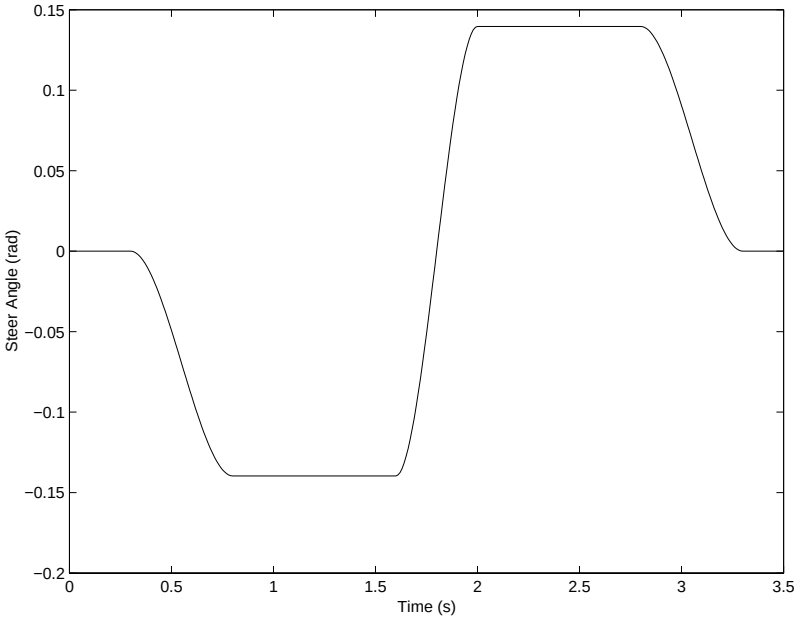


**Figure 36:** Steering input for lane-change maneuver.

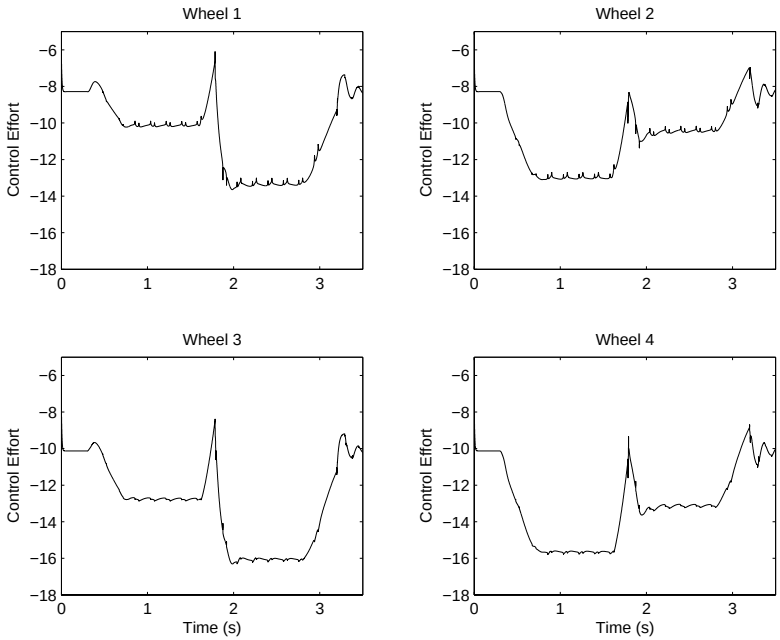


**Figure 37:** Control effort for speed control during lane-change maneuver.

vehicle's speed varies with the amount of steering input. It is instructive to also observe the control efforts that achieve this performance. These are shown in Figure 37 and from these we see that the controller increases the effort suitably over the intervals where the open-loop inputs failed to maintain the vehicle's speed. In addition, very fast transients may be observed which appear as spikes in the effort, corresponding to time instants when the relative velocity of the corresponding wheel-road contact point is near zero, and the relative velocity gradient estimates take effect. As relative velocity disappears, bristle deflection rate vanishes and force changes may only be produced by means of bristle acceleration. Such bristle acceleration may be produced by the rapid wheel acceleration that the controller attempts to create at these instants.

For more aggressive maneuvers or higher desired accelerations, control effort requests becomes very large and are restricted only by the torque limits. This results from an inability to achieve sufficient bristle deflection in order to supply the necessary force at the road-wheel interface, requiring that bristle transients supply the remaining force. Such bristle transients are only possible by generating high relative velocity through application

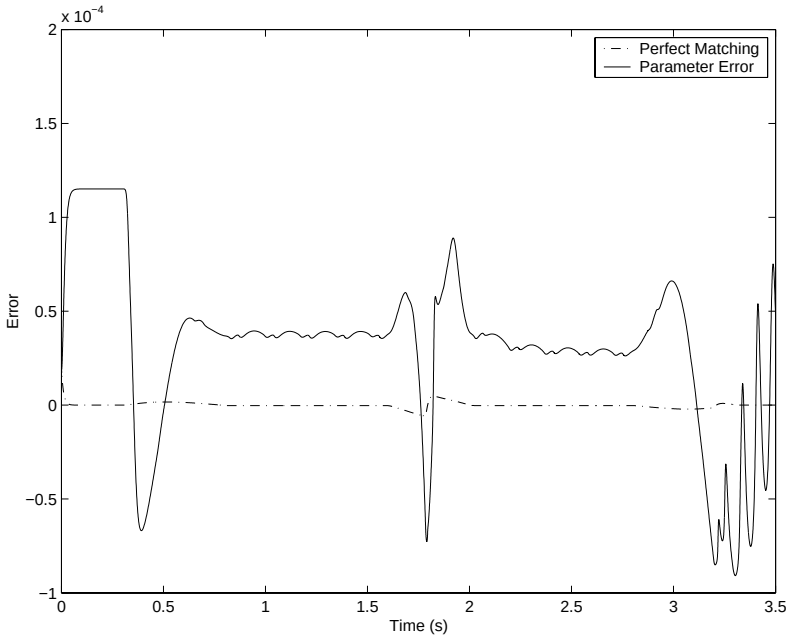


**Figure 38:** Comparison of speed tracking error for small bristle stiffness model mismatch.

of large amounts of wheel torque. In order to avoid such undesirable performance, we must therefore always limit the desired trajectories to within achievable acceleration bounds.

#### *5.3.1.1 Effect of Friction Parameter Mismatch*

In Chapter 3 we developed a friction model that allowed for different bristle stiffness and damping along the two wheel axes, but we have designed our controller under the assumption of identical stiffnesses along both axes. We now consider the effect of a slight parameter mismatch on the ability of the controller to track the desired speed.

We experiment first with a slight variation in the bristle stiffness, increasing $\sigma_{0,y}$ for the model to 200 N/m and we set the control model lateral bristle stiffness to 189 N/m; the average value of the model's bristle stiffness along each axis. Figure 38 shows a comparison of the resulting speed error for the control with perfect model matching to that with mismatched lateral bristle stiffness. Observe that the error is much larger for the mismatched controller, however, it is still relatively low.

We now increase the model's lateral bristle stiffness to 650 N/m and the controller's

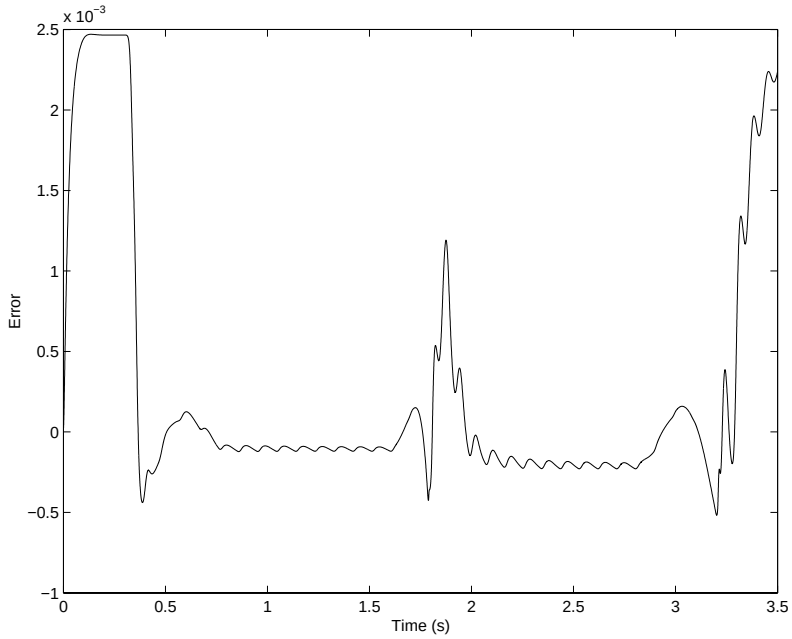


**Figure 39:** Speed tracking error for large bristle stiffness model mismatch.

average bristle stiffness parameter to 414 N/m and observe the effect on the control's speed tracking performance once again. Observe in Figure 39 that despite such significant parameter mismatch, the controller achieves the desired speed to within one-hundreth of one meter per second.

We now return the model bristle stiffness to 178 N/m along both axes and experiment with variations in the bristle damping parameter, $\sigma_1$. Since this parameter precedes the bristle rate terms through which control authority enters the system, variations in this parameter are of great concern. Maintaining $\sigma_{1,x}$ at 1 Ns/m, setting $\sigma_{1,y}$ for the model to 5 Ns/m, and the controller's average damping parameter to 3 Ns/m, we simulate the system under speed control. The resulting error is shown in Figure 40 and we see that despite some large transient error in the control, the overall tracking error is maintained extremely small.

Finally, we simulate the system with errors in both bristle stiffness and damping parameters and observe controller tracking performance. The error in Figure 41 is for the model with $\sigma_{0,x} = 178$ N/m, $\sigma_{0,y} = 650$ N/m, $\sigma_{1,x} = 1$ Ns/m, and $\sigma_{0,y} = 5$ Ns/m. The controller parameters are set to the average of these pairs as in the previous examples. Note that once

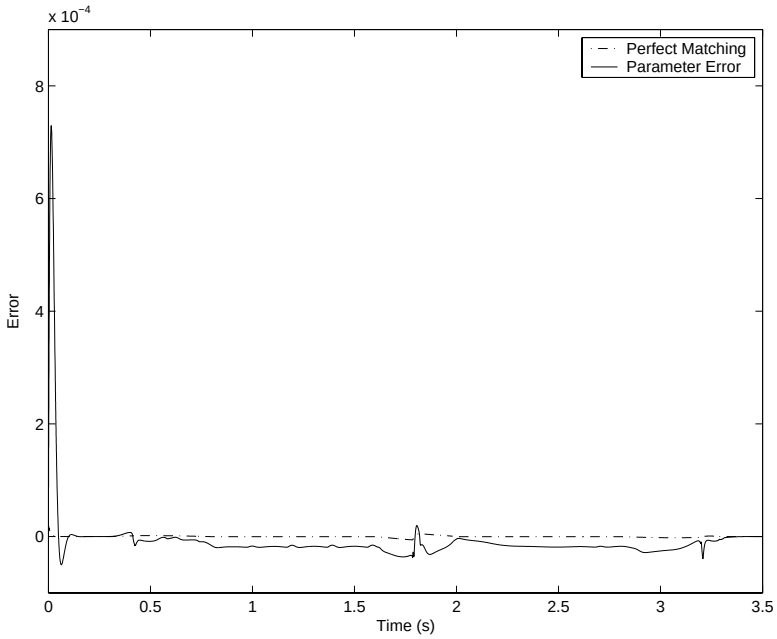


**Figure 40:** Speed tracking error for bristle damping model mismatch.

again, very low tracking error is achieved.

With such high robustness to friction parameter mismatch, we can now be confident in our choice to utilize a control model with constant parameters.

### 5.3.2 Combined Speed and Yaw Control

We may now consider a less trivial case for control. Let us now define the outputs as longitudinal velocity and vehicle angular velocity. In this case, the control becomes

$$\boldsymbol{\tau} = \boldsymbol{G}_{1,3}^T \left( \boldsymbol{G}_{1,3} \boldsymbol{G}_{1,3}^T \right)^{-1} \left[ \text{diag}(m_v, I_v) \ddot{\boldsymbol{y}}_r - \boldsymbol{f}_{1,3} \right] \tag{140}$$

where the subscripts on $\boldsymbol{f}$ and $\boldsymbol{G}$ now indicate selection of the first and third rows, corresponding to the desired output variables. The vector $\ddot{\boldsymbol{y}}_r$ is now

$$\ddot{\boldsymbol{y}}_r = \begin{bmatrix} \ddot{s}^d \\ \ddot{\omega}^d \end{bmatrix} + \begin{bmatrix} k_{d,1}(\dot{s}^d - \dot{\xi}_1) \\ k_{d,2}(\dot{\omega}^d - \dot{\xi}_3) \end{bmatrix} + \begin{bmatrix} k_{p,1}(s^d - \xi_1) \\ k_{p,2}(\omega^d - \xi_3) \end{bmatrix} \tag{141}$$

and we specify the first row in an identical manner as we did for the case of speed control only. Once again, the derivatives of the velocity states are vehicle accelerations which may

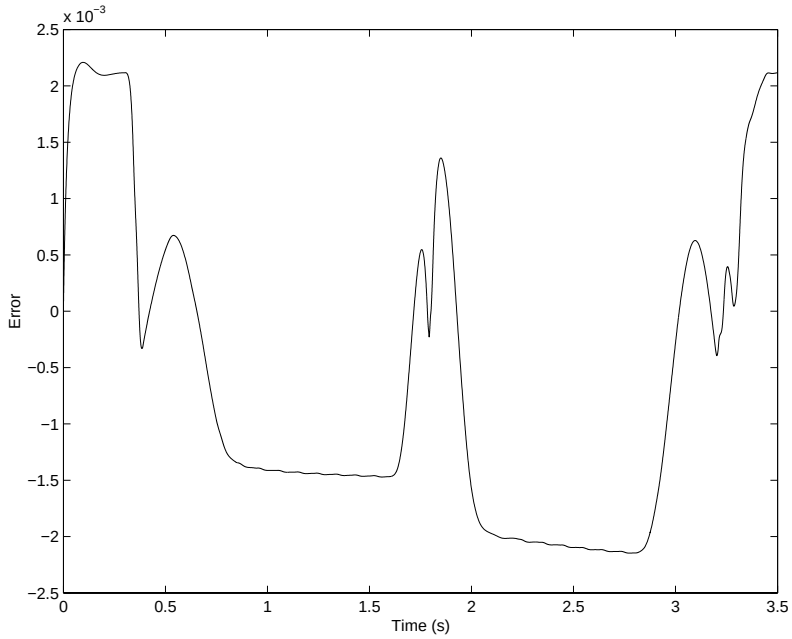


**Figure 41:** Speed tracking error for model mismatch in both bristle stiffness and damping.

be either measured or computed. We specify the desired angular velocity as a fraction of that which would be achieved under no lateral wheel slip conditions as

$$\omega^d = k_\omega \frac{s_d \sin(\theta_1)}{y_1 \sin(\theta_1) + (x_1 - x_3)\cos(\theta_1)} \tag{142}$$

where $k_\omega$ is the scale parameter, and we may compute the derivatives of this expression for use as well. High rates of steer, however, would cause unnecessarily high tracking requests which might exceed the friction limits of the system, and we therefore treat the steering rates as zero when computing the derivatives. We execute the control in simulation with gains as indicated in Table 4 for an identical lane-change maneuver as in the speed control example, but with 38% of the steer angle as previously and 0.2 m/s$^2$ of desired longitudinal acceleration once again. The resulting error evolution is shown in Figure 42 for both speed and angular velocity.

We see in the figure that both outputs are successfully controlled, however, the yaw rate error increases significantly during steering transients. Figure 43 shows a comparison of the vehicle yaw rate under control to that of a vehicle with a constant torque of -10 Nm at

**Table 4:** Gains for yaw control.

| Parameter | Value |
|---|---|
| $k_p$ | 1e5 |
| $k_d$ | 1e4 |
| $k_\omega$ | 0.5 |

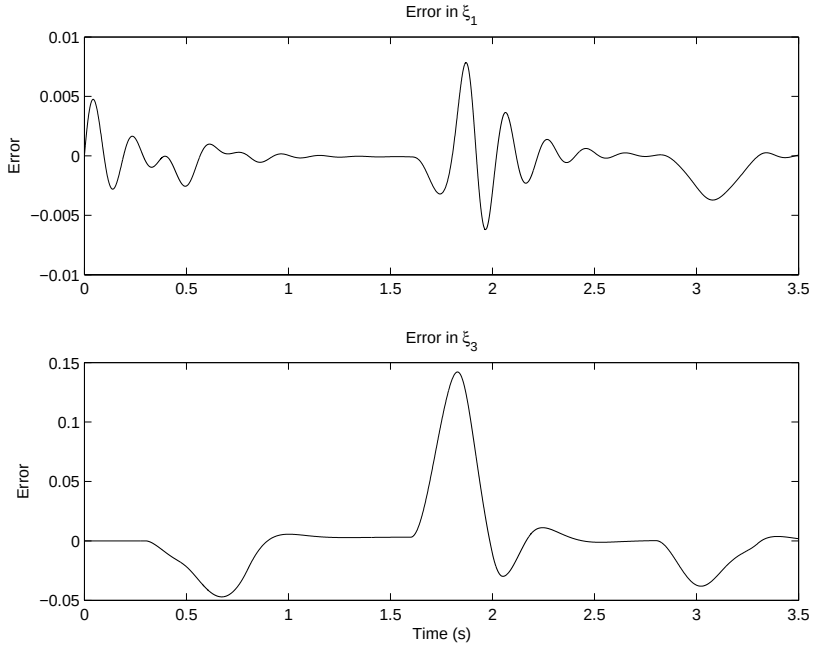


**Figure 42:** Error evolution for combined speed and yaw rate control.

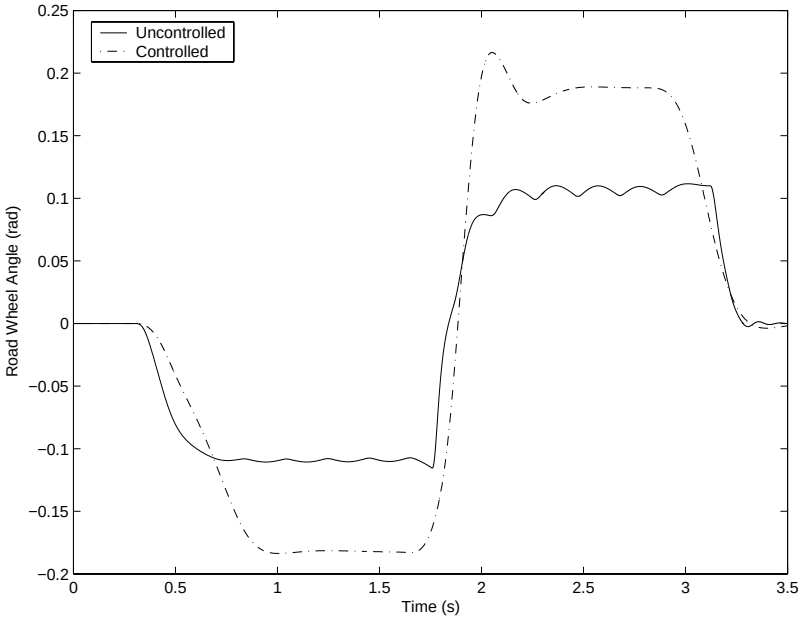


**Figure 43:** Comparison of controlled yaw response to uncontrolled vehicle response.

each wheel and identical steering input. Here the success of the control is apparent as the uncontrolled vehicle achieves far less steady-state yaw rate than its controlled counterpart.

Once again, the success of the control is limited by the available friction forces and higher yaw rate requests tend to cause the controller to saturate.

### 5.3.3 Full Vehicle Body Control

Having achieved some success with control of two of the vehicle outputs, we now consider the possibility of simultaneous control of all three vehicle body velocities. The previous relative degree analysis of this chapter seems to suggest this possibility.

Returning again to consideration of the structure of the $\boldsymbol{G}$ matrix, we recall that this matrix loses rank under zero steer conditions. Further, due to the fact that, in general, $\sigma_0 \gg \sigma_1 \gg \sigma_2$, the condition of the $\boldsymbol{G}\boldsymbol{G}^T$ matrix with respect to inversion is almost entirely determined by the rank properties of the matrix

$$\boldsymbol{R}_x \text{diag}(\boldsymbol{\zeta}_x) + \boldsymbol{R}_y \text{diag}(\boldsymbol{\zeta}_y) \tag{143}$$

Therefore, if this matrix loses rank or is poorly conditioned, then the control is either not

computable or excessively large.

Using the definitions of $\boldsymbol{R}_x$ and $\boldsymbol{R}_y$, we express this matrix as

$$\begin{aligned} &\boldsymbol{A}_x \left[ \boldsymbol{I}_4 + \boldsymbol{\mu}_x \boldsymbol{P}^{-1} \left( \boldsymbol{P}_x \text{diag}(\boldsymbol{\zeta}_x) + \boldsymbol{P}_y \text{diag}(\boldsymbol{\zeta}_y) \right) \right] \\ &+ \boldsymbol{A}_y \left[ \boldsymbol{I}_4 + \boldsymbol{\mu}_y \boldsymbol{P}^{-1} \left( \boldsymbol{P}_x \text{diag}(\boldsymbol{\zeta}_x) + \boldsymbol{P}_y \text{diag}(\boldsymbol{\zeta}_y) \right) \right] \end{aligned} \tag{144}$$

and from this representation we see that the condition of the $\boldsymbol{G}$ matrix is almost completely determined by the magnitude of the steering input. If the steering angle is small, then the second row of $\boldsymbol{A}_x$ is correspondingly small due to the sine terms. In addition, if $\boldsymbol{\mu}_y$ is much smaller than $\boldsymbol{\mu}_x$, then the cosine terms of the second row of $\boldsymbol{A}_y$ have little effect. Thus, in order to influence the lateral velocity of the vehicle to the same extent as the longitudinal and angular velocities, we require either large steer angles, or large pre-existing lateral friction forces. However, large lateral forces rarely occur prior to the appearance of significant steer so that control of lateral velocity will usually only be possible if the vehicle's driver steers sufficiently. We thus have little hope of achieving control of lateral velocity given the current system architecture, vehicle model, and standard input-output linearization theory.

# CHAPTER VI

# CONCLUSION

This thesis addresses the problem of automobile dynamic control by means of wheel torque. In order to address this problem thoroughly, a new nonlinear vehicle model with a careful consideration of friction was necessary.

A vehicle dynamic model has been systematically presented that describes the motion of an automobile in the horizontal plane. This model provides for wheel torque at each wheel as inputs and vehicle and wheel velocities as outputs. Steering is considered a time-varying signal which influences the system structure, and the model allows for independent steering angles to be specified for each wheel. A method for computing independent normal forces at each wheel of the vehicle was demonstrated, eliminating the need for modeling of a vehicle suspension.

Friction model selection was based upon a desire for a first-principles treatment of friction. A dynamic friction model known as the LuGre model, and based upon the view of friction as the interaction between microscopic surface asperities, was chosen. A point contact form of the LuGre friction model was discussed and important extensions to previous two-dimensional versions of the LuGre model were developed. This friction model was then combined with the vehicle model to form a complete set of equations of motion for a vehicle system.

The vehicle model was simulated in MATLAB and shown to exhibit the expected properties of a physical automobile. Both normal road and slick road cases were addressed and compared. Different torque input scenarios were also addressed and shown to impact the vehicle responsiveness to the steering signal.

The relative degree of the system was analyzed and the vehicle model was shown to possess well defined relative degree for the class of outputs that are a function of vehicle body longitudinal and angular velocity. For outputs that are defined as a function of vehicle

body lateral velocity, relative degree singularities or near-singularities were shown to exist.

Control of the vehicle for two system output definitions was demonstrated. These outputs were defined simply as longitudinal velocity in the first case, and both longitudinal and angular velocity in the second case. Robustness in the presence of variations in friction model parameters that results from the use of average, rather than exact, parameters was shown for the case of vehicle longitudinal velocity control. In such cases the control tracking error was shown to increase, but to remain within acceptable bounds.

## *6.1 Future Work*

Significant opportunities for future work based upon the developments of this thesis are possible, in both the areas of modeling and control.

First, a lumped-parameter version of the LuGre friction model may be developed as in [8, 47, 12] by integrating the extended point contact model presented in Chapter 3 over a contact patch. This would enhance the accuracy of the overall model and make it more immediately applicable for comparison to physical automobiles.

Further generalizations of the vehicle model of Chapter 2 as well as modeling of additional, higher-order dynamic effects are also possible. Vehicle model generalizations that have not been incorporated into the current model include the possibility of wheel camber angle, the allowance of wheel steering rotation about a point other than the wheel geometric center, and different wheel radii for the consideration of underinflated or spare tires. Dynamic effects that were not considered for this work include a vehicle suspension model, which might be of interest for some problems, and the effect of wheel inertia about the $z$-axis and its impact on normal force.

The area of control provides the greatest potential for future work since this thesis presents only initial investigations into the mathematical structure of the vehicle system model equations and control implementation. One opportunity for investigation is made clear by the discussion in Chapter 5 of the singularity or near-singularity when system outputs are defined as a function of lateral velocity. Such problems have been dealt with to some extent for other systems and [18] presents a method for approximate decoupling in

the presence of near singularities that might be applicable to the vehicle problem.

Additionally, this thesis did not undertake an analysis of the zero dynamics of the vehicle system. Such an analysis would reveal greater fundamental properties of the system, most particularly if it is minimum phase. Should the system prove not to be minimum phase in certain regimes, methods of approximate decoupling for non-minimum phase systems were presented in [4] and might be of some use.

The availability of state measurements for control design was assumed in this work, but in practice, only direct measurements of wheel speed and vehicle body angular velocity states are available. Lateral and longitudinal accelerations may be measured by use of accelerometers, but sensors to directly measure the translational vehicle velocities are generally too expensive to be practical. In addition, direct measurement of the friction model bristle deflection states is not possible. These difficulties necessitate the implementation of nonlinear model-based dynamic observers for future practical implementation of the control that has been developed in this work.

Finally, an analytical study of the effect of friction limits on the ability to control the vehicle has yet to be undertaken. In the past, use of static friction models has dictated the presence of an absolute friction bound, however, use of the dynamic friction LuGre model, as in this thesis, suggests that the production of higher forces is possible. A more detailed investigation of the equations of motion that were presented in Chapter 4 might reveal control methods for utilizing this available force.

In conclusion, this thesis has presented a combination of both existing theory and a number of unique developments that point towards a new direction for automobile dynamic modeling and control design. While the focus of this work has been control of a vehicle by means of wheel torque, its results are applicable to many other challenges facing the automotive community as it seeks to improve customer satisfaction and safety.

# REFERENCES


[1] Anwar, S., "A predictive control algorithm for a yaw stability management system," in *Vehicle Dynamics & Simulation, 2003*, pp. 189–198, Warrendale, Pennsylvania: Society of Automotive Engineers, 2003.

[2] Armstrong-Helouvry, B., Dupont, P., and Canudas de Wit, C., "A survey of models, analysis tools and compensation methods for the control of machines with friction," *Automatica*, vol. 30, no. 7, pp. 1083–1138, 1994.

[3] Beer, F. P. and Johnston, Jr., E. R., *Mechanics of Materials*. New York: McGraw Hill, Inc., second ed., 1992.

[4] Benvenuti, L., Di Benedetto, M., and Grizzle, J., "Approximate output tracking for nonlinear non-minimum phase systems with an application to flight control," *International Journal of Robust and Nonlinear Control*, vol. 4, pp. 397–414, 1994.

[5] Brennan, S. and Alleyne, A., "Integrated vehicle control via coordinated steering and wheel torque inputs," in *Proceedings of the American Control Conference*, (Arlington, Virginia), pp. 7–12, June 2001.

[6] Canudas de Wit, C., Olsson, H., Astrom, K. J., and Lischinsky, P., "A new model for control of systems with friction," *IEEE Transactions on Automatic Control*, vol. 40, pp. 419–425, March 1995.

[7] Canudas de Wit, C. and Tsiotras, P., "Dynamic tire friction models for vehicle traction control," in *Proceedings of the 38th Conference on Decision and Control*, (Phoenix, Arizona), pp. 3746–3751, December 1999.

[8] Canudas de Wit, C., Tsiotras, P., Velenis, E., Basset, M., and Gissinger, G., "Dynamic friction models for road/tire longitudinal interaction," *Vehicle System Dynamics*, vol. 39, no. 3, pp. 189–226, 2003.

[9] Chowanietz, E., "Automobile electronics in the 1990s; part2: Chassis electronics," *Electronics & Communication Engineering Journal*, pp. 53–58, April 1995.

[10] Chu, T., Jones, R., and Whittaker, L., "A system theoretic analysis of automotive vehicle dynamics and control," *Vehicle System Dynamics*, vol. 37, no. Supplement, pp. 83–95, 2002.

[11] Claeys, X., Yi, J., Alvarez, L., Horowitz, R., and Canudas de Wit, C., "A dynamic tire/road friction model for 3d vehicle control and simulation," in *IEEE Intelligent Transportation Systems Conference Proceedings*, (Oakland, CA), pp. 483–488, August 2001.

[12] Deur, J., "A dynamic tire friction model for combined longitudinal and lateral motion," in *Proceedings of 2001 ASME International Mechanical Engineering Congress and Exposition*, (New York, NY), pp. 229–236, 2001.

[13] Drakunov, S. V., Ashrafi, B., and Rosiglioni, A., "Yaw control algorithm via sliding mode control," in *Proceedings of the American Control Conference*, (Chicago, Illinois), pp. 580–583, June 2000.

[14] Esmailzadeh, E., Goodarzi, A., and Vossoughi, G., "Optimal yaw moment control law for improved vehicle handling," *Mechatronics*, vol. 13, no. 7, pp. 659–675, 2003.

[15] Ghoneim, Y. A., Lin, W. C., Sidlosky, D. M., Chen, H. H., Chin, Y.-K., and Tedrake, M. J., "Integrated chassis control system to enhance vehicle stability," *International Journal of Vehicle Design*, vol. 23, no. 1/2, pp. 124–144, 2000.

[16] Gillespie, T. D., *Fundamentals of Vehicle Dynamics*. Warrendale, Pennsylvania: Society of Automotive Engineers, first ed., 1992.

[17] Ginsberg, J. H., *Advanced Engineering Dynamics*. Cambridge: Cambridge University Press, second ed., 1998.

[18] Godbole, D. N. and Sastry, S. S., "Approximate decoupling and asymptotic tracking for mimo systems," *IEEE Transactions on Automatic Control*, vol. 40, pp. 441–450, March 1995.

[19] Guntur, R. and Sankar, S., "A friction circle concept for dugoff's tyre friction model," *International Journal of Vehicle Design*, vol. 1, no. 4, pp. 373–377, 1980.

[20] Guvenc, B. A., Acarman, T., and Guvenc, L., "Coordination of steering and individual wheel braking actuated vehicle yaw stability control," in *Proceedings of the IEEE Intelligent Vehicles Symposium*, (Columbus, Ohio), pp. 288–293, June 2003.

[21] Hahn, J.-O., Hur, J.-W., Yi, K., Kang, S., and Lee, K. I., "Nonlinear vehicle stability control using disturbance observer," in *Proceedings of the 2002 IEEE International Conference on Control Applications*, (Glasgow, Scotland), pp. 441–446, September 2002.

[22] Hallowell, S. J. and Ray, L. R., "All-wheel driving using independent torque control of each wheel," in *Proceedings of the American Control Conference*, (Denver, Colorado), pp. 2590–2595, June 2003.

[23] Horiuchi, S., Okada, K., and Nohtomi, S., "Improvement of vehicle handling by nonlinear integrated control of four wheel steering and four wheel torque," *JSAE Review*, vol. 20, pp. 459–464, 1999.

[24] ichiro Sakai, S., Sado, H., and Hori, Y., "Motion control in an electric vehicle with four independently driven in-wheel motors," *IEEE/ASME Transactions on Mechatronics*, vol. 4, pp. 9–16, March 1999.

[25] Isidori, A., *Nonlinear Control Systems*. New York: Springer-Verlag, second ed., 1989.

[26] Khalil, H., *Nonlinear Systems*. Upper Saddle River, New Jersey: Prentice Hall, third ed., 2002.

[27] Kwak, B. and Park, Y., "Robust vehicle stability controller based on multiple sliding mode control," in *Brake Technology ABS/TCS, and Controlled Suspensions*, pp. 73–79, Warrendale, Pennsylvania: Society of Automotive Engineers, 2001.

[28] Langson, W. and Alleyne, A., "Multivariable bilinear vehicle control using steering and individual wheel torques," in *Proceedings of the American Control Conference*, (Albuquerque, New Mexico), pp. 1136–1140, June 1997.

[29] Lin, H.-F. and Seireg, A. A., "Vehicle dynamics and stabilisation using a nonlinear tyre model with four-wheel steering and braking," *International Journal of Computer Application in Technology*, vol. 11, no. 1/2, pp. 53–64, 1998.

[30] Mokhiamar, O. and Abe, M., "Active wheel steering and yaw moment control combination to maximize stability as well as vehicle responsiveness during quick lane change for active vehicle handling safety," *Proceedings of the Institution of Mechanical Engineers, Part D: Journal of Automobile Engineering*, vol. 216, pp. 115–124, 2002.

[31] Nagai, M., Yamanaka, S., and Hirano, Y., "Integrated control of active rear wheel steering and yaw moment control using braking forces," *JSME International Journal, Series C*, vol. 42, no. 2, pp. 301–308, 1999.

[32] National Highway Traffic Safety Administration, National Center for Statistics & Analysis, *Fatality Analysis Reporting System (FARS)*. http://www-fars.nhtsa.dot.gov.

[33] Noronha, P. F., "A robust lumped-parameter tire model developed for real-time simulation," in *ABS/Brake/VDC Technology*, pp. 79–89, Warrendale, Pennsylvania: Society of Automotive Engineers, 1998.

[34] Ono, E., Hosoe, S., Asano, K., Sugai, M., and Doi, S., "Robust stabilization of the vehicle dynamics by gain-scheduled $h_\infty$ control," in *Proceedings of the 1999 IEEE International Conference on Control Applications*, (Kohala Coast Island, Hawaii), pp. 1679–1685, August 1999.

[35] Pacejka, H. B. and Bakker, E., "The magic formula tyre model," *Vehicle System Dynamics*, vol. 21, no. Supplement, pp. 1–18, 1993.

[36] Park, J. H. and Ahn, W. S., "$H_\infty$ yaw-moment control with brakes for improving driving performance and stability," in *Proceedings of the 1999 IEEE/ASME International Conference on Advanced Intelligent Mechatronics*, (Atlanta, Georgia), pp. 747–752, September 1999.

[37] Pilutti, T., Ulsoy, G., and Hrovat, D., "Vehicle steering intervention through differential braking," in *Proceedings of the American Control Conference*, (Seattle, Washington), pp. 1667–1671, June 1995.

[38] Reimpell, J., Stoll, H., and Betzler, J., *The Automotive Chassis*. Warrendale, Pennsylvania: Society of Automotive Engineers, second ed., 2001.

[39] Rodic, A. D. and Vukobratovic, M., "Contribution to the integrated control synthesis of road vehicles," *IEEE Transactions on Control Systems Technology*, vol. 7, pp. 64–78, January 1999.

[40] Rosiglioni, A. and Drakunov, S. V., "A nonlinear stability controller for rear wheel driven vehicles," in *Proceedings of the 41st IEEE Conference on Decision and Control*, (Las Vegas, Nevada), pp. 879–880, December 2002.

[41] Rossetter, E. J. and Gerdes, J. C., "The role of handling characteristics in driver assistance systems with environmental interaction," in *Proceedings of the American Control Conference*, (Chicago, Illinois), pp. 2528–2532, June 2000.

[42] Shim, T. and Margolis, D., "Using $\mu$ feedforward for vehicle stability enhancement," *Vehicle System Dynamics*, vol. 35, no. 2, pp. 103–119, 2001.

[43] Shimada, K. and Shibahata, Y., "Comparison of three active chassis control methods for stabilizing yaw moments," in *SAE Document 940870*, pp. 87–96, Warrendale, Pennsylvania: Society of Automotive Engineers, 1994.

[44] Shino, M., Miyamoto, N., Wang, Y., and Nagai, M., "Traction control of electric vehicles considering vehicle stability," in *6th International Workshop on Advanced Motion Control*, (Nagoya, Japan), pp. 311–316, 2000.

[45] Tahami, F., Kazemi, R., and Farhanghi, S., "A novel driver assist stability system for all-wheel-drive electric vehicles," *IEEE Transactions on Vehicular Technology*, vol. 52, pp. 683–692, May 2003.

[46] Unyelioglu, K. A., Ozguner, U., Hissong, T., and Winkelman, J., "Wheel torque proportioning, rear steering, adn normal force control: A structural investigation," *IEEE Transactions on Automatic Control*, vol. 42, pp. 803–818, June 1997.

[47] Velenis, E., Tsiotras, P., Canudas-De-Wit, C., and Sorine, M., "Dynamic tire friction models for combined longitudinal and lateral vehicle motion," *Vehicle System Dynamics*, To appear in 2004.

[48] Wang, Y. and Nagai, M., "Integrated control of four-wheel-steer and yaw moment to improve dynamic stability margin," in *Proceedings of the 35th IEEE Conference on Decision and Control*, (Kobe, Japan), pp. 1783–1784, December 1996.

[49] Yi, K., Chung, T., Kim, J., and Yi, S., "An investigation into differential braking strategies for vehicle stability control," *Proceedings of the Institution of Mechanical Engineers, Part D: Journal of Automobile Engineering*, vol. 217, pp. 1081–1093, 2003.

[50] Yoshioka, T., Adachi, T., Butsuen, T., Okazaki, H., and Mochizuki, H., "Application of sliding-mode theory to direct yaw-moment control," *JSAE Review*, vol. 20, pp. 523–529, 1999.

[51] You, S.-S. and Jeong, S.-K., "Vehicle dynamics and control synthesis for four-wheel steering passenger cars," *Proceedings of the Institution of Mechanical Engineers, Part D*, vol. 212, pp. 449–461, 1998.